UNIVERSITA' DEGLI STUDI DI MILANO-BICOCCA
Dipartimento di Biotecnologie e Bioscienze
Dottorato di ricerca in Biologia XXVI ciclo

NORMAL AND PATHOGENIC ATAXIN-3: BIOLOGICAL ROLES, TOXICITY AND FIBRILLOGENESIS

Tutor: Dott.ssa Maria Elena Regonesi

Marcella Bonanomi
Matr.: 055116

Anno Accademico 2012/2013

Table of contents

Abstract

Ataxin-3 (AT3) is a deubiquitinating enzyme that triggers the inherited neurodegenerative disorder spinocerebellar ataxia type 3 when its polyglutamine (polyQ) stretch close to the C-terminus exceeds a critical length. It consists of the N-terminal globular Josephin domain (JD) and the C-terminal disordered one. Regarding its physiological role, it has ubiquitin hydrolase activity implicated in the function of the ubiquitin-proteasome system, but also plays a role in the pathway that sorts aggregated protein to aggresomes *via* microtubules.

In the first part of this work, we further investigated its function(s) by taking advantage of Small Angle X-ray Scattering (SAXS) and Surface Plasmon Resonance (SPR). We demonstrated that an AT3 oligomer consisting of 6-7 subunits tightly binds to the tubulin hexameric oligomer at the level of three distinct tubulin-binding regions, one located in the JD, and the two others in the disordered domain, upstream and downstream of the polyQ stretch. By SPR we have also provided the first evidence of direct binding of AT3 to HDAC6, one of the components of the transport machinery that sorts protein to the aggresome.

In the second part of this work, we have investigated the mechanisms of AT3 cytotoxicity triggered by expanded variants. For this purpose, we used *Saccharomyces cerevisiae* as a eukaryotic cellular model. We expressed a wild type (Q26), a pathogenic (Q85) and a truncated (291Δ) variant of the protein. The expanded form caused reduction in viability, accumulation of reactive oxygen species, imbalance of the antioxidant defense system and loss in cell membrane integrity. An AT3 variant truncated upstream of the polyQ also exerted a detrimental effect on cell growth and similar cytotoxicity, although

to a lesser extent, which points to the involvement of also non-polyQ regions in cytotoxicity.

Finally, we sought to evaluate the effects of tetracycline and epigallocatechin-3-gallate (EGCG), two well-known inhibitors of amyloid aggregation, on AT3 fibrillogenesis and cytotoxicity. We observed that tetracycline does not apparently change the aggregation mode, as supported by Fourier Transform Infrared spectroscopy and Atomic Force Microscopy data, but slightly retards further aggregation of the earliest soluble oligomers. In contrast, EGCG apparently increases the aggregation rate but also leads to the formation of off-pathway, non-amyloid, final aggregates. Despite these different effects, co-incubation of the AT3 with either compounds resulted in significantly lower cytotoxicity during AT3 aggregation.

Chapter One

Introduction

1.1 PROTEIN MISFOLDING DISEASES: THE AMYLOIDOSES

A broad range of human diseases arises from the failure of a specific peptide or protein to adopt, or remain in, its native functional conformational state. These pathological conditions are generally referred to as *protein misfolding (or protein conformational) diseases* (PMD). Partially folded or misfolded states often tend to aggregate, particularly when they represent major kinetic traps in the folding pathway. This is due to the fact that these forms typically expose hydrophobic amino acid residues and regions of unstructured polypeptide backbone, features that are mostly buried in the native state. Like intra-molecular folding, aggregation — the association of two or more non-native protein molecules — is largely driven by hydrophobic forces and primarily results in the formation of amorphous structures [1]. Alternatively, aggregation can lead to the formation of highly ordered, fibrillar aggregates called amyloid, in which β-strands run perpendicular to the long fibril axis (cross-β structure), with specific tinctorial properties (binding to Congo red and thioflavin S), higher resistance to proteolytic degradation and a fibrillar appearance under electron microscopy (straight, unbranched, 10 nm wide fibrils) [2].

Pathologies developing amyloid fibrils are called amyloidoses. The diseases can be broadly grouped into (i) neurodegenerative conditions, in which aggregation occurs in the brain, (ii) non-neuropathic localized amyloidosis, in which aggregation occurs in a single type of tissue other than the brain, and (iii) non-neuropathic systemic amyloidosis, in which aggregation occurs in multiple tissues (Table 1.1) [1].

Table 1.1: Human diseases associated with formation of extracellular amyloid deposits or intracellular inclusions with amyloid-like characteristics [1].

Disease	Aggregating protein or peptide	Number of residues[a]	Native structure of protein or peptide[b]
Neurodegenerative diseases			
Alzheimer's disease[c]	Amyloid β peptide	40 or 42[f]	Natively unfolded
Spongiform encephalopathies[c,e]	Prion protein or fragments thereof	253	Natively unfolded (residues 1–120) and α-helical (residues 121–230)
Parkinson's disease[c]	α-Synuclein	140	Natively unfolded
Dementia with Lewy bodies[c]	α-Synuclein	140	Natively unfolded
Frontotemporal dementia with Parkinsonism[c]	Tau	352–441[f]	Natively unfolded
Amyotrophic lateral sclerosis[c]	Superoxide dismutase 1	153	All-β, Ig like
Huntington's disease[d]	Huntingtin with polyQ expansion	3144[g]	Largely natively unfolded
Spinocerebellar ataxias[d]	Ataxins with polyQ expansion	816[g,h]	All-β, AXH domain (residues 562–694); the rest are unknown
Spinocerebellar ataxia 17[d]	TATA box-binding protein with polyQ expansion	339[g]	α+β, TBP like (residues 159–339); unknown (residues 1–158)
Spinal and bulbar muscular atrophy[d]	Androgen receptor with polyQ expansion	919[g]	All-α, nuclear receptor ligand-binding domain (residues 669–919); the rest are unknown
Hereditary dentatorubral-pallidoluysian atrophy[d]	Atrophin-1 with polyQ expansion	1185[g]	Unknown
Familial British dementia[d]	ABri	23	Natively unfolded
Familial Danish dementia[d]	ADan	23	Natively unfolded
Nonneuropathic systemic amyloidoses			
AL amyloidosis[c]	Immunoglobulin light chains or fragments	~90[f]	All-β, Ig like
AA amyloidosis[c]	Fragments of serum amyloid A protein	76–104[f]	All-α, unknown fold
Familial Mediterranean fever[c]	Fragments of serum amyloid A protein	76–104[f]	All-α, unknown fold
Senile systemic amyloidosis[c]	Wild-type transthyretin	127	All-β, prealbumin like
Familial amyloidotic polyneuropathy[d]	Mutants of transthyretin	127	All-β, prealbumin like
Hemodialysis-related amyloidosis[c]	β2-microglobulin	99	All-β, Ig like
ApoAI amyloidosis[d]	N-terminal fragments of apolipoprotein AI	80–93[f]	Natively unfolded
ApoAII amyloidosis[d]	N-terminal fragment of apolipoprotein AII	98[i]	Unknown
ApoAIV amyloidosis[c]	N-terminal fragment of apolipoprotein AIV	~70	Unknown
Finnish hereditary amyloidosis[d]	Fragments of gelsolin mutants	71	Natively unfolded
Lysozyme amyloidosis[d]	Mutants of lysozyme	130	α+β, lysozyme fold
Fibrinogen amyloidosis[d]	Variants of fibrinogen α-chain	27–81[f]	Unknown
Icelandic hereditary cerebral amyloid angiopathy[d]	Mutant of cystatin C	120	α+β, cystatin like
Nonneuropathic localized diseases			
Type II diabetes[c]	Amylin, also called islet amyloid polypeptide (IAPP)	37	Natively unfolded
Medullary carcinoma of the thyroid[c]	Calcitonin	32	Natively unfolded
Atrial amyloidosis[c]	Atrial natriuretic factor	28	Natively unfolded
Hereditary cerebral haemorrhage with amyloidosis[d]	Mutants of amyloid β peptide	40 or 42[f]	Natively unfolded
Pituitary prolactinoma	Prolactin	199	All-α, 4-helical cytokines
Injection-localized amyloidosis[c]	Insulin	21 + 30[j]	All-α, insulin like
Aortic medial amyloidosis[c]	Medin	50[k]	Unknown
Hereditary lattice corneal dystrophy[d]	Mainly C-terminal fragments of kerato-epithelin	50–200[f]	Unknown
Corneal amylodosis associated with trichiasis[c]	Lactoferrin	692	α+β, periplasmic-binding protein like II
Cataract[c]	γ-Crystallins	Variable	All-β, γ-crystallin like
Calcifying epithelial odontogenic tumors[c]	Unknown	~46	Unknown
Pulmonary alveolar proteinosis[d]	Lung surfactant protein C	35	Unknown
Inclusion-body myositis[c]	Amyloid β peptide	40 or 42[f]	Natively unfolded
Cutaneous lichen amyloidosis[c]	Keratins	Variable	Unknown

[a]Data refer to the number of residues of the processed polypeptide chains that deposit into aggregates, not of the precursor proteins.
[b]According to Structural Classification Of Proteins (SCOP), these are the structural class and fold of the native states of the processed peptides or proteins that deposit into aggregates prior to aggregation.
[c]Predominantly sporadic, although in some cases hereditary forms associated with specific mutations are well documented.
[d]Predominantly hereditary, although in some cases sporadic forms are documented.
[e]Five percent of the cases are transmitted (e.g., iatrogenic).
[f]Fragments of various lengths are generated and have been reported to be present in ex vivo fibrils.
[g]Lengths shown refer to the normal sequences with nonpathogenic traits of polyQ.
[h]Length shown is for ataxin-1.
[i]The pathogenic mutation converts the stop codon into a Gly codon, extending the 77-residue protein by 21 additional residues.
[j]Human insulin consists of two chains (A and B, with 21 and 30 residues, respectively) covalently linked by disulfide bridges.

1.1.1 Molecular mechanisms of amyloidoses

Although the proteins involved share few or no functional and structural similarities, the molecular mechanisms of the pathogenesis of amyloidoses are essentially the same (Fig. 1.1). It is widely established that amyloid fibril formation has many characteristics of a "nucleated growth" mechanism. The time course of the conversion of a peptide or protein into its fibrillar form (measured by thioflavin T (ThT) fluorescence, light scattering, or other techniques) typically includes a lag phase that is followed by a rapid exponential growth phase [3-6]. The lag phase is assumed to be the time required for "nuclei" to form. Once a nucleus is formed, fibril growth is thought to proceed rapidly by further association of either monomers or oligomers with the nucleus. Addition of preformed fibrillar species to a sample of a protein under aggregation conditions ("seeding") causes the lag phase to be shortened and ultimately abolished when the rate of the aggregation process is no longer limited by the need for nucleation [3, 4].

Growing evidence suggests that the species mainly responsible for toxicity in cells are not mature amyloid fibrils, but the pre-fibrillar oligomeric species [7, 8]. Bucciantini and collaborators showed that the soluble pre-fibrillar aggregates generated *in vitro* by a synthetic peptide containing the N-terminal domain of *Escherichia coli* HypF (not related to any amyloid-like disease) are highly cytotoxic, while the mature fibrils generated from the same protein have a much more attenuated effect [9]. Similar results were obtained in experiments performed using the prefibrillar forms of other proteins involved in amyloidosis such as transthyretin, α-synuclein (α-syn), amyloid β peptides (Aβ) and proteins containing polyglutamine (polyQ) tracts, such as

huntingtin (htt) [1]. This also led to the suggestion that the formation of mature fibrillar aggregates may be a defense mechanism for the cell [10].

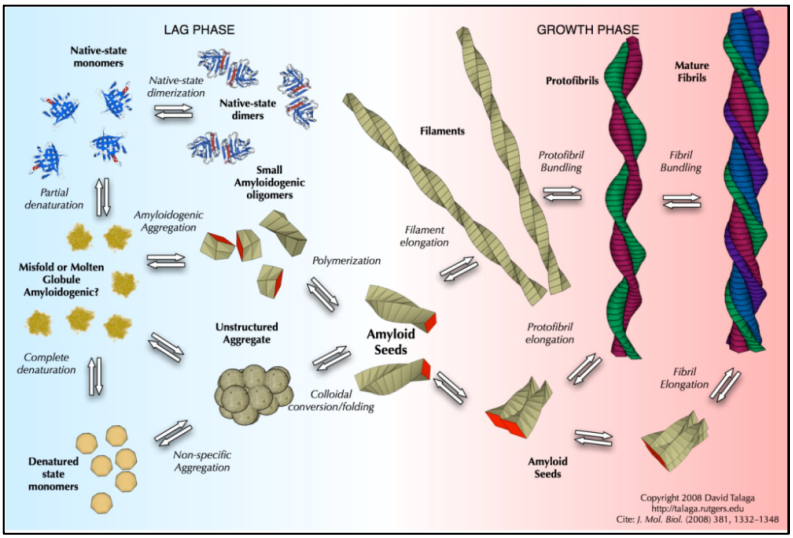

Fig. 1.1 Possible pathways of amyloid formation starting from denatured monomeric protein. Normally a protein, co-translationally or just after its synthesis, acquires its correct native fold. If the protein is not able to reach the native conformation, it can go through an aggregation process, leading to the formation of amyloid fibrils [11].

1.1.2 Mechanisms of toxicity of amyloidogenic protein aggregates

The exposure of neurons to prefibrillar aggregates generates numerous biochemical, cytological and physiological alterations, showing how protein quality control and homeostasis alterations are central elements in the pathogenesis of amyloidoses [12].

Many amyloidogenic peptides/proteins are capable of interacting with lipid membranes thus inducing membrane permeabilization, which may be involved in PMD pathogenesis [13-15]. Two major membrane

permeabilization models have been proposed: (i) transmembrane pore formation via a "barrel-stave model"; and (ii) membrane destruction/solubilization via a "carpet model" [16]. According to the "barrel-stave model", pores are either formed by the direct interaction of protein oligomers and the hydrophobic core of the membrane or by the assembly of monomers on the hydrophobic core of the membrane, which further recruits additional monomers (Fig. 1.2) [17]. In the "carpet model", the amyloidogenic proteins first bind to the surface of the membrane and cover it in a "carpet-like" manner with the positively charged residues interacting with the negatively charged phospholipids head groups. When a critical amyloidogenic protein monomer concentration threshold is reached, the membrane bilayer disintegrates in a detergent-like manner [18, 19].

Mounting evidence suggests that oxidative stress is a major contributor to the pathology of most PMDs [20]. Amyloidogenic proteins, including Aβ, α-syn, prion protein and islet amyloid polypeptide (IAPP), share the ability to generate reactive oxygen species (ROS) that are associated with oxidative stress [21-23].

Endoplasmic reticulum (ER) stress-induced apoptosis has recently been identified as an important signaling pathway in PMDs [24-26]. For example, intraneuronal Aβ oligomers can cause cell death by inducing ER stress in hippocampal neurons of a transgenic mouse expressing the amyloid precursor protein (APP) [27]. Furthermore, amyloidogenic proteins such as Aβ and IAPP have been shown to induce cell apoptosis by promoting the release of two ER stress markers (C/EBP homologous protein and caspase-12) from the ER [21, 28].

Amyloidogenic proteins may exert their cytotoxicity also at the level of the mitochondrial signaling pathway [29-31]. During the process of

amyloidogenesis, cytochrome C (cyt C) and AIF (apoptosis-inducing factor) are released from mitochondria, which in turn induce DNA damage and cell apoptosis [32-34].

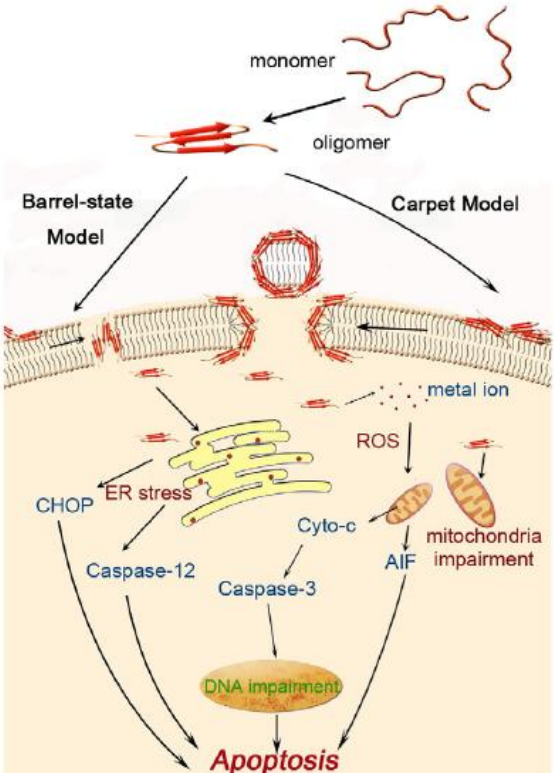

Fig. 1.2 Mechanisms of toxicity of amyloidogenic protein aggregation. The aggregation of amyloidogenic proteins may induce cytotoxicity by four mechanisms: lipid membrane permeabilization; oxidative stress; ER stress; and mitochondrial dysfunction [35].

1.2 TRINUCLEOTIDE REPEAT EXPANSION DISEASES

Repeated sequences constitute about 30% of the human genome and they are a central point in the evolution of the genome as a hot spot of recombination, deletions and insertions [36]. These regions include microsatellites, repeated sequences in telomeres, centromeres and the sequences of repeated trinucleotides (triplets). When the triplets exceed a critical length, they may result in pathological conditions that have been classified as Trinucleotide Repeat Expansion Diseases (TREDs). The mechanism of expansion is based on the formation of loops and hairpins and consequently to the insertion of additional repeats during DNA replication. The mutations in the trinucleotides repeated sequences, that determine instability and expansion of these sequences, are implicated in different human diseases such as neurodegenerative diseases, neuromuscular and mental retardation [37].

TREDs are grouped into two major classes based on the position of the expansion in the genome:

- in class I TREDs the expansion is located into non-coding regions (usually in regulatory elements) and therefore it can potentially affect the expression of the adjacent genes (e.g. X-fragile syndrome, Myotonic dystrophy, Friedreich's ataxia);
- in class II, the expansion occurs in translated regions and this leads to a gain of toxic function of the synthesized protein, which eventually acquires the capability to form toxic aggregated species (e.g. Spinocerebellar ataxias, Huntington's disease).

1.2.1 PolyQ diseases

A typical class II expansion consists of trinucleotide CAG repeats that are translated as an expanded tract of repeated glutamines (polyQ) in the encoded protein. The associated diseases, called polyQ diseases, arise in the case the polyQ length exceeds a certain threshold. This group of disorders includes nine members: Huntington's disease (HD), dentatorubral-pallidoluysian atrophy (DRPLA), spinal and bulbar muscular atrophy (SBMA) and spinocerebellar ataxia types (SCA) 1, 2, 3 6, 7 and 17 [38-40] (Table 1.2).

Table 1.2 Biologic features of polyQ expansion diseases [41].

Disease name	Mutated gene	Protein product	Putative function	CAG repeat size		Regions most affected
				Normal	Pathogenic	
HD	*HD*	Huntingtin	Signaling, transport, transcription	6–34	36–121	Striatum, cerebral cortex
DRLPA	*DRPLA*	Atrophin 1	Transcription	7–34	49–88	Cerebellum, cerebral cortex, basal ganglia, Luys body
SBMA	*AR*	Androgen receptor	Steroid-hormone receptor	9–36	38–62	Anterior horn and bulbar neurons, dorsal root ganglia
SCA1	*SCA1*	Ataxin-1	Transcription	6–39	40–82	Cerebellar Purkinje cells, dentate nucleus, brainstem
SCA2	*SCA2*	Ataxin-2	RNA metabolism	15–24	32–200	Cerebellar Purkinje cells, brainstem, frontotemporal lobes
SCA3	*ATXN3/ MJD/SCA3*	Ataxin-3	Deubiquitinating activity and transcription regulation	10–51	55–87	Cerebellar dentate neurons, basal ganglia, brainstem, spinal cord
SCA6	*CACNA1A*	$CACNA1_A$	P/Q-type α1A calcium channel subunit	4–20	20–29	Cerebellar Purkinje cells, dentate nucleus, inferior olive
SCA7	*SCA7*	Ataxin-7	Transcription	4–35	37–306	Cerebellum, brainstem, macula, visual cortex
SCA17	*SCA17*	TBP	Transcription	25–42	47–63	Cerebellar Purkinje cells, inferior olive

Abbreviations: HD, Huntington's disease; DRPLA, dentatorubral-pallidoluysian atrophy; SBMA, spinal and bulbar muscular atrophy; SCA, spinocerebellar ataxia; MJD, Machado–Joseph disease; $CACNA1_A$, calcium channel, voltage dependent, P/Q type, α1A subunit; TBP, TATA box binding protein.

All these diseases are characterized by a selective neuronal loss accompanied by a collection of associated physical and psychological complications, though the particular features vary among the different diseases [38]. In fact, although the different polyQ diseases have several common traits, the proteins associated with each different disorder share no homology outside the polyQ tract, being structurally and functionally unrelated [38, 40]. The mechanisms by which polyQ-expanded proteins lead to pathology are still not completely understood. One important common aspect to all polyQ expansion diseases is the negative correlation between the age of onset and the number of CAG repeats, meaning that a greater number of such

repeats results in an earlier development of the disease [40, 42-45]. The fact that the polyQ expansion is a common causative aspect to all these diseases and that its size correlates negatively with the age of onset are indicative of the importance that the expanded polyQ sequence has on the mechanisms leading to the disease. The involvement of the polyQ-expanded tracts has been explained in several ways, including: (a) polyQ stretch-induced modifications of the host protein, eventually leading to functional alterations (e.g., changes in intermolecular interactions) and/or to the transition into an aggregate-prone state and consequent generation of toxic oligomers; (b) generation of toxic polyQ containing fragments after cleavage of the host protein; (c) transcriptional changes, caused by interactions of the expanded protein with specific transcription factors; (d) proteotoxic stress as a result of the disruption of the quality control systems of the cell; (e) mitochondrial dysfunction [39]. One characteristic hallmark of all polyQ expansion diseases is the formation of large macromolecular protein aggregates or inclusion bodies containing the expanded and misfolded disease protein, in the nucleus and/or cytoplasm of neurons (and glial cells, in rare cases) [40]. These cell-generated structures, distinct from the small aggregates or oligomers formed by the self association of the proteins, have been related to the pathogenesis of the polyQ expansion diseases for a long time, but recent evidence supports the idea that they actually result from end-stage protective cellular mechanisms moved against the toxicity of the misfolded expanded protein oligomers [39, 46-48]. Notably, polyQ toxicity has been associated not only with the expanded proteins that are translated from the CAG-expanded genes, but also with the expanded CAG repeat-containing RNA, which (by recruiting specific intracellular proteins) has been shown to cause toxicity by itself [49]. Although there are some aspects shared by the different polyQ diseases that must be attended to, in order to

study possible common mechanisms of pathogenesis, there are peculiar aspects as well. The different neurodegeneration and symptomatic profiles of each polyQ expansion disease may be explained as a result of the fact that the polyQ expansion is inserted into a different host protein in each different disease. The diverse properties of each of these proteins, which include their subcellular localization, abundance, structure, activity and biological role, along with the way the polyQ expansion affects them, shall constitute the factors responsible for each disease's specific presentation [38].

1.2.1.1 Machado-Joseph disease

Machado–Joseph disease (MJD), otherwise known as spinocerebellar ataxia type 3 (SCA3), is an inherited neurodegenerative disorder originally described in people of Portuguese Azorean descent [50-52], but nowadays described as the most common form of autosomal dominantly-inherited ataxia in the world [44, 45, 53]. Apart from Portugal, the disease has been identified in many countries including Spain, Italy, Germany, China, Taiwan, Japan, Australia, Brazil, United States and Canada [45, 51, 52].

The gene causatively associated with MJD is ATXN3, located on the long arm of chromosome 14 (14q32.1) [54, 55], and encoding a polyQ-containing protein named ataxin-3 (AT3) [54]. In the healthy population, the number of CAG repeats lies between 10 and 51, with 55–87 CAG repeats being reported to associate with the disease [56, 57]. Nonetheless, CAG repeat numbers between 45 and 51 seem to belong to an overlapping region of healthy and disease phenotypes, since, while the longest repeat number detected in healthy people was 51, some smaller repeats have also been

identified as associated with the development of MJD, the smallest of them being 45 CAG repeats [45, 57].

MJD neurodegeneration profile involves neuronal loss in selective regions of the nervous system, including the cerebellum (spinocerebellar pathways and dentate nucleus), the substantia nigra, the striatum, the thalamus, pontine nuclei, spinal cord and cranial nerves (including locus coeruleus and vestibular nuclei), as well as visual, auditory, vestibular, somatosensory, and ingestion and urination-related systems; cerebral and cerebellar cortexes, inferior olive and Purkinje cells are moderately preserved [42, 50-52, 58-61]. Regarding brain functionality, metabolism (assessed by glucose utilization) was shown to be decreased in the cerebellum, brainstem, cerebral cortex, thalamus and putamen [45, 62, 63], and both dopaminergic and cholinergic neurotransmissions were reported to be negatively affected [60, 63, 64]. MJD pathogenesis results in a set of characteristic clinical symptoms, including the hallmark progressive ataxia, other general neuromuscular complications like dystonia, dysarthria, spasticity, rigidity, fasciculation, postural instability and proprioceptive loss, visual (nystagmus, eyelid retraction, ophthalmoparesis, double vision) and speech (dysarthria) disorders, dysphagia, amyotrophy, corticospinal and autonomic nervous system dysfunctions and neuropathy [45, 51, 52, 62]. The course of the disease is progressive and death occurs typically for pulmonary complications and cachexia, from 6 to 29 years after onset [52, 65]. In a recent study, it was calculated that the average age of survival is around 21 years after the start of the first symptoms of the disease [66].

1.3 ATAXIN-3

AT3 is a protein of wide distribution among eukaryotes, having been identified in protozoa, plants, fungi and animals, from nematodes and flatworms to arthropods and vertebrates. In mice and humans, despite the localized neuronal degeneration observed in MJD patients, AT3 displays a ubiquitous expression among different body tissues and cell types [67-71]. It was found to be widely expressed throughout the brain, though different regions present varying expression levels [71].

AT3 is composed by a structured globular N-terminal domain followed by a flexible C-terminal tail [72]. The N-terminal domain, termed Josephin domain (JD) (residues 1-182), displays ubiquitin (Ub) protease activity, while the flexible tail presents two Ub-interacting motifs (UIMs) (residues 224-243; 244-263), followed by the polyQ region of variable length, whose expansion beyond a certain threshold is associated with MJD [73-75] (Fig. 1.3 A). Other features of the protein are a highly conserved nuclear localization signal (NLS) upstream of the polyQ (residues 282-285) and two nuclear export signal (NES) in the JD (residues 77-99, 141-158) [76, 77]. Further, five serine residues present in the UIMs (S236, S256, S260/S261, S340, S352) have been identified as potential phosphorylation sites; also, an ubiquitinatable lysine residue was mapped to residue 117, inside the JD (Fig. 1.3 A).

The NMR structure of the JD revealed that it is mainly composed of two subdomains – a globular catalytic subdomain and a helical hairpin [75, 78] (Fig. 1.3 B and C). The JD surface presents two binding sites for Ub: site 1, close to the catalytic cleft separating the two subdomains, and site 2, contiguous but placed on the opposite surface [79] (Fig. 1.3 D and E). The Ub protease activity,

i.e., the ability to cleave isopeptide bonds between Ub monomers, was first predicted through an integrative bioinformatic analysis of AT3 amino acid sequence [77] and later confirmed biochemically using model substrates and Ub protease-specific inhibitors [74, 75, 78, 80], establishing AT3 and other identified JD-containing proteins as deubiquitinating enzymes (DUBs) [74, 77, 81]. Comparative analysis of the JD showed that AT3 belongs to the papain-like cysteine protease family, and the amino acids of the catalytic triad, C14, H119 and N134 (Fig. 1.3 C), are strictly conserved when compared to Ub C-terminal hydrolases (UCH) and Ub-specific processing proteases (USP) [75, 78]. Q9 is also important for the catalytic activity. The two conserved UIMs located N-terminally of the polyQ region are α-helical structures separated by a short flexible linker region and act cooperatively when binding Ub; in other words, the affinity of the two tandem motifs is greater than that of each individual UIM [82].

Different human AT3 isoforms resulting from alternative splicing have been described, the longest having an approximate molecular weight of 42 kDa [68, 71, 83]. Notably, the most common isoform found in the human brain has an extra UIM localized in the C-terminal region, downstream of the polyQ sequence [84]. A recent study identified a total of 56 human alternative splicing variants, expected to be translated into at least 20 isoforms, with varying predicted domain architecture [85], but the actual biological relevance of such variants remains unknown.

In addition to the ubiquitous distribution of AT3 among tissues, the protein seems to be widely, though heterogeneously, distributed within the cells themselves, being found in the cytoplasm (mitochondria included) and the nucleus, with varying degrees of predominance depending on the cell type [71, 86-91]. In human brain cells, AT3 localizes mainly in the perikarya, though,

depending on the analyzed cells, it was also detected on proximal processes, axons and nuclei. This heterogeneity suggests that regulation of AT3 expression levels and localization may be functionally important [71]. Some studies demonstrated that AT3 is actively transported across the nuclear envelope, being actively shuttled from the cytoplasm to the nucleus and vice versa [86, 92-93].

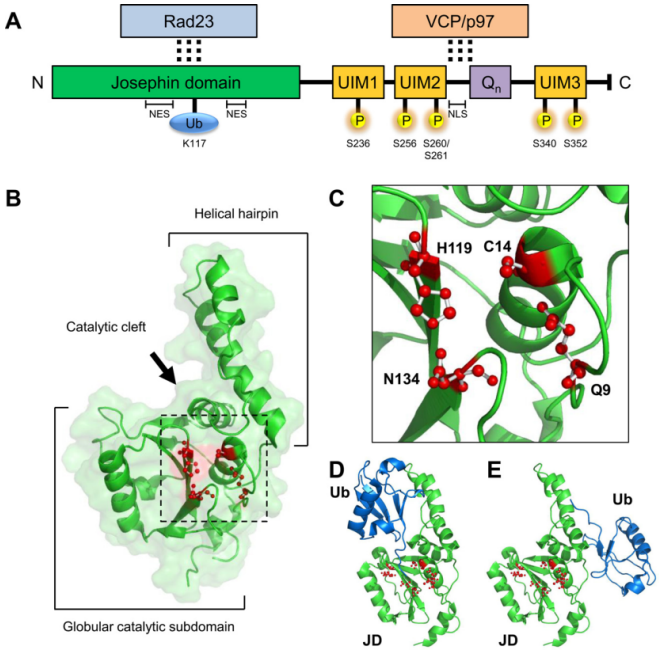

Fig. 1.3 Domain architecture, structure and post-translation modifications of AT3 3UIM isoform. (A) Schematic representation of AT3 3UIM. (B) Structure of the JD solved by NMR (PBI code 1YZB) where the globular catalytic subdomain, the helical hairpin and the catalytic residues (in red) are shown. (C) Close-up of the catalytic cleft with in red the catalytic triad. (D, E) JD Ub-binding sites: site 1 is located close to the catalytic cleft and site 2 on the opposite surface (PDB code: 2JRI) [41].

1.3.1 Ataxin-3 functional and biological roles

1.3.1.1 Role as a deubiquitinating enzyme in Ubiquitin-Proteasome Pathway (UPP)

Plenty of experimental evidence suggests for AT3 a role in the ubiquitin-proteasome pathway (UPP), one major mechanism in protein turnover [94]. Short-lived or damaged proteins can undergo a covalent modification called ubiquitination (i.e. covalent attachment of Ub molecules, either K48- or K63-polyUb chains to lysine residues) that targets them to the proteasome for degradation. It has been observed that inhibition of the DUB activity of AT3 in mammalian cells leads to an increase in polyubiquitinated proteins to a degree similar to what is observed when the proteasome is inhibited [95]. AT3 is able to bind polyUb chains through the UIMs located at the C-terminal region, interacting with both K48- and K63-linked chains in a UIM-dependent manner [74, 96-98]. There is, however, a preference for chains of no less than four Ub monomers, and K48-linked polyUb chains of four or more monomers are the ones involved in the targeting of proteins for proteasomal degradation [74, 78, 98, 99]. AT3 has also been shown to be able to bind polyubiquitinated proteins in neural cells in a UIM-dependent way [95]. Many results suggest that AT3 functions as a polyUb-editing protease, shortening polyUb chains rather than favoring their complete disassembly in order to yield free Ub [74, 98, 100-102]. The increase in polyubiquitinated proteins observed when AT3 catalytic activity is inhibited occurs only when the UIMs are intact, suggesting that they are important in the presentation of substrates to the JD [95]. UIMs may help to recruit the polyubiquitinated substrates and position those substrates relative to the catalytic site in a way that allows for a sequential editing [78, 98]. The contribution of the third UIM

present in one AT3 isoform for the overall ubiquitin protease activity is not clear, as isoforms with two or three UIMs display similar enzymatic activity *in vitro* [84, 96]. Importantly, Burnett and Pittman [100] reported that AT3 is able to edit K48-linked polyUb chains from a polyubiquitinated model protein (^{125}I-lysozyme) *in vitro*, at the same time blocking its proteasome-dependent degradation. Therefore, it has been proposed that AT3 partially deubiquitinates proteins and prevents their degradation by binding through the UIMs, while possibly maintaining their polyUb degradation signals. However, Winborn and coworkers [98] observed that AT3 preferentially cleaves K63-linked chains and chains of mixed K48 and K63 linkage, suggesting that AT3 may function as a regulator of topologically complex polyUb chains. Actually, AT3 proteolytic activity *in vitro* is very slow [80] [98], suggesting that external factor(s) may be required for optimal proteolysis [80, 103]. Moreover, as for many DUBs, the actual substrate(s) targeted by AT3 in the physiological context remains elusive, thus limiting understanding of its function [103].The low activity observed for AT3 *in vitro* may also be explained by the absence of the endogenous substrate, since many DUBs require association with the proper substrate(s) to effect a transition to an optimal catalytic-competent conformation [104]. The first *in vivo* clues to AT3 function as a DUB came from studies involving AT3 knockout (KO) mice [99]. Compared to wild-type animals, AT3 KO mice showed no significant morphological or behavioral differences. Noteworthy, however, is the observation that AT3 KO mice had increased levels of ubiquitinated proteins, a fact that substantiates AT3 role as a DUB *in vivo*. The absence of deleterious physiological consequences was suggested to be due to redundancy existing among DUBs [99]. Taken together, these results show that AT3 acts as a DUB and that it is likely associated with the UPP, though its precise biological role remains unclear. Nevertheless, the

deubiquitinating activity may be important in a variety of cellular processes, taking into account that ubiquitination, in all its alternative linkage forms, serves many different cellular functions other than targeting proteins for proteasomal degradation [98, 105].

1.3.1.2 Role in Endoplasmic Reticulum-Associated Degradation (ERAD)

AT3 has been shown to interact with p97/valosin-containing protein (VCP) through the C-terminal region [78, 106-109] and with the Ub-like domains of the human homologs of the yeast DNA repair protein Rad23, HHR23A and HHR23B, through the ubiquitin-binding site 2 of the JD (in the face opposite to the catalytic site, Fig. 1.3 D) [75, 110]. Both p97/VCP and HHR23A and B have been implicated in many different biological processes, including the UPP; they have both been linked to the shuttling of polyubiquitinated substrates to the proteasome for degradation, particularly in endoplasmic reticulum-associated degradation (ERAD). ERAD is the system that mediates the ubiquitination of misfolded proteins or unassembled complex constituents present in the secretory pathway and their export to the cytosol for degradation by the proteasome [73, 74, 94, 111, 112]. While AT3 has been associated with the ERAD, there is dispute regarding whether AT3 promotes or decreases degradation by this pathway [109, 112]. AT3 has been found to associate with the proteasome itself through its N-terminal region [94], but a study showed that this interaction may not be very strong or even direct [105]. Functioning with these interactors, AT3 may act in a number of different ways, (a) trimming polyUb chains of a substrate, thus facilitating the subsequent disassembly of the chain by proteasome-associated DUBs, (b) editing polyUb chains in order to guarantee that the substrate is correctly

targeted for degradation, or (c) functioning as a transiently associated subunit of the proteasome and recognizing some of its substrates [106, 113].

1.3.1.3 Involvement in transcription regulation

A different aspect of AT3 function concerns its possible involvement in transcription regulation. In particular, it has been reported that AT3 is able to repress transcription in different manners: by inhibiting transcription activators as the cAMP response element-binding protein (CREB)-binding protein (CBP), p300 and p300/CBP-associated factor (PCAF) [114]; by decreasing histone acetylation [115] through interaction with histone deacetylase 3 (HDAC3), nuclear receptor co-repressor (NCor) [115] and histones [114]. Further, it has been proposed that AT3 deubiquitinating activity may interfere with the turnover of transcription regulators with which it interacts, thereby influencing repressor complex formation and activity [115, 116].

1.3.1.4 Role in the organization of the cytoskeleton

It is also known that AT3 interacts with components of the cytoskeleton such as tubulin, microtubule-associated protein 2 (MAP2) and dynein for aggresome formation as described in the following section (Par. 1.3.1.5) [100]. However, these interactions may not be limited to a possible role in aggresome formation. Recent findings indicate that AT3 may play a role in the organization of the cytoskeleton itself, since its absence leads the disorganization of the several cytoskeleton constituents (microtubules, microfilaments and intermediate filaments) and a loss of cell adhesions [117].

1.3.1.5 Role in aggresome formation

Another role associated with quality control mechanisms of the cell AT3 may play is in aggresome formation. The aggresome-autophagy pathway sequesters misfolded proteins and facilitates their clearance when the chaperone and ubiquitin proteasome systems are overwhelmed. The formation of the aggresome is a multi-step process involving recognition of misfolded and aggregated protein, coupling to the dynein motor complex, and retrograde transport along microtubules to the microtubule-organizing center (MTOC) [118, 119]. Defective proteins accumulated in aggresomes are then degraded by lysosomes, contributing to the maintenance of cellular homeostasis [120]. This suggests that these structures actually play a physiological role. Endogenous AT3 seems to be also involved in the regulation of aggresome formation, as shown by its capability to co-localize with aggresome and preaggresome particles [100]. AT3 also associates with dynein, histone deacetylase 6 (HDAC6) and tubulin, constituents of the complex responsible for the transport of misfolded proteins to the MTOC [100, 121]. It has been proposed that AT3 may protect misfolded proteins before they reach the MTOC, or stabilize proteins involved in the transport [100]. Recently it was also demonstrated that AT3 is required for HDAC6 recruitment of protein aggregates to aggresomes [122]. In fact, HDAC6 binds polyubiquitinated proteins through the unanchored C-terminal diglycine motif of ubiquitin that are likely to be released by the deubiquitinating activity of AT3 [122].

1.3.2 Ataxin-3 aggregation

The mechanism by which polyQ-expanded AT3 leads to MJD pathogenesis has not been clarified yet. Although wild-type AT3 displays a

ubiquitous distribution, in MJD patient expanded AT3 accumulates as nuclear inclusions (NIs) only in neurons [87]; recently, however, axonal inclusions have also been observed in patients' brains, in fibers known to degenerate in MJD [123].

Further studies suggest that expanded AT3, like any other polyQ expanded protein, tends to form aggregates, as a result of polyQ expansion-induced misfolding and consequent transition to aggregation-prone conformations [124-130]. As for most amyloid-forming proteins, several pathways may drive the conversion of the soluble protein to amyloid aggregates, through the formation of different conformationally altered monomeric or self-assembled multimeric species [131], being the small aggregates or oligomers the ones envisioned as the species actually causing cytotoxicity.

Several works have focused on the aggregation mechanism of AT3, highlighting the complexity of this process. To date, it has been shown that the isolated JD has an intrinsic amyloidogenic potential, which results in the capability of the wild-type protein to aggregate under particular conditions. This implies that the aggregation pathway consists of two steps. The first gives rise to SDS-soluble oligomers and protofibrils as a consequence of aberrant interactions between the JDs; the second is accessible just to variants carrying expanded polyQs and results in the formation of mature, SDS-insoluble fibrils that are characterized by the formation of hydrogen bonds among polyQ glutamine side-chains [132-135] (Fig. 1.4). Expanded variants display the fastest aggregation kinetics, suggesting that the polyQ tract also affects the mode of JD aggregation [133]. JD plays therefore a key role in the early conformational changes modulating the aggregation of both expanded and non-expanded AT3 [133, 136, 137] and, interestingly, the surfaces involved in

the self-association overlap with the functionally relevant ubiquitin binding sites 1 and 2 [79, 138]. This observation provides a direct link between protein function and aggregation and a role for intracellular interactors in protecting against AT3 self-assembly, in keeping with the fact that Ub reduces *in vitro* aggregation of the JD [138]. The C-terminal region of AT3 may also represent a bridge between physiological interactions and aggregation. When expanded, the polyQ may provoke aberrant protein interactions leading to AT3 aggregation. The connection between normal molecular interactions and aggregation may help explain the failure of non-expanded protein to self-aggregate in the crowded cell environment [132].

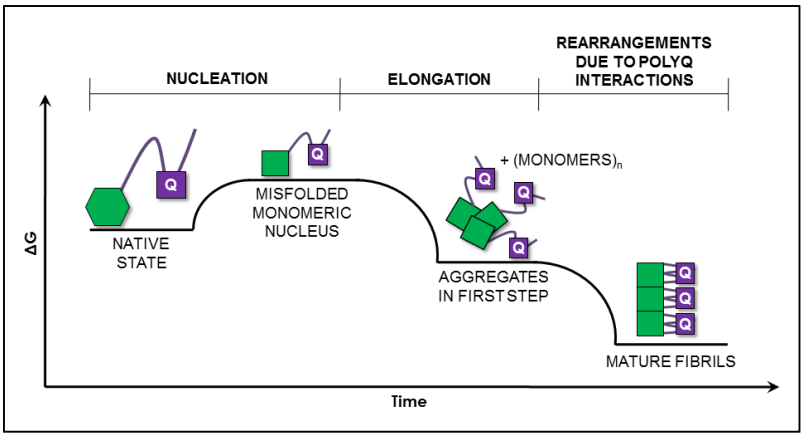

Fig. 1.4 Scheme of AT3 fibrillogenesis. In native AT3 the JD is represented as a hexagon and the disordered tract, including the polyQ (square), as a non-structured tail. AT3 fibrillization follows a two-step aggregation process. The first consists in the formation of a misfolded monomeric nucleus that is thermodynamically less stable with respect to the native protein. This conformational change is promoted by a structural rearrangement that does not involve the polyQ and leads to a first elongation step, driven by monomer addition. Only in the presence of an expanded polyQ, AT3 undergoes a further aggregation step that leads to an increase in size and stability of the fibril [133].

1.4 THE *SACCHAROMYCES CEREVISIAE* MODEL SYSTEM FOR NEURODEGENERATIVE DISEASES

The budding yeast *Saccharomyces cerevisiae* has long been used as a eukaryotic model organism, mostly due to its ease of manipulation and amenability to genetic modifications. The use of yeast as a model organism was recently expanded to the dissection of the molecular mechanisms of human diseases, either by directly studying an endogenous protein orthologue of a human counterpart involved in the disease or through the heterologous expression of human disease-associated proteins. Though several aspects of the disease are beyond the reach of a unicellular organism like yeast, many processes and pathways are highly conserved in this organism.

In 1996, *S. cerevisiae* became the first eukaryote to have its 1.3×10^7 base pair-long genome sequenced. By comparison, the human genome has 3.08×10^9 base pairs but only 3 to 5 times as many genes. At least 60% of yeast genes have statistically robust human homologues or at least one conserved domain with human genes [139, 140]. Genomic homology explains the conservation of fundamental cell biological processes between yeast and mammalian cells. Yeast cells, like mammalian cells, are eukaryotic and are distinguished from bacteria and Archaea by the presence of membrane-bound organelles, including a nucleus. As a model system, yeast offers the advantage of a short generation time (1.5–3 hours), and grows in a highly reproducible and genetically stable way. It is also a scalable system and therefore suited for highthroughput genetic and small-molecule screens. Most important is its genetic tractability: its DNA is easily transformed, and homologous recombination is efficient [141, 142].

Yeast cells recapitulate fundamental aspects of eukaryotic biology, including a distinctive process of cell division and genetic transmission, transcriptional regulation, biogenesis and function of cellular organelles, protein targeting and secretion, cytoskeletal dynamics and regulation, and cellular metabolism.

A few conserved aspects of cellular biology deserve particular mention in the context of neurodegenerative diseases (Fig 1.5).

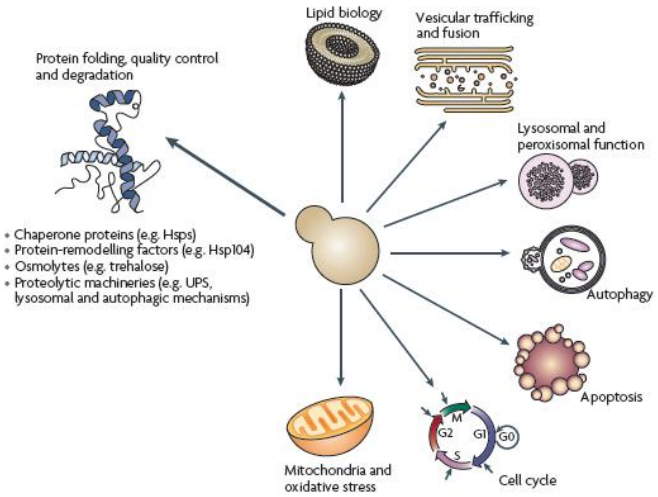

Fig. 1.5 Conserved cellular biology in yeast. Numerous cellular pathways of high relevance to neurodegeneration are conserved in yeast [143].

The most common neurodegenerative diseases, including Alzheimer's disease (AD) and Parkinson's disease (PD), are associated with intracellular proteinaceous aggregates. These processes are readily studied in yeast because there is high conservation of the cellular protein quality system [144]. Yeast amyloid shows similar biochemical properties to amyloid in

neurodegenerative diseases, including recognition by Congo Red and ThT, β-strands running perpendicular to the fiber axis, and the formation of molten preamyloid oligomeric species that react with the same conformation-specific antibody [145].

Mitochondrial dysfunction and oxidative stress are heavily implicated in neurodegeneration. In yeast, as in mammalian cells, the central organelle for the production of reactive oxygen species (ROS) is the mitochondrion. The ability of yeast to grow in fermentative states allows for the analysis of mitochondrial defects that would be lethal in mammalian cells [146].

The secretory pathway, through which proteins are translocated from the endoplasmic reticulum (ER) to the Golgi complex and then trafficked in vesicles to the plasma membrane, is of particular importance in neurons that need to transport proteins over long distances to nerve terminals and that release neurotransmitters by vesicular fusion. Yeast has homologues of synaptobrevin, syntaxin and synaptosomal-associated protein 25 (SNAP25) among other key mammalian components of this pathway [147]. Importantly, ER stress caused by the accumulation of misfolded proteins in vesicular trafficking has been heavily implicated in neurodegeneration [148, 149].

Moreover, yeast has conserved mechanisms of cell death and survival that are likely to be relevant to neuronal loss. Apoptotic and non-apoptotic cell death mechanisms have both been implicated in neurodegeneration [150]. As in mammalian cells, an apoptosis-like process has been described in yeast that involves chromatin condensation, altered mitochondrial membrane potential, release of cytochrome c, exposure of phosphatidylserine at the plasma membrane and labeling by TUNEL (TdT-mediated dUTP nick-end labeling) staining [151]. Although the existence of a programmed cell death pathway in a unicellular organism may seem surprising, there are benefits in a clonal

population for those cells that are accumulating oxidative damage to undergo cell death rather than to deprive genetically identical neighboring cells of nutrients [152].

Enormous attention has been directed recently to the potential role of autophagy in neuronal survival, putatively by degradation of misfolded proteins and elimination of damaged organelles. Genetic analysis in yeast played a pivotal part in identifying the effector machinery of autophagy, which consists of the highly conserved ATG proteins downstream of the target of rapamycin (TOR) kinase [153].

As a unicellular organism with a cell wall, the most obvious limitation of yeast as a model system for neurodegenerative disease is in the analyses of disease aspects that rely on multicellularity and cell–cell interactions. Such interactions include immune and inflammatory responses, synaptic transmission and glial–neuronal interactions, among others. Mammalian cells have diversified to include cellular specializations without homology in yeast. Although the basic elements of the unfolded protein response to ER stress are conserved in yeast, the response is far more complex in mammalian cells [154]. Many neuronal specializations that are likely to be of great importance to neurodegeneration — for example, axonal transport, neurotransmitter release and myelination — cannot be recapitulated in yeast. Nevertheless, fundamental aspects of these biological functions may be conserved in yeast. For example, although yeast cells do not release neurotransmitters, they traffic proteins in vesicles and have conserved endo- and exocytic mechanisms and, although yeast cells do not produce myelin, they have conserved lipid biosynthesis pathways.

1.4.1 Neurodegenerative disorders studied in yeast

Modeling human disease in yeast follows one of two general approaches, depending on whether a yeast homologue exists. When a human disease-related gene has a yeast homologue, the gene can be disrupted or overexpressed to determine the loss- or gain-of-function phenotypes, respectively [141, 142]. For example, Yfh1p is the yeast orthologue of human frataxin whose decreased expression and/or function is associated with Friedreich's ataxia (FRDA), a neuro- and cardiodegenerative disorder [155]. Studies with Yfh1p were decisive in determining the function of frataxin. Absence of Yfh1p, likewise of its human orthologue, results in mitochondrial iron accumulation, mitochondrial dysfunction, and oxidative stress [156]. Other proteins that were directly studied in yeast are associated with Batten's [157] and Niemann-Pick's [158] diseases, Ataxia telangiectasia [159], and Hereditary Spastic Paraplegia [160]. Though yeast has no true orthologues of the human prion protein (PrP), responsible in its prion form for the Creutzfeldt-Jakob disease, it has prions, with at least three forms [URE3], [PSI+], and [PIN+], that show similarities concerning transmission of phenotype in a protein-only mode [161].

For human disease-related genes that do not have a yeast homologue and for which the disease process is clearly a toxic gain of RNA or protein function, the human gene is expressed in yeast (the so-called "humanized yeast") and screens are designed against any relevant phenotypes that result from this expression. Typically, neurodegenerative diseases in this category are autosomal dominant and involve aggregation of the protein encoded by the mutated gene, strongly implicating protein misfolding and the formation of a toxic protein species (whether large aggregates or oligomers) in disease

pathogenesis. For example, yeast cells provided a useful system for investigating amyotrophic lateral sclerosis (ALS) through TDP-43 (TAR DNA binding protein) and FUS/TLS (fused in sarcoma/translocated in liposarcoma) expression. Similarly to that observed in ALS patients, yeast expressing human TDP-43 exhibit cytoplasmic TDP-43 aggregates that correlate with toxicity [162]. Likewise, expression of FUS/TLS in yeast was recently described to form protein aggregates and to induce cytotoxicity, with two ALS-associated mutants showing increased cytotoxicity [163]. Several other proteins involved in neurodegeneration, namely, α-syn and Lrrk2 in PD, tau and Aβ in AD, and htt with expanded polyQ tracts in HD, have been studied in yeast through heterologous expression [164-168] (Table 1.3)

Table 1.3 Proteins associated with human neurodegenerative disorders studied in yeast [169]

Disease	Protein(s) involved	Yeast orthologue
Batten's disease	CLN3	YHC3/BTN1
Friedreich's Ataxia	Frataxin	YFH1
Ataxia-telangiectasia	ATM	TEL1, MEC1
Niemann-Pick disease	NPC1	NCR1
Hereditary Spastic Paraplegia	mAAA-proteases (Afg312 and paraplegin)	mAAA proteases (Yta10 and Yta12)
Creutzfeldt-Jakob disease	PrP	—
Amyotrophic lateral sclerosis	SOD1	SOD1
	TDP-43	—
	FUS/TLS	—
Parkinson's disease	α-synuclein	—
	Lrrk2	—
Alzheimer's disease	Amyloid β	—
	tau	—
Huntington's disease	Huntingtin	—

—: No orthologue.

1.4.1.1 Yeast model for polyglutamine disorders: HD model

The first yeast model of polyQ diseases involved the expression of exon 1 of huntingtin with different polyQ lengths fused to GFP [170, 171]. Although the Q25 htt variant (corresponding to a normal polyQ length) did not aggregate, insoluble inclusion formation increased with the increase in polyQ length [170], recapitulating results obtained in cultured mammalian cells and animal models [172-174].

The correlation between aggregation and toxicity of htt fragments in yeast was found to be dependent on the sequences flanking the polyQ stretches, as well as on the existence of specific interacting proteins of the yeast strain expressing it, in particular the prion composition of the cell [175-178].

Specifically, the htt exon 1 with expanded polyQ tracts was shown to impair protein homeostasis of the ER [166] and endocytosis [179, 180], cause transcriptional deregulation [181], increase ROS production by affecting mitochondrial function and morphology [164, 165, 182]. Stimulation of mitochondrial biogenesis was able to rescue mitochondrial dysfunction and cellular toxicity, indicating that mitochondria contribute significantly to polyQ toxicity [183]. In addition to mitochondrial dysfunction, the occurrence of DNA fragmentation and caspase activation pointed to the activation of an apoptotic pathway by htt polyQ tracts [165]. The same authors reported a derangement in the cell cycle that was also related to polyQ cytotoxicity. Another consequence of the polyQ expression in yeast is the alteration of the cellular concentration of several metabolites, namely, alanine, glycerol, glutamine, and valine. Alterations in these metabolites were proposed as promising biomarkers for HD [184] (Fig. 1.6).

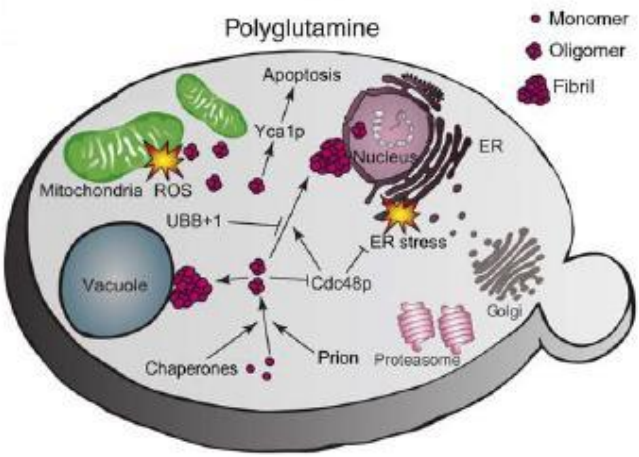

Fig. 1.6 Yeast models for polyglutamine disorders. Proteins with expanded polyglutamine residues form chaperone and prion-dependent oligomeric and fibril-like aggregates, causing damage to mitochondria and the ER, leading to oxidative stress and cell death. Oligomeric aggregates can be partially detoxified by transporting them to perinuclear and perivacuolar collection points [185].

Once validated, yeast models of HD were used as platforms to unravel the molecular basis of the disease [164, 180]. An important advance was the identification of the kynurenine pathway in a yeast screen for modifiers of polyQ toxicity [164]. This pathway is involved in tryptophan degradation and is activated by mutant htt expression, resulting in higher levels of two neurotoxic metabolites, 3-hydroxykynurenine and quinolinic acid, consistent with observations in mammalian models and HD patients [186].

Yeast models of HD were also used in drug screens and led to the identification of small molecules that showed potential as therapeutic tools to ameliorate polyQ toxicity in higher eukaryotes [187-190]. In a recent study, a HD yeast model was also used to dissect the protective effect and mode of

action of curcumin, a polyphenol present in the spice turmeric and known to have broad biological and medicinal effects, including efficient anti-oxidant, anti-inflammatory, and anti-proliferative activities [191].

1.5 THERAPEUTIC STRATEGIES

Nowadays, it is common opinion that the central event in the etiology of the most common protein misfolding diseases is the conversion of soluble peptides and proteins into amyloid aggregates, through the formation of small aggregates or oligomers that are the ones envisioned as the species causing cytotoxicity. Consequently, many therapeutic strategies have been aimed at reduction of amyloid production; inhibition of amyloid aggregation and/or destabilization of aggregated species, and enhancement of its clearance [192]. The discovery of molecules that inhibit protein deposition or reverse fibril formation could certainly open new avenues for developing therapeutic strategies aimed to prevent or control the corresponding amyloid-related diseases. Thus, many efforts in the last decade have been devoted to the inhibition of the polymerization process leading to amyloid formation as a potential preventive treatment for misfolding diseases.

Numerous compounds have been found to inhibit specific amyloid fibril formation *in vitro* [193-196], particularly in relation to Aβ deposition [197], formation of proteasome resistant forms of the PrP [198], and htt aggregation [194]. To date, no effective treatment has been developed for SCA3 disease and no compounds were tested on AT3 aggregation process. Consequently, as with many hereditary diseases, it remains incurable and invariably fatal [199, 200]. For this reason, we focus our attention to study two different classes of compounds which have been found to influence the polymerization process of many amyloid proteins: (i) epigallocatechin-3-gallate (EGCG) and (ii) tetracycline.

1.5.1 Epigallocatechin-3-gallate (EGCG)

Tea is the most widely consumed beverage after water. Green tea preparation precludes the oxidation of leaf polyphenols which are thought to contribute to the health-promoting effects. Tea polyphenols, known as catechins, usually account for 30% to 42% of the dry weight of the solids in brewed green tea. The four major catechins (flavan-3-ols) are (−)–epigallocatechin-3-gallate (EGCG) (Fig. 1.7), (−)-epigallocatechin (EGC), (−)-epicatechin-3-gallate (ECG), and (−)epicatechin (EC). EGCG represents the most abundant tea catechins (50% to 80% of total catechins) [201-203]. These four catechins act as potent antioxidants via direct scavenging of reactive oxygen and nitrogen species (ROS and RNS), induction of defense enzymes and binding and chelation of divalent metals, such as copper and iron [204]. In particular, EGCG potently inhibited Fe^{2+}-mediated DNA damage and iron ascorbate-promoted lipid peroxidation of brain mitochondrial membranes. *In vivo*, EGCG increases expression and activity of antioxidant enzymes, such as glutathione peroxidase, glutathione reductase, superoxide dismutase (SOD) and catalase but inhibits pro-oxidative ones, such as monoamine oxidase (MAO)-B and nitric oxide synthase (NOS) [205]. Furthermore, EGCG was reported to pass the blood–brain barrier in mammals [206] and to be safe for humans when tested in clinical studies [207].

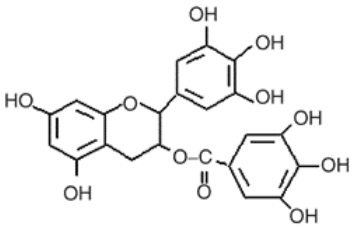

Fig 1.7 Chemical structure of EGCG.

However, EGCG does not only influence neurodegenerative processes via modulation of cellular signal transduction pathways and ROS production, but also directly acting on amyloid species formation. Ehrnhoefer and coworkers demonstrated that green tea polyphenols are able to modulate early steps in the aggregation process of an amyloidogenic polyQ-containing protein using an *in vitro* model of HD. The inhibitory effect on the assembly of mutant htt exon 1 fragments in the cell-free assays is concentration-dependent and does not require the antioxidant properties of the polyphenols [189].

Moreover, Wanker and coworkers demonstrated that EGCG is a potent inhibitor of α-syn fibrillogenesis. It binds to natively unstructured α-syn monomers and prevents their conversion into stable, β-sheet–rich structures [208], which are a prerequisite for nucleation-dependent amyloid fibril assembly [209]. Thus, the compound interferes with a very early step in the amyloid formation pathway and suppresses the assembly of on-pathway amyloidogenic oligomers and protofibrils [210]. EGCG seems to inhibit amyloid fibrillogenesis because it stabilizes the unstructured state of the natively unfolded α-syn protein and reinforces the autoinhibitory intramolecular interactions in the protein [211]. Instead of amyloid fibrils, highly stable spherical oligomers are formed in EGCG-treated aggregation reactions, indicating that the compound redirects aggregation-prone molecules into an assembly pathway, distinct from the amyloid formation cascade [208]. In the same way, EGCG also redirects $A\beta_{42}$ aggregation cascades and thus prevents the formation of toxic, β-sheet–rich aggregation products such as amyloid oligomers or protofibrils [10, 208]. In a subsequent study, Wanker demonstrated that EGCG has the ability to convert large, mature α-syn and amyloid-β-fibrils into smaller, amorphous protein aggregates that are non-toxic to mammalian cells. Mechanistic studies revealed that the compound directly

binds to β-sheet-rich aggregates and mediates the conformational change without their disassembly into monomers or small diffusible oligomers [212].

1.5.2 Tetracycline

Tetracyclines (TCs) are a group of structurally related antibiotics discovered in the late 1940s. The first members of this family, chlortetracycline and oxytetracycline were isolated from *Streptomyces aureofaciens* and *Streptomyces rimosus*. They were later followed by the discovery of other natural TCs [213]. The basic chemical structure of TCs is represented by the partially saturated naphthacene carboxamide nucleus, composed of four linear fused six-membered carbocyclic rings (Fig. 1.8).

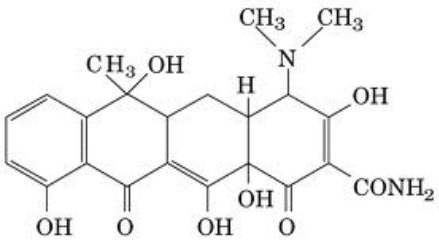

Fig 1.8 Chemical structures of tetracycline.

Tetracyclines cross the blood brain barrier and are already used in clinical practice offering the advantage of a safe toxicological profile and well characterized pharmacological properties [214-216]. The indications of non-antimicrobial activities of these drugs have raised considerable interest and triggered clinical trials for a number of different pathologies. In fact, they act as pluripotent drugs that affect many mammalian cell functions including proliferation, migration, apoptosis and matrix remodeling [217].

About 10 years ago, it was reported for the first time that tetracyclines inhibit the aggregation of prion protein fragments and Aβ, destabilizing their aggregates and promoting their degradation by proteases [195, 218]. In particular, tetracycline is able to sequester Aβ oligomers and prevent further progression of the amyloid fibril growth, resulting in significant reduction of peptide toxicity. Tetracyclines were also found to reduce the resistance of $A\beta_{1-42}$ amyloid fibrils to trypsin digestion [195] and to bind to amyloid fibrils of PrP, hinder their assembly, and revert the protease resistance of PrP aggregates extracted from brain tissue of patients with Creutzfeldt-Jacob disease [215, 218]. In addition, these drugs have been described to behave as fibril disrupters. In α-synucleopathies, including Parkinson's disease, studies have shown that tetracycline dose-dependently inhibits fibrillogenesis of α-syn and destabilizes preformed fibrils *in vitro* [219]. There are a few works regarding the action of tetracyclines on HD models, but the results are conflicting and it is not clear if these compounds are able to reduce htt aggregation [220, 221].

Actually, the use of TCs to treat amyloidoses affects the main pathological target, such as aggregation and deposition of the misfolded proteins, but they may also contribute to improve other pathological events, concurrent with amyloid deposit formation, including inflammation, ROS generation causing oxidative stress, apoptosis, and uncoupling of metal homeostasis [222].

Chapter Two

Interactions of ataxin-3 with its molecular partners in the protein machinery that sorts protein aggregates to the aggresome

2.1 AIM OF THE WORK

Even though its physiological role is not yet fully understood, it has been established that AT3 plays a role in the aggresome pathway. Aggresomes are perinuclear proteinaceous aggregates, close to the microtubule-organizing center (MTOC), to which misfolded protein is sorted *via* microtubules when proteasomes are overloaded or their function compromised [223]. In particular, it is known that AT3 co-localizes with aggresome and preaggresome particles and co-precipitates with dynein and histone deacetylase 6 (HDAC6) [100]. HDAC6 plays a pivotal role in the formation of aggresomes: in particular, the ubiquitin-binding activity of HDAC6 has been shown to mediate the transport of polyubiquitylated proteins along microtubule tracks to aggresomes [224]. Recently, it has been demonstrated that HDAC6 binds polyubiquitylated proteins through the unanchored C-terminal diglycine motif of ubiquitin that are likely to be released by the deubiquitinating activity of AT3 [122]. Furthermore, in a previous work we demonstrated that AT3 tightly binds tubulin dimers, the constituents of microtubules [121]. Microtubules are essential components of the cytoskeleton that play a major role in many cellular functions, including the retrograde transport of misfolded proteins to the aggresomes at MTOC [225]. Our investigations are aimed at providing further insight into the mode of interaction of AT3 with the protein components that are involved in sorting aggregated proteins to the aggresome. In particular, by taking advantage of Small Angle X-ray Scattering (SAXS) and Surface Plasmon Resonance (SPR) methods, we want to model the scaffold of the AT3-tubulin complex and to establish what specific AT3 site(s) or region(s) are involved in the tubulin binding. SPR experiments can also provide evidence of direct binding of AT3 to HDAC6, in order to better

understand the role of the individual components of the machinery that sorts proteins to the aggresome.

2.2 EXPERIMENTAL PROCEDURES

Cloning and expression of AT3 variants

The truncated forms $AT3_{1-182}$ and $AT3_{1-291}$ were cloned in fusion with glutathione S-transferase in a pGEX-6P-1 (GE Healthcare LifeSciences, Little Chalfont, UK) as previously described [121]. The truncated variants $AT3_{182-362}$, $AT3_{1-244}$, $AT3_{1-319}$ were obtained by PCR reactions using 5'-phosphorylated oligos and the construct pGEX6P1/AT3Q24 as a template. These AT3 variants were expressed in *E. coli* strain BL21-*CodonPlus* (DE3)-RIL *(E. coli B F– ompT hsdS (rB–mB–) dcm+ Tetr gal* λ (DE3) *endA Hte [argU ileY leuW* Cam^r*]* (Stratagene, La Jolla, CA, USA) as GST-fusion proteins containing a PreScission Protease recognition site. The wild type AT3Q24 was cloned in a pQE30 vector (Qiagen Hamburg GmbH, Hamburg, Germany) and expressed as a His-tagged protein as previously described [135].The variants AT3Q6 and AT3Q24-3UIM were obtained by PCR reactions using 5'-phosphorylated oligos and the construct pQE30/AT3Q24 as template. These three variants were expressed in SG13009 (*E. coli* K12 Nal^S, Str^S, Rif^S, Thi^-, Lac^-, Ara^+, Gal^+, Mtl^-, F^-, $RecA^+$, Uvr^+, Lon^+; Qiagen Hamburg GmbH, Hamburg, Germany) as His-tagged proteins.

Purification of AT3 variants

The procedures adopted to purify either GST- or His-tagged AT3 variants shared the initial steps, the only difference being that for the GST-tagged construct (i.e. AT3Q24 and AT3182-362), cells were grown at 37 °C in LB-ampicillin medium, for the His-tagged in LB-ampicillin-kanamycin medium.

In either case, they were induced with 50 µM IPTG at A600 0.8 for 3 h at 30 °C. To obtain crude extracts, pelleted cells were resuspended in lysis buffer (5 ml/g wet weight; 25 mM potassium phosphate, pH 7.2, 150 mM NaCl, 0.5 mM PMSF, 5 mM dithiothreitol, 100 mM MgCl2) plus 1 mg/ml lysozyme and incubated for 30 min at 4 °C. The cell suspension was then sonicated in 3 pulses of 30 s each. DNase I (0.2 mg/g of cells, wet weight) and 1% Triton X-100 were added, and the sample further incubated for 30 min at room temperature. Finally, it was centrifuged for 30 min at 20,000 × g. The supernatant was filtered through a 0.45 µm pore size SFCA membrane (Corning). When purifying the GST-tagged variants, it was then incubated for 1 h at 4 °C with Glutathione Sepharose 4 Fast Flow affinity resin (GE Healthcare Life Sciences, Little Chalfont, England) under shaking. Then, the sample was loaded onto a column, washed with 20 bed volumes of Wash Buffer (25 mM potassium phosphate, pH 7.2, 150 mM NaCl, 0.5 mM phenylmethanesulfonyl fluoride) and equilibrated with 10 volumes of Cleavage Buffer (50 mM Tris–HCl, pH 7.0, 150 mM NaCl, 1 mM EDTA, 1 mM dithithreitol). To elute bound protein, the resin was incubated at 4 °C overnight under shaking with PreScission Protease (80 U/ml resin) (GE Healthcare Life Sciences, Little Chalfont, England), except for the AT3/JDΔ variant that was eluted as a GST-tagged protein with Elution buffer (50 mM Tris-HCl, 10 mM reduced glutathione, pH 8.0). When purifying the His-tagged variants, the procedure by Chow and coauthors [226] was followed with minor modifications. Briefly, after filtration through the SFCA membrane, the supernatant was loaded onto HisPur™ Cobalt Resin (Thermo Fisher Scientific, Rockford, IL, USA) and washed with 20 bed volumes of Wash Buffer (25 mM potassium phosphate, pH 7.4, 150 mM NaCl, 2 mM phenylmethanesulfonyl fluoride, 10 mM imidazole, 10% glycerol, 0.1% Triton X-100, 1 mM 2-mercaptoethanol). The bound protein was

then eluted with Elution buffer (25 mM potassium phosphate, pH 7.4, 150 mM NaCl, 2 mM phenylmethanesulfonyl fluoride, 150 mM imidazole, 10% glycerol, 0.1% Triton X-100, 1 mM 2-mercaptoethanol). Before each experiment, protein preparations were thawed, centrifuged at 15,000 × g for 15 min at 4 °C to remove aggregates and then equilibrated with PBS buffer (25 mM potassium phosphate, pH 7.2, 0.15 M NaCl) using Zeba™ Spin Desalting Columns (Thermo Fisher Scientific, Rockford, IL, USA). Protein content was determined using Coomassie brilliant blue G-250 (Thermo Fisher Scientific, Rockford, IL, USA) and BSA as a standard protein.

Small-Angle X-Ray Scattering (SAXS)

For AT3Q24-tubulin complex formation and SAXS measurements, tubulin dimer (Tebu-bio TEBU-BIO, Boechout, Belgium) was resuspended in PBS buffer. Complex formation between AT3Q24 and tubulin dimer takes place by incubating proteins for 15 min at room temperature under shaking. SAXS patterns of AT3Q24, tubulin and AT3Q24-tubulin complexes in PBS buffer were recorded at X33 EMBL beamline on the storage ring DORIS-III (Hamburg, Germany) [227]. The protein concentration of the measured samples ranged between 2 and 10 mg/ml. The data were recorded at 10 °C using pixel 1M PILATUS detector (DECTRIS, Switzerland) (X33) at a sample-detector distance of 2.7 m, respectively, and a wavelength of $\lambda = 0.15$ nm, covering the range of momentum transfer $0.12 < s < 5.5$ nm-1 ($s = 4\pi \sin\theta/\lambda$, where 2θ is the scattering angle). No measurable radiation damage was detected by comparison of four successive time frames with 30 sec exposures. The data were averaged after normalization to the intensity of the incident beam, corrected for the detector response, and the scattering of the buffer was subtracted. All data manipulations were performed by using the program

package PRIMUS [228]. The forward scattering I(0) and the radius of gyration Rg were evaluated using the Guinier approximation [229] assuming that at very small angles (s < 1.3/Rg) the intensity is represented as I(s) = I(0) exp(-(sRg)2/3). These parameters were also computed from the entire scattering patterns using the program GNOM [230] which provides maximum particle dimensions Dmax and the pair distance distribution functions p(r). The molecular weights (MWexp) of the solutes were estimated from the forward scattering by normalization against reference solutions of bovine serum albumin. The excluded (Porod) volumes of hydrated particles were computed as in [231]:

$$V_p = 2\pi^2 I(0) / \int_0^\infty s^2 I(s) ds \qquad (1)$$

Prior to the calculation, an appropriate constant was subtracted from each data point to force the s-4 decay of the intensity at higher angles following Porod's law [231] for homogeneous particles. This procedure yields a “shape scattering” curve corrected for the unwanted scattering contribution from the internal structure. The program DAMMIF [232], a fast version of DAMMIN [233] used to reconstruct the low resolution shape of AT3Q24, tubulin and AT3Q24-tubulin complexes, represents the particle as a collection of M >> 1 densely packed beads inside a sphere with diameter Dmax. In DAMMIF, each bead is assigned to either the solvent or the particle and the latter is represented by a simple "phase" (non-solvent beads). Starting from a random string, simulated annealing is employed in DAMMIF to search for a model composed by interconnected compact phases, which fits to the experimental curve to minimize the overall discrepancy:

$$\chi^2 = \frac{1}{N-1}\sum_j \left[\frac{I(s_j) - c\ I_{calc}(s_j)}{\sigma(s_j)}\right]^2 \quad (2)$$

where N is the number of experimental points, c is a scaling factor and I_{calc}(sj) and σ(sj) are the calculated intensity and the experimental error at the momentum transfer sj, respectively (the ideal fit should correspond to χ values close to 1.0, however, in reality, values around 1.45-1.50 are acceptable). The results of multiple DAMMIF runs (20 runs) were averaged to determine common structural features using the programs DAMAVER [234] and SUPCOMB [235]. The aggregation states of the AT3Q24 and tubulin proteins were estimated from their excluded [231] volumes taking into account that for sufficiently large globular proteins the hydrated volume in nm^3 should numerically be about twice the molecular mass in kDa. Molecular modeling for the AT3Q24-tubulin complex was done using the NMR atomic model of the JD of AT3Q24 (PDB code; 1YZB [75]) and the crystallographic model of tubulin dimer (PDB code: 1TUB and 1SA0 [236, 237]) by manual docking to the *ab initio* model of the complex. The scattering pattern from the constructed model was calculated from its atomic coordinates by the program CRYSOL [238].

Surface Plasmon Resonance (SPR)

A BIACORE X system (GE Healthcare Life Sciences, Little Chalfont, England) was used to analyze molecular interactions by means of SPR. Tubulin (dimer) and HDAC6 proteins were coupled to a carboxymethylated dextran surface of two different CM5 sensor chips by using amine-coupling chemistry at surface densities of 4000 and 3500 resonance units, respectively. Appropriate, multiple concentrations of the interacting proteins (analytes in

BIAcore terminology) were injected at 25 °C (30 µl injections at a flow rate of 10 µl/min) in running buffer (10 mM HEPES, pH 7.4, 150 mM NaCl, 3 mM EDTA containing 0.005% (v/v) Surfactant P20). After injection, analyte solutions were replaced by running buffer at a continuous flow rate of 10 µl/min. Surface regeneration was accomplished by injecting 50 mM NaOH (10 µl/min; 0.5-min contact time). Each sensorgram was subtracted for the response observed in the control flow cell (no immobilized protein) and normalized to a baseline of 0 RU. The interaction rate constants were calculated by using the BIA evaluation 4.1 SPR kinetic software (GE Healthcare Life Sciences, Little Chalfont, England).

2.3 RESULTS

SAXS analysis of the tubulin-ataxin-3 complex

Previous findings have shown that ataxin-3 (AT3) is part of the transport machinery of misfolded proteins to the aggresome *via* microtubules [100]. We showed, in addition, tight binding of AT3 (dissociation constant of 50-70 nM) to tubulin dimers [121]. Here, we aim at providing a better understanding of such mode of binding, and consequently of the molecular mechanism by which AT3 fulfils such physiological role.

To obtain a structural description of the AT3Q24-tubulin complex, we resorted to a strategy based on SAXS measurements and molecular modeling validated by experimental data. We selected the conditions whereby both proteins are less prone to oligomerize and acquired and compared SAXS data for each of the isolated individual components, as well as for the complex.

The experimental curve for tubulin is shown in Fig. 2.1 A, upper panel. The estimated molecular weight of the solute (MW_{exp} = 280 $\pm$ 20 kDa) indicates that the protein is composed of three $\alpha\beta$-dimeric units (each monomer having a theoretical MW ~ 55 kDa) under the assayed experimental conditions. Accordingly, the excluded volume of the particle in solution (Porod volume) is V_p = 450 ± 20 × 10^3 Å^3, noting that for globular proteins the hydrated volume in Å^3 should numerically be about twice the molecular mass in Da. The experimental radius of gyration R_g and maximum size D_{max} (7.0 $\pm$ 0.3 nm and 25 $\pm$ 1 nm, respectively) point to an elongated particle structure. The low resolution shape of hexameric tubulin, reconstructed *ab initio* using DAMMIN [233] has the overall size of about 40 x 60 x 250 Å^3, fitting the experimental data with discrepancy χ = 1.05 (Fig. 2.1 A). High resolution modeling of the tubulin oligomer within the low resolution *ab initio* shape

resulted in a linear combination of three αβ-dimers similar to that seen in the tubulin protofilament (PDB-code 1TUB) [236, 239]. The oligomer is not fully straight, with the terminal dimer slightly bent relative to the axis of the preceding linear tetramer (Fig. 2.1 A, lower panel), in a conformation reminiscent of that found in the crystal structure of tubulin in complex with the stathmin-like domain of RB3 and colchicine (PDB-code 1SA0) [237]. The SAXS curve computed from our hexameric model yielded a good fit to the experimental data with χ = 1.09.

AT3Q24 consists of the Josephin domain (JD; about 20 kDa: NMR structure PDB-code 1YZB) and a 20 kDa unstructured region [75]. Fig. 2.1 B, upper panel shows the experimental SAXS curve for the AT3Q24. The estimated molecular weight of the solute (MW_{exp} = 260 ± 20 kDa) suggests that the AT3 oligomer should have 6-7 monomers under the assayed experimental conditions. Accordingly, the excluded volume of the particle in solution is V_p = 425 ± 20 nm^3. The experimental R_g = 6.9 ± 0.3 nm and maximum size D_{max} = 25 ± 1 nm point to an elongated particle structure. The low resolution shape of AT3Q24, reconstructed *ab initio* using DAMMIN [233], has the overall size of about 50 x 60 x 240 Å^3, fitting the experimental data with discrepancy χ = 1.07 (Fig. 2.1 B, upper panel). Overall, the AT3Q24 oligomer *ab initio* model is similar in size to that of tubulin, but it has a more bent shape (Fig. 2.1 B, lower panel). A high resolution model of AT3 oligomer cannot be built in the *ab initio* low resolution envelope, considering that the JD (PDB-code 1YZB) is only half of the total scattering mass of the protein.

The SAXS parameters calculated from measurement on the AT3Q24-tubulin complex are MW_{exp} = 500 ± 30 kDa, V_p = 900 ± 30 nm^3, R_g = 8.4 ± 0.4 nm and maximum size D_{max} = 30 ± 2 nm, distinctly different from those of the

isolated species. The low resolution shape of the AT3Q24-tubulin complex, reconstructed *ab initio* using DAMMIN [233], has the overall size of about 60 x 80 x 280 $Å^3$, fitting the experimental data with discrepancy χ = 1.11 (Fig. 2.1 C, upper panel). A high resolution model of the complex was attempted based on the following considerations: (1) the *ab initio* model shows that the complex is more elongated than the single components (tubulin and AT3Q24), and (2) the radius of the section of the complex is much larger than the radius of the section of the single components, but it is smaller than their summation. Therefore, the scaffold of the complex was modeled by the linear addition of tubulin $\alpha\beta$ dimers with the JD intercalating laterally between tubulin monomers, so as to minimize the increased radius of the section (Fig. 2.1 C, bottom panel). This is in agreement with the expectation that the AT3Q24 oligomer interacts with the tubulin oligomer in a "parallel" fashion, since under physiological conditions the AT3Q24 protein should face and bind the external part of the microtubule. Accordingly, in our model the JD units contact the tubulin surface at the region that would be external to the tubulin protofilament. Given that this model misses the unstructured part of AT3Q24 and the relative position of tubulin and the JD is not uniquely defined, the computed curve displays some deviations from the experiment at higher angles leading the discrepancy value of χ = 1.65 (Fig. 2.1 C, upper panel). Still, the fit at low angles is rather good indicating that the tentative model correctly represents the overall structure of the AT3Q24-tubulin complex.

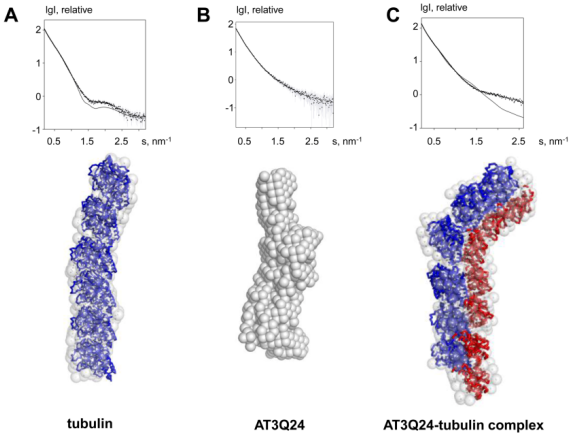

Fig. 2.1 SAXS results. (A) Upper panel: experimental scattering curve on tubulin (dots), and the scattering from the models: (dashed line) ab initio bead model obtained by DAMMIN and (continuous line) hexameric model based on the crystal structures (PDB-codes 1TUB and 1SA0). The plot displays the logarithm of the scattering intensity as a function of momentum transfer $s = 4\pi \sin(\theta)/\lambda$, where θ is the scattering angle and $\lambda = 0.15$ nm is the X-ray wavelength. Lower panel: model of hexameric tubulin. Gray beads show the ab initio model obtained by DAMMIN. The gray envelope is superimposed to the hexameric tubulin assembly, based on the crystal models (blue), drawn as Cα trace. (B) Upper panel: experimental scattering curve on AT3Q24 (dots), and the scattering from ab initio bead model (dashed line). Lower panel: ab initio low resolution shape model (gray beads) obtained by DAMMIN. (C) Upper panel: experimental scattering curve on the AT3Q24-tubulin complex (dots), the scattering from ab initio bead model (dashed line), and from the model based on the crystal structure of the components (continuous line). Lower panel: model of the AT3Q24-tubulin complex. The gray ab initio bead model, obtained by DAMMIN, is superimposed to the AT3Q24-tubulin complex based on the crystal structure of tubulin (blue: PDB-code 1TUB and 1SA0) and on the NMR structure of the Josephin domain of AT3 (red: PDB-code 1YZB), both drawn as Cα traces

Optimal tubulin binding of AT3Q24 involves co-presence and appropriate spacing of three separate amino acid stretches

Following the SAXS analysis, we performed SPR experiments to achieve a more precise identification of the AT3 regions involved in tubulin dimer binding. We studied real time association and dissociation using a sensor chip coupled directly to tubulin dimer and assaying different truncated forms of human AT3Q24 (N-terminal His-tagged proteins) (Fig. 2.2). The binding and release of each variant to and from the chip was monitored. To determine the K_D values, we used a Langmuir 1:1 model fitting of simultaneous sensorgrams at different concentrations with BIA evaluation software.

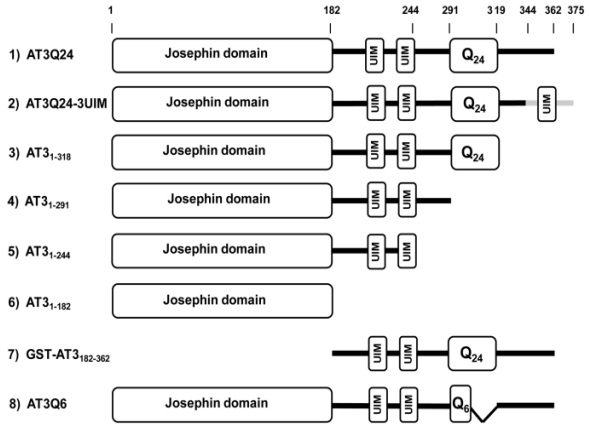

αβ-TUBULIN		
k_{on} ($M^{-1}s^{-1}$)	k_{off} (s^{-1})	K_D (M)
$1.7 \cdot 10^4$	$9.2 \cdot 10^{-4}$	**$5.2 \cdot 10^{-8}$**
$6.2 \cdot 10^2$	$1.7 \cdot 10^{-3}$	**$2.7 \cdot 10^{-6}$**
b.d.	b.d.	**b.d.**
$6.9 \cdot 10^2$	$7.2 \cdot 10^{-4}$	**$1.0 \cdot 10^{-6}$**
b.d.	b.d.	**b.d.**
b.d.	b.d.	**b.d.**
b.d.	b.d.	**b.d.**
$2.6 \cdot 10^2$	$1.4 \cdot 10^{-3}$	**$5.4 \cdot 10^{-6}$**

Fig. 2.2 Sequence and domain organization of the investigated AT3 variants, and the respective kinetic and equilibrium binding constants to tubulin dimer. Real time association and dissociation was assayed by SPR using a sensor chip CM5 coupled directly to the indicated proteins (His-tagged at the N terminus, unless otherwise stated). The C-terminal AT3 domain was assayed in fusion with GST (GST-AT3$_{182-362}$). GST and GST-AT3Q24 were used as negative and positive controls, respectively. No detectable binding was observed for GST, whereas k_{on} and k_{off} values measured for GST-AT3Q24 were not significantly different from those of AT3Q24 (k_{on}: $5.4 \cdot 10^3$; k_{off}: $1.5 \cdot 10^{-3}$; K_D: $2.8 \cdot 10^{-7}$). UIM: ubiquitin-binding motif; b.d.: below detection; n.a.: not assayed.

Only for the variants AT3Q24, AT3Q24-3UIM, $AT3_{1-291}$ and AT3Q6 (constructs 1, 2, 4 and 8) measurable values could be recorded, all other forms displaying binding below the detection limit (Figs. 2.2, 2.3, 2.4).

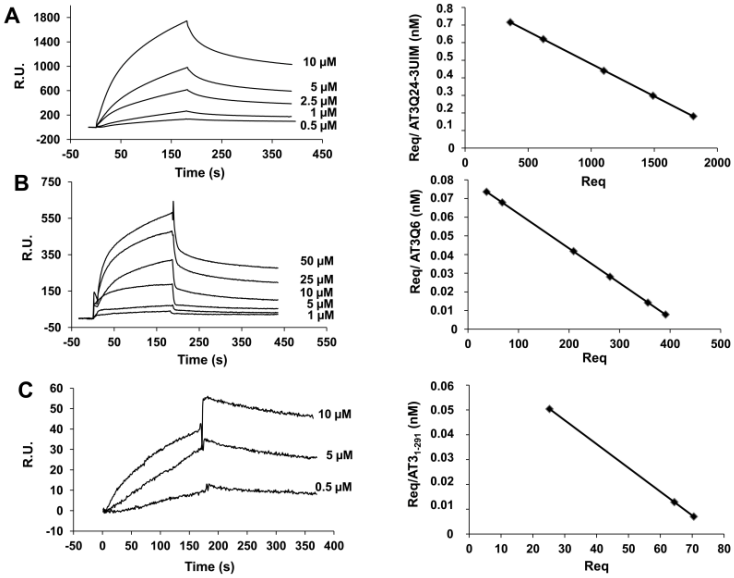

Fig. 2.3 Association/dissociation kinetics for the binding between tubulin dimer and AT3Q24-3UIM, AT3Q6, $AT3_{1-291}$ variants. Tubulin dimer was immobilized on the sensor chip and the indicated concentrations of (A) AT3Q24-3UIM, (B) AT3Q6, (C) $AT3_{1-291}$ were flowed onto the chip surface. The Req values obtained for each given protein concentration were used to generate the Scatchard plots.

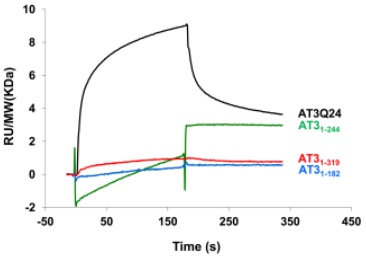

Fig. 2.4 Association/dissociation kinetics for the binding between tubulin dimer and AT3Q24, $AT3_{1-182}$, $AT3_{1-244}$, $AT3_{1-319}$. Comparison of the profiles obtained at equal concentration (5 μM) of AT3Q24 (black), $AT3_{1-182}$ (cyan), $AT3_{1-244}$ (green), $AT3_{1-319}$ (red).

In particular, we could assign to the wild-type AT3Q24 splice variant (construct 1) an affinity as low as 50 nM, in keeping with our previous report [121]. The truncated $AT3_{1-291}$ form (construct 4) was capable of binding tubulin, although with an about 20-fold lower affinity with respect to the AT3Q24 wild type variant. Surprisingly, the longer construct 3, in which the polyQ stretch is still present, lost any detectable binding, suggesting that the polyQ region may interfere with tubulin binding in the absence of region 319-362. These data suggest that a tubulin binding region (TBR) is present downstream of the polyQ. We will refer to this site as TBR3. The presence of a binding region downstream of the polyQ was further supported by comparing the affinities of the two splicing isoforms mainly expressed in the central nervous system [70, 83], i.e., AT3Q24 (construct 1) and AT3Q24-3UIM (construct 2), which only differ in the C-terminal region (Figs. 2.2, 2.3, 2.5). For the isoform AT3Q24-3UIM, a 2.7 μM K_D was determined, close to that of the truncated $AT3_{1-291}$ mutant, suggesting that TBR3 is either absent or functionally inactivated in this splice variant. Also noteworthy is that the AT3Q6 form (construct 8) displayed

an affinity well below that of AT3Q24, suggesting that a polyQ length above a given threshold is required for the correct positioning of TBR3.

```
     319                    344              362         375
      |                      |                |           |
2UIM  RDLSGQSSHPCERPATSSGALGSDLGKACSP-FIMFATFTLYLT------------
3UIM  RDLSGQSSHPCERPATSSGALGSDLGDAMSEEDMLQAAVTMSLETVRNDLKTEGKK
      *************************.* *   :: *:.*: *
```

Fig. 2.5 Alignment of the C-terminal amino acid sequences downstream of the polyQ of the two AT3 isoforms (AT3Q24 and AT3Q24-3UIM). In bold is the UIM sequence. The alignment was performed by Clustal Omega.

Further deletion of the disordered region (construct 5) resulted in undetectable binding in the BIAcore assay, suggesting that one binding region upstream of the polyQ is located in the stretch 244-291. We refer to this region as TBR2. Although JD did not show any binding to tubulin in our SPR assay, it should be stressed that our previous pull-down experiments also demonstrated that the JD in isolation was capable of binding tubulin [121]. We therefore assume that its affinity for tubulin is below the sensitivity of the BIAcore X instrument. The essential role of JD in tubulin binding was also confirmed by the lack of any detectable tubulin binding of the C-terminal disordered domain in isolation (construct 6, GST-AT3$_{182-362}$).

On the whole, these results support the idea that AT3 interacts with tubulin dimer *via* three regions, one located in the JD and the two others in the C-terminal disordered domain, namely in the stretches 244-291 and 319-362, respectively.

AT3 directly binds HDAC6

A previous report has shown that in the transport machinery of misfolded proteins to the aggresome *via* microtubules, HDAC6 recognizes protein aggregates by binding to polyubiquitylated proteins at the diglycine motifs of the unanchored ubiquitin C-termini generated by AT3 [122]. However, to date it is unclear whether HDAC6 interacts directly with AT3. We therefore performed further SPR experiments, using a sensor chip coupled to HDAC6, to assess the binding and release of the AT3 variants under investigation. Actual sensorgrams are reported in Fig. 2.6 and summarized in Fig. 2.7.

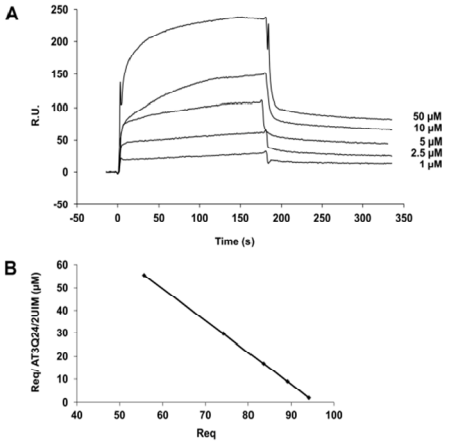

k_{on} ($M^{-1}s^{-1}$)	k_{off} (s^{-1})	K_D (M)
$8.7 \cdot 10^2$	$6.3 \cdot 10^{-4}$	$7.2 \cdot 10^{-7}$

Fig. 2.6 Association/dissociation kinetics for the binding between HDAC6 and AT3Q24. (A) HDAC6 was immobilized on the sensor chip and the indicated concentrations of AT3Q24 were flowed onto the chip surface. (B) The Req values obtained for each given protein concentration were used to generate the Scatchard plot. In the inset the kinetic and equilibrium binding constants are given.

Direct binding of AT3 to HDAC6 was substantiated by significant affinity values, in the range 10^{-7}-10^{-8} M (Fig. 2.7). The two AT3Q24 and AT3Q24-3UIM isoforms displayed quite similar affinities (Fig. 2.7 and 2.8). However, no significant binding by any of the truncated variants was detected (Fig. 2.8). The 5-fold difference between the two isoforms suggests that the HDAC6-binding site includes the C-terminal region of AT3 downstream of the polyQ region.

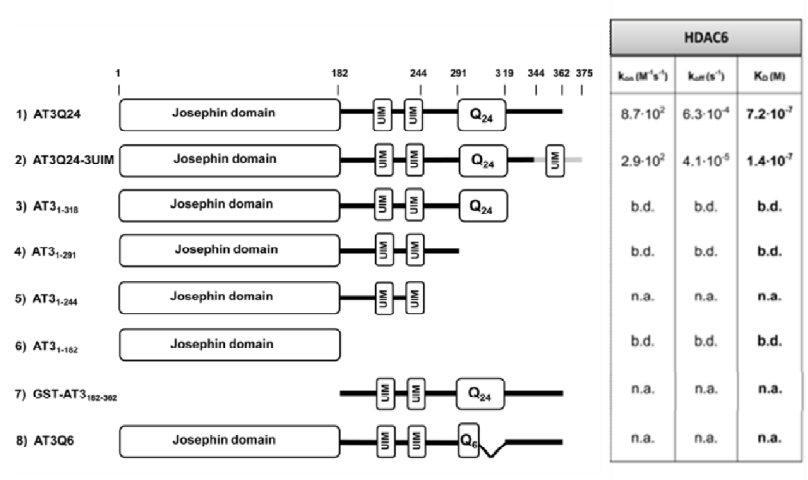

Fig. 2.7 Sequence and domain organization of the investigated AT3 variants, and the respective kinetic and equilibrium binding constants to HDAC6. Real time association and dissociation was assayed by SPR using a sensor chip CM5 coupled directly to the indicated proteins (His-tagged at the N terminus, unless otherwise stated). The C-terminal AT3 domain was assayed in fusion with GST (GST-AT3$_{182-362}$). GST and GST-AT3Q24 were used as negative and positive controls, respectively. UIM: ubiquitin-binding motif; b.d.: below detection; n.a.: not assayed.

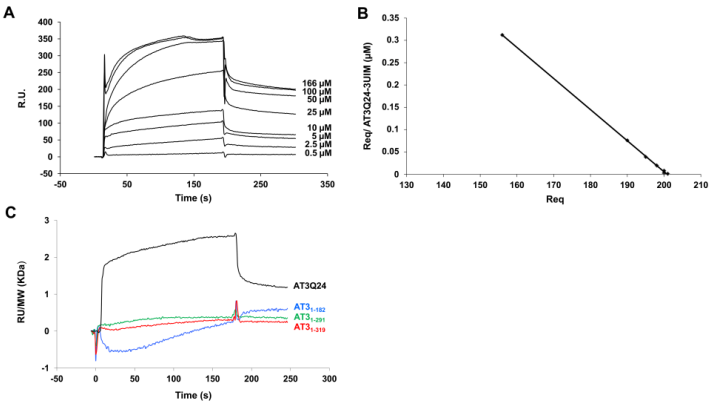

Fig. 2.8 Association/dissociation kinetics for the binding between HDAC6 and AT3Q24-3UIM and truncated AT3 variants. (A) HDAC6 was immobilized on the sensor chip and AT3Q24-3UIM at the indicated concentrations flowed onto the chip surface. (B) The Req value obtained for each protein concentration for the HDAC6 binding sensor chip was used to generate the Scatchard plot. (C) Comparison of the profiles obtained at equal concentration (5 µM) of AT3Q24 (black), $AT3_{1-182}$ (cyan), $AT3_{1-291}$ (green), $AT3_{1-319}$ (red).

2.4 DISCUSSION

Aggresomes are proteinaceous inclusion bodies that accumulate around the microtubule-organizing center in eukaryotic cells, when cellular degradation machinery is impaired or overwhelmed, leading to an accumulation of protein for disposal [240]. Their formation is regarded as a protective response, sequestering potentially cytotoxic aggregates and also acting as a staging center for eventual autophagic clearance from the cell [47, 224, 241].

Several molecular players are involved in sorting misfolded proteins to aggresomes *via* microtubules. In particular, polyubiquitin-tagged proteins are gathered by HDAC6, which also binds the component dynactin/p150^{Glued} of dynein, the microtubule-based motor protein [122, 224]. Furthermore, previous work has suggested that the ZnF-UBP domain of HDAC6 binds protein aggregates by interacting with polyubiquitin moieties exclusively at the level of their unanchored C-termini. In addition, AT3 has been implicated as one of the deubiquitinases responsible for exposing such termini on the aggregates, so quite likely it plays a major role in their sorting to the aggresome [122]. A previous report [117] also added to the understanding of AT3's physiological role by showing that its depletion causes a significant disorganization of the cytoskeleton, including microtubules, microfilaments and intermediate filaments, in line with our previous finding that AT3 is capable of tightly binding to tubulin [121]. Finally, HDAC6 is also likely to be associated, at least reversibly, with microtubules, given its well-known tubulin deacetylase activity [242].

These data clearly indicate that the transport machinery of aggregated proteins to aggresomes is a quite complex one, wherein HDAC6

acts as the hub protein, interacting with at least dynein, microtubules and polyubiquitin. Thus, the present investigation was mainly aimed at providing a better understanding of AT3's role in such machinery.

We first characterized the AT3-tubulin dimer complex by SAXS, which actually confirmed the capability of the two protein species to tightly interact with each other. In particular, based on the assumption that under physiological conditions AT3Q24 should face and bind the external part of the microtubule, the data highlight an interaction in which the AT3Q24 oligomer binds to the tubulin oligomer in a "parallel" fashion with the JD units intercalating laterally between tubulin monomers (Fig. 2.1C, bottom panel).

Consistently with SAXS data, SPR data show that tubulin and AT3 interact according to a Langmuir 1:1 model. Interaction of AT3Q24 with tubulin takes place through a single binding interface, since the secondary plot of ln[d(RU)/d(time)] against time shows a curve with a constant slope, indicative of a single binding site. Nevertheless, analysis of SPR data indicates that this interaction surface is tripartite, being originated by three discontinuous individual TBRs. Immunoprecipitation experiments reported elsewhere show that the isolated JD domain may bind tubulin under different experimental conditions [121], although no binding is detectable by our SPR assay (construct 6). We refer to this tubulin interaction region as TBR1. TBR1 deletion (construct 7) completely abolishes binding in our SPR assay. The bipartite interaction surface formed by TBR1 and TBR2 - that is located between JD and polyQ - has at least 100-fold less affinity for tubulin, compared to the tripartite surface found in AT3Q24 (compare constructs 1 and 4). When comparing constructs 4 and 8 with the wild type (construct 1), it is apparent that a third TBR (referred to as TBR3) is located downstream of the polyQ region. Notably, the polyQ stretch plays a modulatory role on AT3-tubulin interaction in a way

dependent on the type of tubulin-interacting surface present. Actually, comparison of constructs 1 and 8 indicates that an extended polyQ stretch (Q24) actually promotes AT3-tubulin interaction when the full tripartite structure can be formed. By contrast, in the absence of TBD3, Q24 inhibits binding ability of the bipartite interface formed by TBD1 and TBD2 (constructs 3 and 4).

Although K_Ds of the various isoforms and mutants analyzed in this paper differ by more than two orders of magnitude, their k_{off} are remarkably similar - differing at most by a factor of 2 - indicating that the tripartite structure plays a major role in establishing the interaction, and a much less important role in maintaining it. In the absence of TBR3 - and the more so in the absence of both TBR2 and TBR3 - TBR1 has trouble in establishing a productive contact with tubulin. Once contact has been established, dissociation of the tubulin-AT3 complex is mostly governed by TBR1 that remains locked in place with similar efficacy, regardless of the number of TBRs domains flanking it.

As mentioned above, an AT3 carrying a shorter polyQ (AT3Q6, construct 8) displays an affinity well below that of AT3Q24, suggesting that a polyQ length above a given threshold is required for the correct positioning of TBR3. In line with our observations, a recent paper highlights the crucial role of polyQ length in huntingtin function, as both its expansion and its deletion prevents the upstream and downstream regions from interacting with each other [243].

Interestingly, AT3Q24-3UIM - construct 2 - displays an about 50-fold lower affinity for tubulin than AT3Q24. This suggests that the two isoforms may play different physiological roles, the former likely being the one preferentially involved in the interaction with microtubules.

All together these data indicate that formation of the binding interface to tubulin is governed by a complex intra-molecular, inter-domain regulatory network similar to the one found in the much larger human Sos protein [244].

Besides a more in-depth characterization of the mode of AT3-tubulin interaction, one major finding of the present paper is the first evidence we provide of a direct interaction of AT3 with HDAC6. Our data also suggest that HDAC6 binds to the C-terminal stretch of AT3 downstream of the polyQ, as supported by the fact that its removal resulted in loss of measurable affinity between the two proteins. Given the comparable affinities of the AT3Q24 and AT3Q24-3UIM isoforms for HDAC6, we suggest that the binding site is located in the stretch 319-344, as it retains an identical sequence in the two variants (Fig. 2.5).

Although much is still to be elucidated regarding the mechanisms by which the individual components of the transport machinery participate in protein sorting to the aggresome, our results pave the way to further studies that should aid in better understanding their roles and mechanisms. This will be accomplished, in particular, by developing AT3 mutants impaired in their ability to bind either HDAC6 or tubulin, and analyzing the impact of these mutations on the intracellular distribution of such proteins, as well as on aggresome formation.

Chapter Three

Ataxin-3 toxicity assessed in a yeast cellular model

3.1 AIM OF THE WORK

Polyglutamine diseases are a group of disorders in which the polyQ-expansion over a certain threshold leads to misfolding of the polyQ-expanded protein, its aggregation into large intracellular inclusions, cytotoxicity and eventually dysfunction and demise of specific neurons [245]. A member of this family is the spinocerebellar ataxia type 3 (SCA3), caused by the expansion of the polyQ tract in the protein ataxin-3 (AT3). To date, the mechanism by which polyQ-expanded AT3 leads to SCA3 pathogenesis has not been fully clarified. It has been largely reported that the polyQ-expansion induces misfolding and consequent transition to aggregation-prone conformations [124, 125, 130]. As for most amyloid-forming proteins, several pathways may drive the conversion of the soluble protein into large amyloid aggregates, though small aggregates and oligomers are the species responsible for cytotoxicity [9, 131, 246, 247]. It is suggested that soluble amyloid oligomers have common mechanisms of toxicity [248], for example being able to destabilize the cellular membrane or to sequester quality control system components and transcription factors, causing proteotoxic stress and transcriptional dysregulation [249]. Consequently, this investigation is aimed at clarifying the mechanisms underlying AT3 aggregation and how the different species could exert their cytotoxicity. To elucidate this, we used as a model organism the budding yeast *Saccharomyces cerevisiae*, one of the simplest eukaryotes, that shares many cellular mechanisms with all eukaryotic cells including humans. It has long been used as model organism for studying neurodegeneration [143]: most processes involved in neurodegenerative disorders such as apoptosis and necrosis, mitochondrial damage, oxidative stress, protein aggregation and degradation can be analyzed within yeast [185]. Models of protein aggregation

disorders in *S. cerevisiae* have provided new insights into Parkinson's disease [250], amyotrophic lateral sclerosis [162], and Huntington's disease [175, 177]. Importantly, these yeast models recapitulate cellular aspects of the misfolded protein and their corresponding diseases. Here, we intend to characterize the mechanisms of toxicity exerted by AT3 variants expressed in *S. cerevisiae*. First, we have checked whether the expression of an expanded-pathological form can develop a growth-inhibitory effect or reduce viability compared to the wild type strain. Then, we have evaluated possible relationships between toxicity and accumulation of reactive oxygen species (ROS) and whether antioxidant mechanisms, such as glutathione balance or antioxidant enzymes activities, are affected. We have also assessed whether polyQ deletion impacts on the toxic effects under investigation, so as to better understand the role of the regions outside the polyQ tract in the development of toxicity.

3.2 EXPERIMENTAL PROCEDURES

Yeast strains and plasmids

Experiments were carried out in W303 *(MATα can1-100 ade2-1 his3-11, 15 trp1-1 ura3-1 leu23,112)* yeast strain. p426GALhtt103QGFP plasmid (Addgene) was digested with *BamHI* restriction enzyme to excide htt gene. AT3Q26, AT3Q85 and AT3291Δ genes were digested with *BamHI* and the resulting fragments were sub cloned into digested plasmid in frame with GFP protein at C-terminal. Transformation of yeast was performed by the lithium acetate method [251]. We used yeast cells transformed with the p426GAL empty vector as a control.

Yeast growth conditions

Cells were grown overnight in selective media containing glucose (2%), washed three times in sterile water and diluted to an OD_{600} of 0.1 in selective media containing 2% galactose as inductor of AT3 expression. The analyses were performed after 16, 24 or 48 h of induction, unless otherwise noted.

Confocal microscopy analysis of protein aggregation

Fluorescence microscopy to detect protein aggregation was performed using Leica Mod. TCS-SP2 confocal microscope (Leica Microsystem, Wetzlar, Germany) and the fluorescence of GFP was excited with 488 nm line.

Clonogenic growth assays

About 100 cells derived from the overnight cultures washed in water were spread on a plate with selective medium containing glucose as sole

carbon source and on another plate with selective medium containing galactose as sole carbon source. The ability to form colony is plotted as the ratio of the number of cells grown on galactose to those grown on glucose expressed as percentage.

Filter trap assay and dot blot analysis

1 ml of culture was harvested after 24 h of induction for each strain. Total protein extracts were obtained as previously described [252]. Briefly, the cells were resuspended in 250 µl spheroplasting solution (1.2M sorbitol, 100 mM EDTA, 20 mM Tris pH 7.5, 50 mM 2-mercaptoethanol, 100 U/ml lyticase) and incubated for 1 h at 30° C. The spheroplasted cells are collected by centrifugation at 800 rcf for 5 min and the supernatant is removed completely. The pelleted spheroplasts are then resuspended in 60 µl lysis buffer (20 mM Tris, pH 7.5, 10 mM 2-mercaptoethanol, 0.5% Triton X-100, protease inhibitor cocktail), vortexed at high speed for 1 min and then incubated for an additional 10 min at room temperature. The cellular debris was sedimented by centrifugation at 4000 rcf for 2 min. The concentrations of different samples were determined by Bradford assays. Same amounts of protein were subjected to a filter trap assay and dot blot analysis [135]. Dot blotting was performed by applying samples to a nitrocellulose membrane mounted on a manifold. Samples were vacuum-filtered and washed with 200 µl of PBS. For the filter trap assay, yeast extracts were mixed with 500 µl of SDS buffer (50 mM Tris-HCl, pH 8.0, 5% SDS, 10 mM DTT, 100 mM NaCl, 1 mM EDTA). After a 10 min incubation at 100 °C, the resulting samples were applied to a cellulose acetate membrane (0.2 µm pore size) mounted on a manifold, vacuum-filtered, washed once with 100 µl of SDS buffer and finally with 200 µl of PBS buffer.

The membranes were processed by immunodetection using anti-human AT3Q26 Z46 polyclonal antibody [253].

MTT assay

MTT assay was performed as described by Teparić [254] with minor modifications. Cells from 1 ml of culture were harvested and resuspended in 0.4 ml 5 µg/mL MTT [3-(4,5-dimethylthiazoyl-2-yl) 2,5-diphenyltetrazolium bromide]. The mixture was incubated at room temperature with shaking for 2 h. After that cells were harvested and resuspended in 1 ml acid 2-propanol (0.04 M HCl in 2-propanol). The suspension was agitated for 10 minutes and then centrifuged at 8000 rpm. for 10 min. The absorbance of the supernatant was measured at OD_{540}. The data were expressed as percentage of viability respect to the control (100% viability).

ROS assay

ROS levels were monitored using the Red Hydrogen Peroxide Assay Kit (Enzo Life Sciences) according to the manufacturer's protocol. Cells from 3 ml of culture were harvested and resuspended in lysis buffer (20 mM phosphate buffer, 5 mM EDTA, 0.2 mM PMSF pH 7.2). Cells were broken using glass beads and by vortexing five times for 1 min after intervals of 1 min in ice. Cell debris was pelleted and the supernatants were used for the test. The conversion of red peroxidase substrate in resorufin was determined measuring the absorbance at 576 nm. The data were expressed as fold increase respect the empty vector strain level.

Determination of glutathione levels

Reduced and total glutathione content was determined by the method of Boyne and Ellman [255], using 5,5'-dithio-bis(2-nitrobenzoic acid) (DTNB). Cells from 10 ml were harvested, washed twice with PBS to remove any traces of growth medium, and resuspended in ice-cold 5% perchloric acid. Cells were broken with glass beads as described above and incubated on ice for 15 min to precipitate proteins. Cell debris and proteins were pelleted at 13.000 rpm for 15 min at 4 °C and the supernatant was neutralized with 100 mM NaH_2PO_4 and 5 mM EDTA pH 7.5. For GSH levels, 600 µM of Ellman reagent was added to samples and the absorbance at 412 nm was measured in a spectrophotometer. For total glutathione, the neutralized supernatants were incubated at 37 °C for 10 min in presence of 1 U/ml of glutathione reductase and 0.2 mM NADPH and then GSH content was determined. The GSH concentration was determined using a GSH standard curve. The data were expressed as the ratio of GSH to total glutathione content in percentage.

Antioxidant enzyme activity determination

The catalase (CAT) activity was determined as described by Shangari [256] by determining the rate of H_2O_2 decomposition with the ferrous oxidation. Cells from 3 ml were harvested and resuspended in hypotonic lysis buffer (10 mM HEPES, 1.5 mM $MgCl_2$, 10 mM KCl, 0.5 mM DTT, 0.2 mM PMSF pH 7.9) and broken as described above. The data were expressed as fold increase respect the empty vector strain level.

The superoxide dismutase (SOD) activity was measured using the protocol of enzymatic assay described by Sigma. Cells from 3 ml of culture were harvested and resuspended in lysis buffer (20 mM phosphate buffer, 5

mM EDTA, 0.2 mM PMSF pH 7.2) and broken as described above. The data were expressed as fold increase respect the empty vector strain level.

Propidium iodide staining

500 µl of cells after 48 h of induction were harvested and resuspended in 250 µl of PBS, incubated for 30 min in the dark with 10 µg/ml of propidium iodide (PI). Then cells were applied to a microscopic slide and observed using. Leica Mod. TCS-SP2 confocal microscope (Leica Microsystem, Wetzlar, Germany). The fluorescence of PI was excited with 488 nm line. As positive control, cells were treated for 15 min with 70% ethanol prior to incubation with PI.

Statistical analysis

All experiments were done at least in triplicate. Data are presented as means ± standard error of fold increase or percentage. Values were compared by Student t test. $P < 0.05$ was considered significant.

3.3 RESULTS

A yeast model of AT3 toxicity

To provide insights into SCA3 mechanisms of cellular toxicity in a eukaryotic system, we expressed three AT3 variants in *S. cerevisiae*. Specifically, we expressed a wild type and a pathogenic AT3 variant carrying 26 (AT3Q26) and 85 (AT3Q85) consecutive glutamines, respectively, and a variant truncated immediately upstream of the polyQ (AT3291Δ). All constructs were in fusion with GFP at the C-terminus, under GAL1 promoter control and induced by galactose (Fig. 3.1).

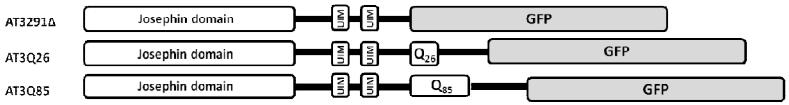

Fig. 3.1 Sequence and domain organization of the investigated AT3 variants.

We assessed the expression levels of the AT3 variants at 16, 24 and 48 h of induction. Dot blot analysis of whole cell lysates did not show any significant difference in expression among the three variants at fixed times of induction. SDS-PAGE analysis at 24 h of induction confirmed the presence of the three variants and their expression levels (Fig. 3.2).

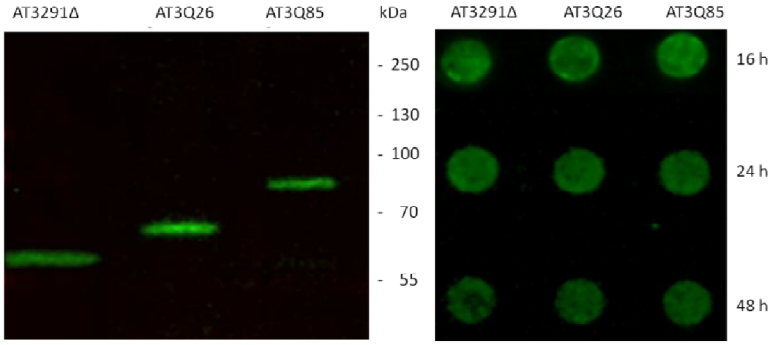

Fig. 3.2. Dot blot and SDS-western blot analysis of AT3 expression levels. Whole protein extracts of *S. cerevisiae* strains expressing the AT3 variants at different times after induction were subjected to dot blot (right panel) and immunodetected using anti-AT3 antibody. Whole protein extracts of *S. cerevisiae* strains expressing the AT3 variants at 24 h after induction were subjected to SDS-PAGE and western blotted using anti-AT3 antibody (left panel).

Morphological analysis of AT3 aggregates

It has been reported that polyQ-expansions in the ataxin-3 lead to the formation of intracellular SDS-insoluble aggregates [134]. To check whether this also occurs in our model yeast, we exploited protein constructs in fusion with GFP to monitor their distribution in cells by confocal microscopy analysis (Fig. 3.3). The results show that the expression of the wild type and of the truncated forms leads to diffuse cytoplasmic distribution at all the time of the induction. In contrast, the expanded variant forms intracellular inclusions starting from 16 h of induction.

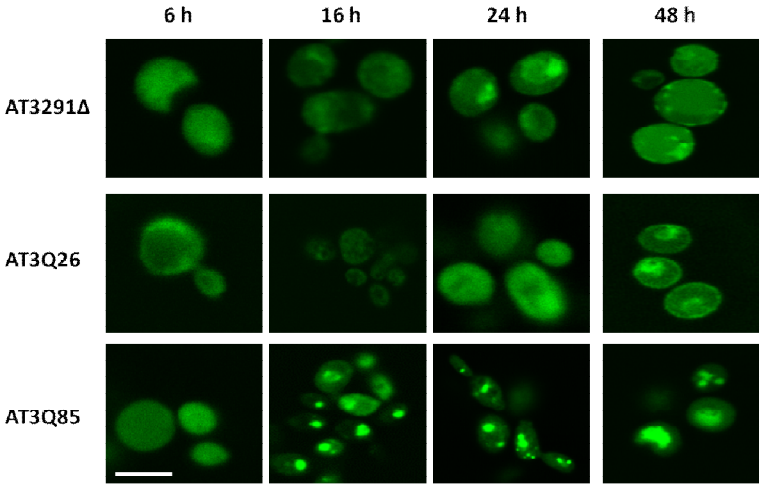

Fig. 3.3 Fluorescence microscopy analysis of AT3 aggregation. Cells expressing the indicated AT3-GFP fusion proteins were analyzed by fluorescence microscopy (Scale bar: 10 µm) at the indicated times of induction.

Subsequently, a filter trap analysis on the whole protein extracts of the three strains at 24 h of induction confirmed that the sole AT3Q85 was capable to form SDS-insoluble aggregates (Fig. 3.4).

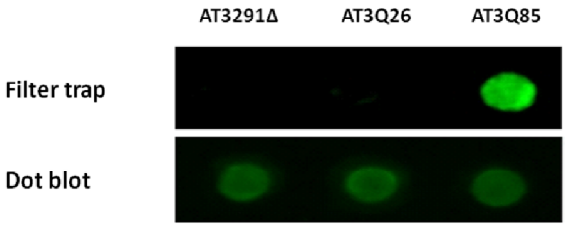

Fig. 3.4 Filter trap assay analysis of AT3 aggregation. Whole protein extracts of the three strains after 24 h of induction were subjected to filter trap analysis to detect SDS-insoluble aggregates. The immunodecoration was performed using anti-AT3 antibody. Dot-blotted analysis was performed as a loading control.

AT3291Δ and AT3Q85 expression impaired the cell growth

The effect of the expression of the AT3 variants on yeast survival rate was analyzed by a clonogenic assay. Briefly, cells were pre-grown in a medium that repressed expression of AT3 variants. Then, a fixed amount of cells was plated in parallel onto two different media: without and with inducer (with glucose and galactose, respectively) and incubated at 30 °C. Their ability to form a colony was determined under either condition (Fig. 3.5). This revealed a significant growth-inhibitory effect of AT3-Q85 expression. The AT3291Δ expressing strain also revealed a decrease in growth capability although statistically non-significant.

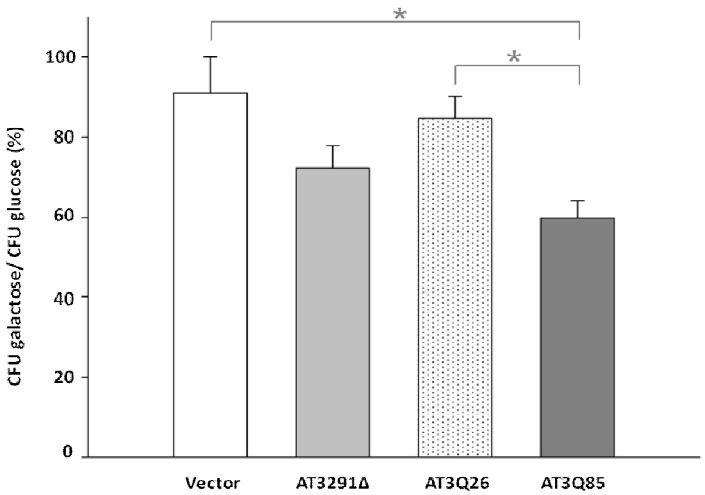

Fig. 3.5 Effect of the AT3 variants expression on cell growth. About 100 cells from the different cultures were spread onto glucose or galactose plates and their colony-forming ability was expressed as percentage ratio of cells grown under inducing (galactose) *versus* non-inducing (glucose) conditions. Bars represent standard errors and are derived from at least three independent experiments ($P < 0.05$, t-Student test)

A significant reduction in cell viability of yeast strains expressing pathological and truncated AT3 forms was also determined by the MTT assay (Fig. 3.6).

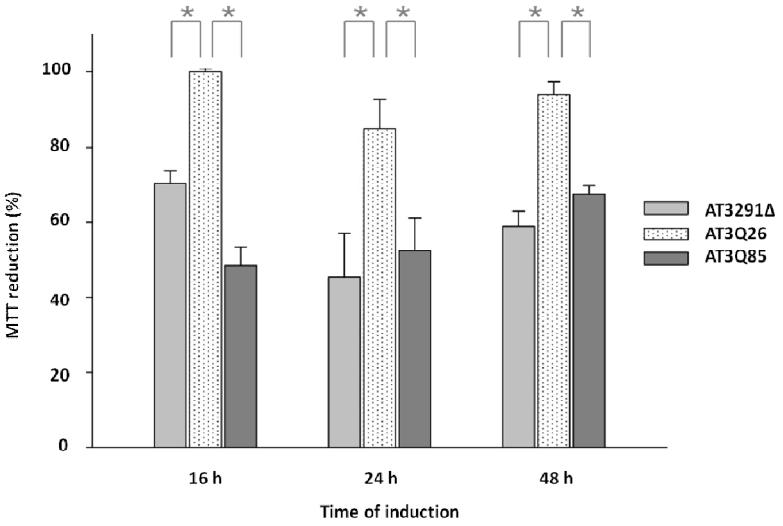

Fig. 3.6 Effect of AT3 variants expression on cell viability. MTT assay was performed on cultures after the indicated induction times. Data are expressed as percentage ratio of MTT reduction *versus* the control (empty vector). Bars represent standard errors and are derived from at least three independent experiments ($P < 0.05$, t-Student test).

Oxidative stress is induced by AT3291Δ and AT3Q85 expression

Besides quantifying cell viability, the MTT assay, can be considered an indicator of mitochondrial stress. To determine whether the growth inhibitory effect observed in the presence of mutant AT3 may be ascribed to increased oxidative stress, we first evaluated ROS levels in the three strains. We found that already 16 h after induction, H_2O_2 levels were significant higher in yeast expressing AT3Q85 and AT3291Δ compared to AT3Q26 (1.9 and 1.4 fold increase, respectively). At 24 h, the increase was significant only for the expanded form (1.6 fold increase) and, at the latest time, the levels of the three strains were comparable (Fig. 3.7).

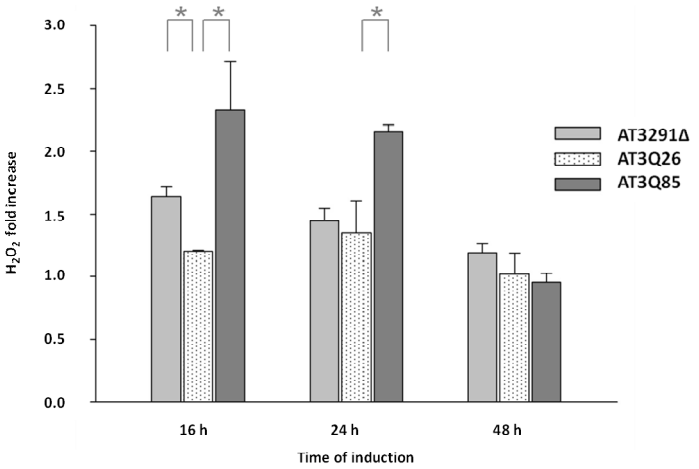

Fig. 3.7 ROS levels in cells expressing AT3 variants. Intracellular H_2O_2 levels were determined using the Red Hydrogen Peroxide Assay Kit. The conversion of red peroxidase substrate in resorufin was determined measuring the absorbance at 576 nm. The data were expressed as fold increase with respect to the empty vector strain level. Bars represent standard errors and are derived from at least three independent experiments ($P < 0.05$, t-Student test).

We then assessed glutathione redox state in the yeast strains at different induction times, by determining the ratio of reduced (GSH) to total

glutathione content. The results (Fig. 3.8) indicate that at 16 h from induction the ratio in the AT3Q85 strain underwent a small but statistically significant decrease (by about 1.2 fold), unlike the AT3291Δ strain that did not show any significant variation at all times assayed (Fig. 3.8).

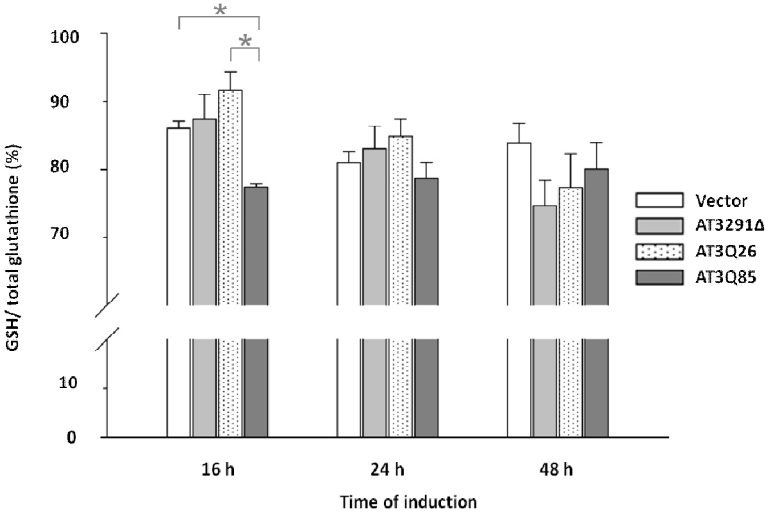

Fig. 3.8 Glutathione levels in cells expressing AT3 variants. GSH and total glutathione content were determinate using Ellman methods. The data were expressed as the ratio of GSH to total glutathione content in percentage. Bars represent standard errors and are derived from at least three independent experiments ($P < 0.05$, t-Student test).

The activity of antioxidant enzymes is increased in strains expressing AT3291Δ and AT3Q85

Enzymatic components in the antioxidant defense system play critical role(s) against oxidative stress. To determine whether the detected increase in ROS levels may induce changes on the activity of certain antioxidant enzymes, we measured catalase (CAT) and superoxide dismutase (SOD) activities. Our results reveal markedly increased activity of CAT at 16 h of induction in the yeast expressing AT3Q85 and AT3291Δ compared to AT3Q26 (1.5 and 1.7 fold, respectively). At 24 h, the increase was significant only for the expanded form (1.5 fold) and at 48 h there were no differences (Fig. 3.9).

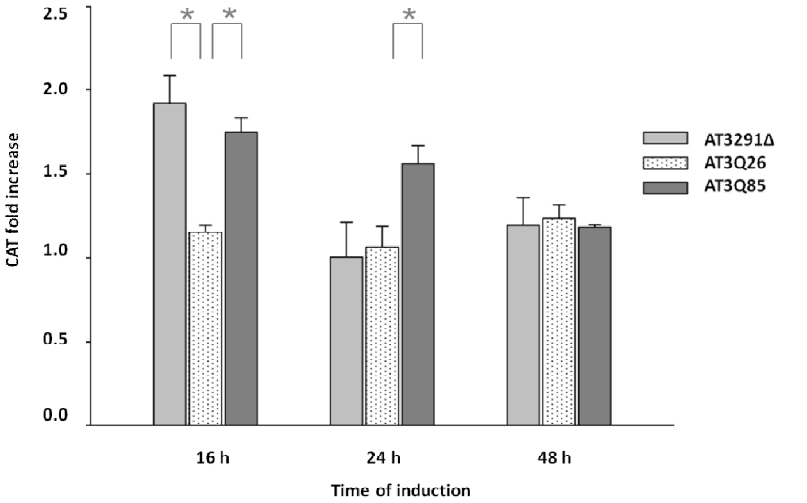

Fig. 3.9 Catalase activity determination. The rate of H2O2 decomposition was determined using the ferrous oxidation assay and absorbance was measured at 560 nm. Data are expressed as fold increase with respect to the empty vector strain level. Bars represent standard errors and are derived from at least three independent experiments ($P < 0.05$, t-Student test).

As regards SOD, we observed a significant activity increase in the AT3291Δ strain at 24 and 48 h of induction (1.4 and 1.3 fold, respectively), whereas in the case of AT3Q85 a significant increase (1.5 fold) was detected only at 48 h of incubation (Fig. 3.10).

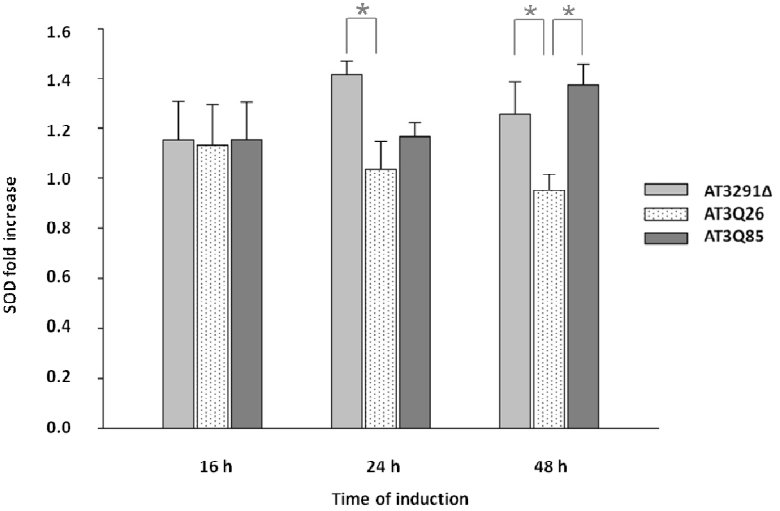

Fig. 3.10 Superoxide dismutase activity determination. Activity was determined as the rate of reduction of oxidized cytochrome c at 550 nm. Data are expressed as fold increase with respect to the empty vector strain level. Bars represent standard errors and are derived from at least three independent experiments ($P < 0.05$, t-Student test).

AT3Q85 expression affects membrane integrity

To assess whether the expression of the pathological AT3 variant causes membrane damage, we performed propidium iodide staining, which is based on the capability of the dye to bind to DNA with resulting fluorescence enhancement, but not to permeate intact cell membranes. We observed that ~ 10 % of AT3Q85 expressing cells took up the dye, indicating loss of plasma membrane integrity and cell necrosis. In contrast, the percentage of necrotic AT3Q26- and AT3291Δ-expressing cells were similar to control cells (Fig. 3.11).

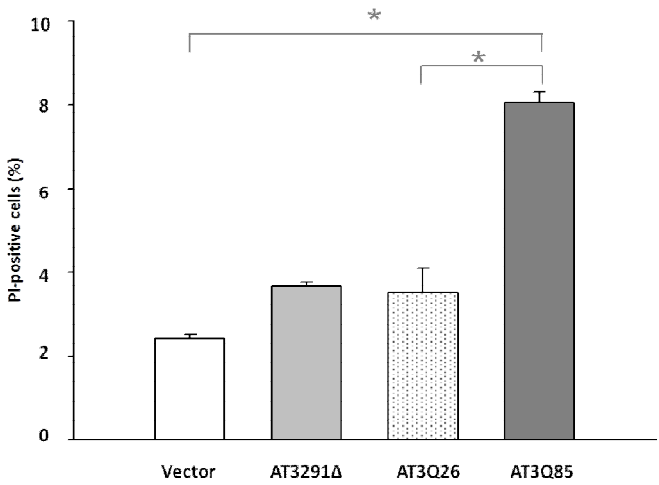

Fig. 3.11 Propidium iodide staining of AT3-expression strains. PI positive cells were counted from > 300 cells from different field views. Bars represent standard errors and are derived from at least three independent experiments ($P < 0.05$, t-Student test).

3.4 DISCUSSION

This work describes the use of a yeast model system to investigate the effects of pathogenic AT3 on yeast cells. We expressed three AT3 variants in *S. cerevisiae*: a wild type and an expanded AT3 variant carrying 26 (AT3Q26) and 85 (AT3Q85) consecutive glutamines, respectively, and a variant truncated immediately upstream of the polyQ (AT3291Δ). All constructs were in fusion with GFP at the C-terminus. We first demonstrated that the expression of expanded form induces a significant growth-inhibitory effect. Although statistically non-significant, AT3291Δ-expressing strain also exerted some effect. So, the polyQ-harboring context may also play a role, although this hypothesis deserves further investigations. Nevertheless, a toxic effect of AT3 variants truncated upstream of the polyQ stretch has been demonstrated in a previous study showing that mice, both homozygous and heterozygous for the truncated AT3259Δ, developed severe motor coordination dysfunction and altered behavior, followed by premature death [257].

A hallmark of SCA3 pathology is the presence of amyloid aggregates in the brain. Through fluorescence microscopy analysis, we showed the formation of aggregation *foci* in the AT3Q85-expressing strain starting from 16 h after induction. This phenotype may be accounted for by the intrinsic properties of the protein rather than by its overexpression, as substantiated by the fact that AT3Q26- and AT3291Δ-expressing strains did not show any such aggregates, although the three variants were expressed at similar levels. Filter trap analysis performed after 24 h of induction also showed that only the aggregates formed by the expanded variant are SDS insoluble. At 16 h after the induction, filter trap analysis did not show any signal (data not shown), in contrast with microscopy observations. This suggests the aggregates observed

at 16 h are not SDS-insoluble mature fibrils but pre-fibrillar species. Also, SDS-insoluble aggregates were not formed at any time in AT3291Δ and AT3Q26 strains, in agreement with a previous study [258].

To assess the effect of protein expression on strain viability, we performed MTT assays, which highlighted a significant decrease in viability induced by the pathological and truncated variants compared to the wild type.

Seeking for possible mechanisms of toxicity, we assessed possible oxidative stress. Indeed, it is reported that amyloid aggregates may increase reactive oxygen species (ROS), a phenomenon which in turn results from mitochondrion dysfunction [259]. We found that already 16 h after induction, H_2O_2 levels were significant higher in yeast expressing AT3Q85 and AT3291Δ compared to AT3Q26. At 24 h, the increase was significant only for the expanded form and, at the latest time, the levels of the three strains were comparable, probably due to culture aging. We also assessed whether cells expressing expanded AT3 showed alterations in the antioxidant defense system. In particular, we observed that the ratio reduced (GSH) to total glutathione was significantly lower in cells expressing AT3Q85 with respect to the two other strains. In addition, total glutathione remained the same of the control cells (data not shown).

To dissect further the mechanisms that mediate the altered redox status in our model, we examined the cellular enzymatic defense system against oxidative stress, by assaying CAT and SOD levels. Our results revealed markedly increased activity of CAT at 16 h of induction in the yeast expressing AT3Q85 and AT3291Δ compared to AT3Q26. At 24 h, the increase was significant only for the expanded form and at 48 h the levels were almost identical and very similar to the control strain (empty vector). SOD significantly

increased in the AT3291Δ strain at 24 and 48 h of induction, whereas in the case of AT3Q85 the increase was significant at 48 h only.

Summarizing, in the AT3Q85-expressing strain an increase in ROS levels is paralleled by a fast GSH drop and a significant increase in CAT activity. Conversely, SOD activity increases after 48 h of induction. One possible explanation for these results may be related to the failure of AT3Q85 and AT3291Δ strains to effectively degrade H_2O_2 by thiol groups, although there seems to be a compensatory mechanism that increases catalase and SOD levels compared to the control. Moreover, these data suggest that the SDS-soluble aggregates formed at 16 h induce mitochondrial damage, increase in ROS species and a consequent imbalance of the antioxidant defense system. These findings are in line with the hypothesis that oligomeric and pre-fibrillar species formed at the initial stages of the aggregation process are those responsible for cellular toxicity. Expression of AT3291Δ showed a toxic effect, even if milder than expanded form.

Another toxicity mechanism known in neurodegenerative diseases is the capability of amyloid aggregates to interact with lipid membranes and induce membrane permeabilization [13-15]. For this reason, PI-staining analyses were performed to evaluate membrane integrity. Data obtained show that ~10% of AT3Q85 expressing strain underwent plasma membrane integrity and cell necrosis after 48 h of induction, which is over three-fold compared with the control strain (empty vector) and over two-fold compared with the wild type AT3 expressing strain. In contrast, AT3291Δ did not show any significant difference with respect to the AT3Q26 strain.

In conclusion, this work shows that *S. cerevisiae* is a good model to study SCA3, as supported by the fact that the expression of AT3 expanded form causes reduced cell viability and formation of protein aggregates, unlike

the wild type protein. The expression of the truncated form also produces a similar, although milder, phenotype. We propose that protein aggregates cause oxidative stress in the short-term, whereas long term effects might affect cell membrane integrity.

In the future we plan to improve our knowledge on the mechanisms of cell death observed in the strain expressing the pathological forms, verifying in particular if oxidative stress could trigger apoptosis.

Chapter Four

Investigations on modifiers of ataxin-3 aggregation

4.1 AIM OF THE WORK

The hallmark of amyloidosis is the deposition of proteins that abnormally self-assemble into insoluble fibrils that leads to an impairment in tissue-organ function. Increasing evidence suggests that the most toxic species are not mature amyloid fibrils, but pre-fibrillar oligomeric species [8, 9]. In agreement with this hypothesis, it was also proposed that the formation of mature fibrillar aggregates may play a role as a defense mechanism for the cell [10]. The discovery of molecules that inhibit protein deposition or reverse fibril formation could certainly open new avenues for developing therapeutic strategies aimed to prevent or control the corresponding amyloid-related diseases. Different classes of structurally unrelated compounds have been investigated for their ability to interfere with protein self-aggregation and stability of amyloid fibers [260]. To date, no effective treatment has been developed for SCA3 disease and no compounds were tested on AT3 aggregation process. For this reason, we focused our attention to study two different classes of compounds which have been found to influence the polymerization process of many amyloid proteins: (i) epigallocatechin-3-gallate (EGCG) and (ii) tetracycline.

In particular, we have evaluated the effect of tetracycline and EGCG on the aggregation process and on the toxicity of an AT3 expanded variant We also have analyzed the capability of the two compounds to disassemble preformed AT3-amyloid fibrils. To provide insight into the structural changes of AT3 fibrillogenesis, we have taken advantage of Fourier Transform Infrared spectroscopy (FTIR), a powerful technique that provides information on protein secondary structure content, and of Atomic Force Microscopy (AFM) to highlight the morphology of the aggregates. Finally, we have performed MTT

assays on mammalian cells to evaluate the toxicity of the species formed in the presence and the absence of the compounds under investigation.

4.2 EXPERIMENTAL PROCEDURES

Purification of AT3Q55

AT3Q55 gene was previously cloned in pQE30 vector and the protein was expressed in SG13009 (E. coli K12 Nals, StrS, RifS, Thi−, Lac−, Ara+, Gal+, Mtl−, F−, RecA+, Uvr+, Lon+; Qiagen Hamburg GmbH, Hamburg, Germany) as His-tagged protein [135]. Cells were grown at 37 °C in LB-ampicillin-kanamycin medium, induced with 1 mM IPTG at A600 0.8 for 45 min at 30 °C. To obtain crude extract, pelleted cells were resuspended in lysis buffer (5 ml/g wet weight; 25 mM potassium phosphate, pH 7.2, 150 mM NaCl, 0.5 mM phenylmethanesulfonyl fluoride, 10 mM imidazole, 10% glycerol, 1 mM 2-mercaptoethanol, 1 mg/ml lysozyme plus protease inhibitors cocktail) and incubated for 30 min at 4 °C. The cell suspension was then sonicated in 3 pulses of 30 s each. DNase I (0.2 mg/g of cells, wet weight) was added, and the sample further incubated for 30 min at room temperature. Finally, it was centrifuged for 45 min at 20,000 × g. The supernatant was filtered through a 0.45 µm pore size SFCA membrane (Corning) and loaded onto HisPur™ Cobalt Resin (Thermo Fisher Scientific, Rockford, IL, USA) and washed with 20 bed volumes of Wash Buffer (25 mM potassium phosphate, pH 7.4, 150 mM NaCl, 2 mM phenylmethanesulfonyl fluoride, 10 mM imidazole, 10% glycerol, 1 mM 2-mercaptoethanol). The bound protein was then eluted with Elution buffer (25 mM potassium phosphate, pH 7.4, 150 mM NaCl, 2 mM phenylmethanesulfonyl fluoride, 150 mM imidazole, 10% glycerol, 1 mM 2-mercaptoethanol). Protein was stored at -80 °C. Before each experiment,

protein fractions were thawed and loaded on a Superose 12 10/300 GL gel filtration column (GE Healthcare, Life Sciences, Little Chalfont, England), pre-equilibrated with PBS (25 mM potassium phosphate, pH 7.2, 150 mM NaCl). Elution was performed at a flow rate of 0.5 ml/min in the same buffer. Fractions were collected and protein content was determined using Coomassie brilliant blue G-250 (Thermo Scientific Rockford, IL USA) and bovine serum albumin as a standard protein.

SDS-PAGE and densitometry analysis of soluble protein fraction

Purified AT3Q55 (25 µM) was incubated at 37°C in PBS buffer in presence or in absence of EGCG and tetracycline (Sigma-Aldrich, St. Louis, MO, USA) at a molar ratio protein/compound of 1:1 or 1:5. AT3 aliquots at different times of incubation (0, 3, 6, 24, 48, 72 h) were centrifugated at 14.000xg for 15 min and 10 µl of the supernatants were subjected to SDS-PAGE. The gels were stained with Imperial Protein Stain (Thermo Scientific Rockford, IL USA), scanned at 700 nm with Odyssey® Fc System (LiCor, Lincoln, USA) and analyzed with Image Studio software (LiCor, Lincoln, USA).

FTIR spectroscopy

For the FTIR analyses, purified AT3Q55 (25 µM) was incubated at 37 °C in PBS buffer in presence or in absence of EGCG and tetracycline at a molar ratio protein/compound of 1:1 or 1:5. Measurements were performed in attenuated total reflection (ATR) on a single reflection diamond element (Golden Gate, USA). An aliquot of about 5-10 µl of the samples at different times of incubation (0-1-3-6-24-30-48-144 h and 2 weeks) was deposited on the diamond ATR plate and dried at room temperature in order to obtain a protein hydrated film. Its ATR/FTIR spectrum was then measured using the

FTS40-A spectrometer (Digilab, USA), equipped with a nitrogen cooled Mercury Cadmium Telluride (MCT) detector and carefully purged by dry air to avoid interference with water vapor under the following conditions: 2 cm^{-1} spectral resolution, 20 kHz scan speed, 1000 scan co-additions, triangular apodization. Second derivatives of the spectra were obtained by the Savitzky-Golay algorithm (5 points), after an 11 point binomial smoothing of the measured spectra, using the software Grams/AI (Thermogalactic, USA).

Atomic Force Microscopy (AFM)

AT3Q55 was purified by gel filtration and thawed before the AFM experiments. 25 µM AT3Q55 was incubated at 37 °C in PBS buffer in presence or in absence of EGCG and tetracycline at a molar ratio protein/compound of 1:5. At fixed aggregation times, a 10 µl aliquot was withdrawn, incubated on a freshly cleaved mica substrate for 5 min, then rinsed with Milli-Q water and dried under mild vacuum. AFM images were acquired in tapping mode in air using a Dimension 3100 Scanning Probe Microscope equipped with a 'G' scanning head (maximum scan size 100 mm) and driven by a Nanoscope IIIa controller, and a Multimode Scanning Probe Microscope equipped with ''E'' scanning head (maximum scan size 10 mm) and driven by a Nanoscope IV controller (Digital Instruments – Bruker). Single beam uncoated silicon cantilevers (type OMCL-AC160TS, Olympus) were used. The drive frequency was between 270 and 330 kHz, the scan rate was between 0.5 and 0.8 Hz.

MTT assay

COS-7 cells were cultured in DMEM supplemented with 10% (v/v) fetal bovine serum (FBS), 100 U/ml penicillin, 100 µg/ml streptomycin and 4 mM L-glutamine, maintained at 37 °C in a humidified 5% CO2 incubator. For

MTT assays, cells were trypsinized and plated at a density of 10,000 cells per well on 96-well plates in 100 µL fresh medium without phenol red. After 24 h, 25 µM AT3-Q55 alone or co-incubated with the two compounds (1:1 and 1:5 molar ratio) at different times (3,6,24 h) were added to the cell medium at a final concentration of 2.5 µM and cells were further incubated for 1 h at 37 °C. Then MTT were added to cells at a final concentration of 0.5 mg/ml. Absorbance values of formazan were determined at 570 nm with an automatic plate reader after 2 h.

4.3 RESULTS

EGCG and tetracycline affect AT3 aggregates solubility

In recent years, plenty of evidence has highlighted a critical role for soluble oligomeric amyloid species in triggering cellular toxicity. Here, we examined whether the addition of EGCG and tetracycline to aggregation reaction mixtures can affect the aggregation of the species formed during fibrillogenesis. Initially, a His-tagged expanded variant of AT3 was purified by affinity chromatography. In order to isolate monomeric protein, the sample was further subjected to a size exclusion chromatography. The elution profile is presented (Fig. 4.1).

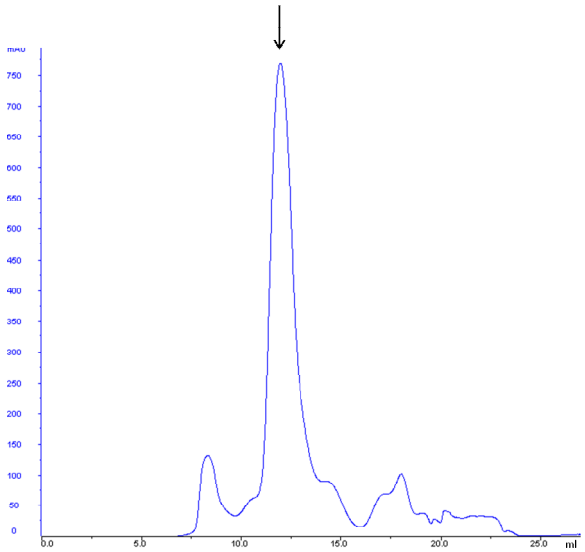

Fig. 4.1 SEC profile of AT3Q55 on a Superose 12 10/300 GL in PBS buffer. 10 mg His-tagged AT3Q55 was loaded onto a gel filtration column. The arrow indicates the peak corresponding to the AT3Q55 monomeric form used for the experiments**.**

Monomeric protein was incubated at 37 °C in the presence or the absence of different amounts of the two compounds (1:1 and 1:5 molar ratios). Aliquots were taken at different times of incubation and the soluble fraction was isolated as the supernatant from a centrifugation at 14.000 x g. SDS-PAGE (Fig. 4.2A) and the respective densitometric analyses (Fig. 4.2B) of AT3Q55 soluble fraction showed a decrease in the SDS-soluble amount of the protein in the presence of EGCG at the earliest time of incubation (3 h) relative to the untreated protein; in contrast, tetracycline somewhat retarded the disappearance of SDS-soluble protein. The effects were best detected at a 1:5 protein-compound molar ratio and, to a lesser extent, at a molar ratio 1:1.

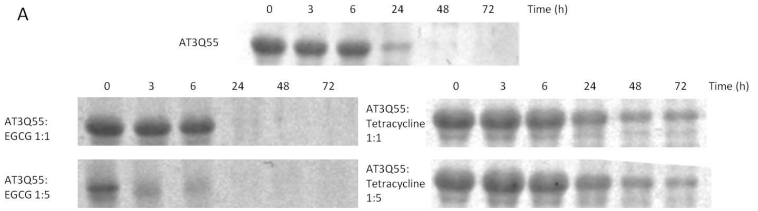

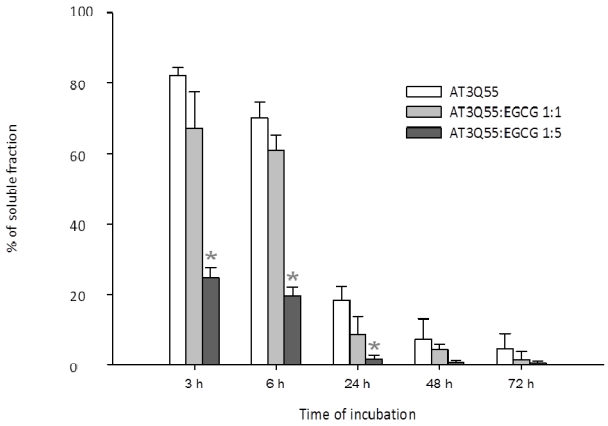

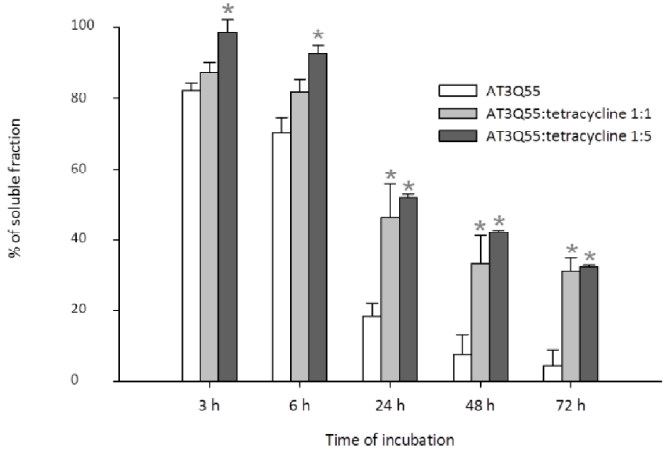

Fig. 4.2 Soluble protein fraction analysis of AT3Q55 incubated in the presence or the absence of EGCG or tetracycline. A) Soluble fractions obtained by centrifugation of aliquots of AT3Q55 (25 μM) incubated at 37 °C in the presence or the absence of compounds at a molar ratio protein/compound of 1:1 or 1:5, were collected at different times and subjected to SDS-PAGE. B) Soluble protein fraction was quantified by densitometry. Signals were normalized at t = 0 h protein content (considered as 100% of solubility). Error bars represent standard errors and are derived from at least three independent experiments. * $P < 0.05$.

Surprisingly, the reduced solubility of EGCG-treated protein was paralleled by the appearance of large SDS-insoluble aggregates in the soluble fraction (Fig. 4.3). Thus, EGCG seems to interact with the protein and to induce the formation of soluble SDS-resistant species, which are found in the supernatant already after 3 h of incubation. These soluble aggregates are large in size and do not enter the separating gel (>200 kDa). In contrast, in time course experiments without EGCG, large SDS-resistant complexes were detected only after 24 h. Instead, tetracycline treatment yielded a pattern qualitatively similar to that of untreated protein, in particular as regards SDS-insoluble species accumulation.

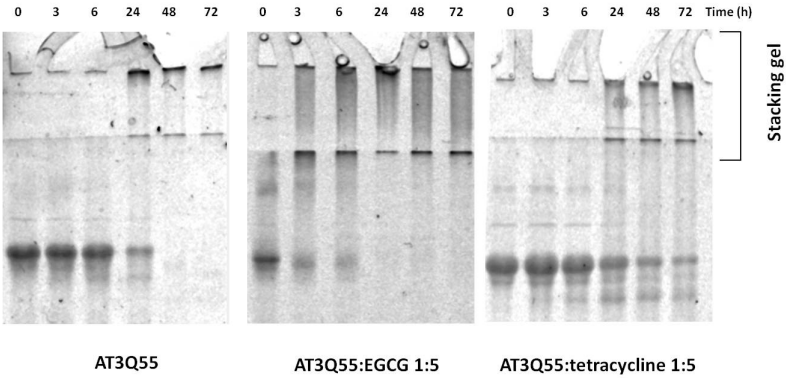

Fig. 4.3 SDS-PAGE of the soluble protein fraction of AT3Q55, AT3Q55/EGCG 1:5 and AT3Q55/tetracycline 1:5. Soluble fractions of AT3Q55 in the presence or the absence of the compounds were collected at the indicated times of incubation and subjected to SDS-PAGE.

EGCG, but not tetracycline, drastically affects aggregation kinetics of AT3Q55

To achieve a deeper understanding of the structural changes in AT3Q55 fibrillogenesis in the presence of either compounds, we performed FTIR spectroscopy analyses by monitoring the time-dependent structural changes. However, we first assessed the secondary structure content of freshly purified protein. In Fig. 4.4 A, the absorption spectrum of the AT3Q55 in the amide I band region is presented. This is mainly contributed by the C=O peptide bond absorption whose peak position is sensitive to the protein's secondary structure [261, 262]. In order to resolve this band into its overlapping components, the second derivative analysis of the spectrum was performed. Two main components, appearing as negative peaks, were detected at 1657 and 1635 cm^{-1}. The former can be assigned to α-helices and random coils; the latter, along with a shoulder around 1690 cm^{-1}, to native, intramolecular β-sheets. In addition, a low-intensity component at about 1688 cm^{-1} was found in the typical absorption region of β-turns. It is also noteworthy

that the glutamine side-chain infrared response, which in the amide I region is expected in the ranges 1687– 1668 cm^{-1} and 1611–1586 cm^{-1} [263], was undetectable in the freshly purified AT3Q55 spectrum.

To assess the changes in secondary structure associated with the aggregation process, we incubated AT3Q55 in the presence or the absence of either EGCG or tetracycline at a molar ratio of 1:5 at 37 °C, and collected FTIR spectra at different times. In the second derivative spectra of AT3Q55 alone, we observed that the native β-sheet component at 1635 cm^{-1} underwent a decrease in intensity starting from the earliest times of incubation, which indicates misfolding of the Josephin domain. The band of *inter*molecular β-sheet structures around 1624 cm^{-1} started to increase from 3 h, reaching very high intensities at the longest times of incubation. We also observed an additional band at 1604 cm^{-1} that was assigned to NH_2 deformation modes of the glutamine side chains involved in strong side chain-side chain (and possibly side chain-backbone) hydrogen bonding in the mature amyloid aggregates [135] that appeared from 144 h of incubation (Fig. 4.4 B).

FTIR spectra in the presence of tetracycline did not show any significant difference compared with AT3Q55 alone. Thus, based on the sole FTIR data, the mechanism by which tetracycline affects protein fibrillogenesis cannot be defined (Fig. 4.4 C).

A completely different behavior was observed in the presence of EGCG. In fact, we observed that the native β-sheet component underwent a faster decrease in intensity compared with AT3Q55, indicating a very early misfolding of the Josephin domain. The aggregation band of *inter*molecular β-sheet structures displayed a faster increase at 1 h but remained at very low intensity until the end of incubation; instead, glutamine side-chain band did not appear even at very long times of incubation (Fig. 4.4 D).

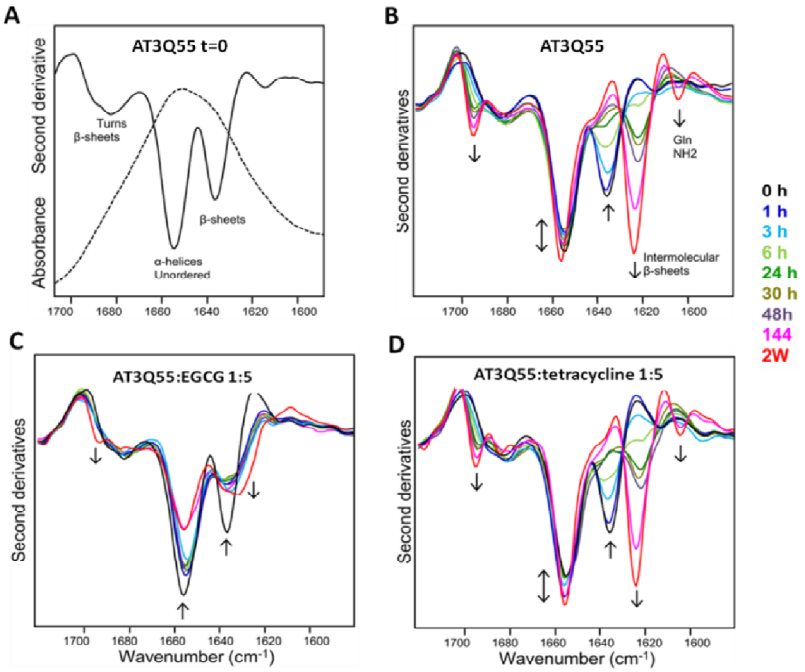

Figure 4.4 FTIR spectra of freshly purified AT3Q55 and kinetics of aggregation of AT3Q55 incubated in the presence or the absence of EGCG or tetracycline. A) Absorption spectra (dotted line) and their second derivatives (continuous line) in the amide I region of AT3Q55. Band assignment to the secondary structure components is indicated. B-C-D) Second derivative spectra of ATQ55 in the presence or the absence of compounds were taken at different times of incubation in PBS at 37 °C. Arrows point to increasing time.

Morphology of EGCG and tetracycline AT3 aggregates

Tapping mode atomic force microscopy was employed to get insight into the effects of EGCG and tetracycline on the morphology of aggregates formed by AT3Q55. Representative images are reported in Fig. 4.5. Bundles of fibrils were observed for AT3Q55 alone after 24 h and 48 h aggregation, in keeping with previous observations. Instead, in the presence of EGCG no such bundles were detected. After 24 h, the sample mainly consists of globular

particles, isolated or associated in small clusters. After 48 h, large clusters of non-fibrillar material were found.

A completely different behavior was found in the presence of tetracycline. At both aggregation times analyzed, the drug did not apparently inhibit fibril formation. However, many irregular and compact aggregates also appeared along with mature fibrils.

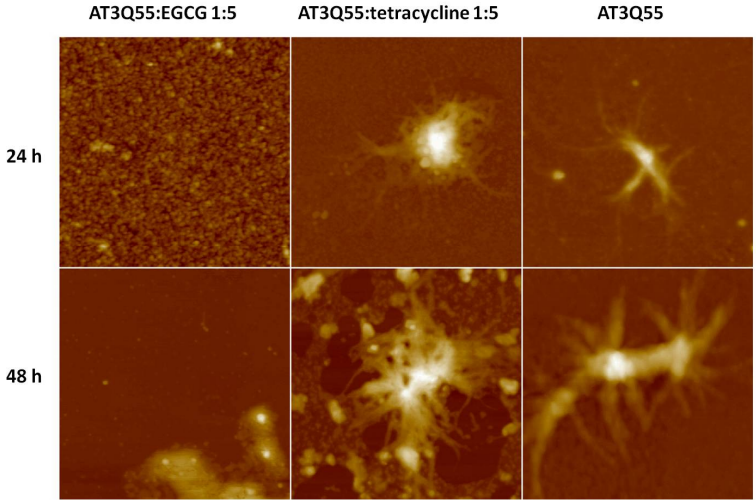

Fig. 4.5 Tapping mode AFM images (height data) of AT3Q55 aggregates obtained after 24h (top) or 48 h (bottom) incubation in the presence of EGCG (left), tetracycline (middle), or in the absence of either compounds (right). Scan size 1.9 µm; Z range (from top to bottom): AT3Q55 + EGCG, 20 nm, 80 nm; AT3Q55 + Tetracycline, 200 nm, 100 nm; AT3Q55, 110 nm, 150 nm.

EGCG and tetracycline do not disrupt AT3Q55 preformed fibrils

To study the effect of EGCG and tetracycline on preformed amyloid aggregates, we first produced AT3Q55 fibrils by incubating the protein at 37 °C for 2 weeks in PBS. Then, the fibrils were resuspended in the presence or the absence of EGCG or tetracycline at a molar ratio of 1:5. FTIR analyses,

performed on the fibrils before and after the addition of the either compounds, did not show any difference, indicating that EGCG and tetracycline are not able to revert mature AT3 fibrils (Fig. 4.6).

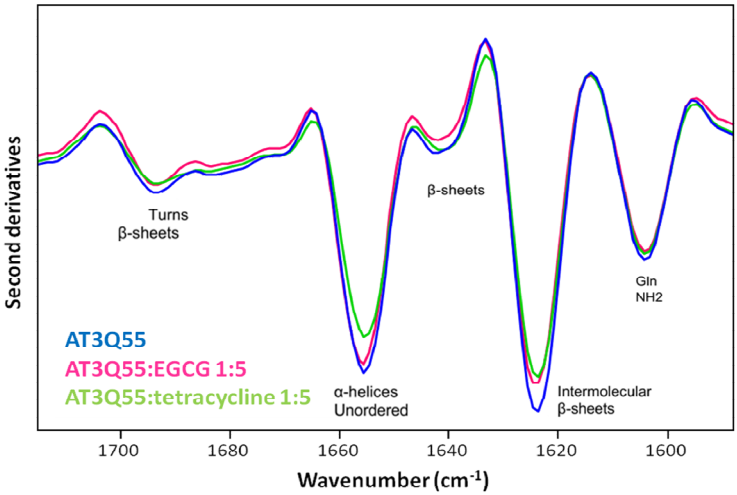

Fig. 4.6 FTIR spectra of AT3Q55 fibrils. Second derivative spectra of AT3Q55 fibrils resuspended in PBS (blue), 125 µM EGCG (magenta) or 125 µM tetracycline (green) and incubated for 24 h at 37 °C.

Both EGCG and tetracycline treatments reduce AT3Q55 toxicity

Finally, we examined the toxicity of AT3Q55 species formed in presence or absence of EGCG and tetracycline. AT3Q55 aliquots at different times of incubation were added to COS7 cells medium and toxicity was analyzed using an MTT assay (Fig. 4.7). AT3Q55 aggregates after 3 or 6 h of incubation inhibited MTT reduction (~60%), but no such effect was observed when cells were incubated with AT3Q55 aggregates generated in the presence of either EGCG or tetracycline and otherwise under the same conditions. This suggests that these treatments significantly reduce the toxicity of AT3Q55

aggregates. At 24 h of incubation, no significant differences were detectable among the three samples.

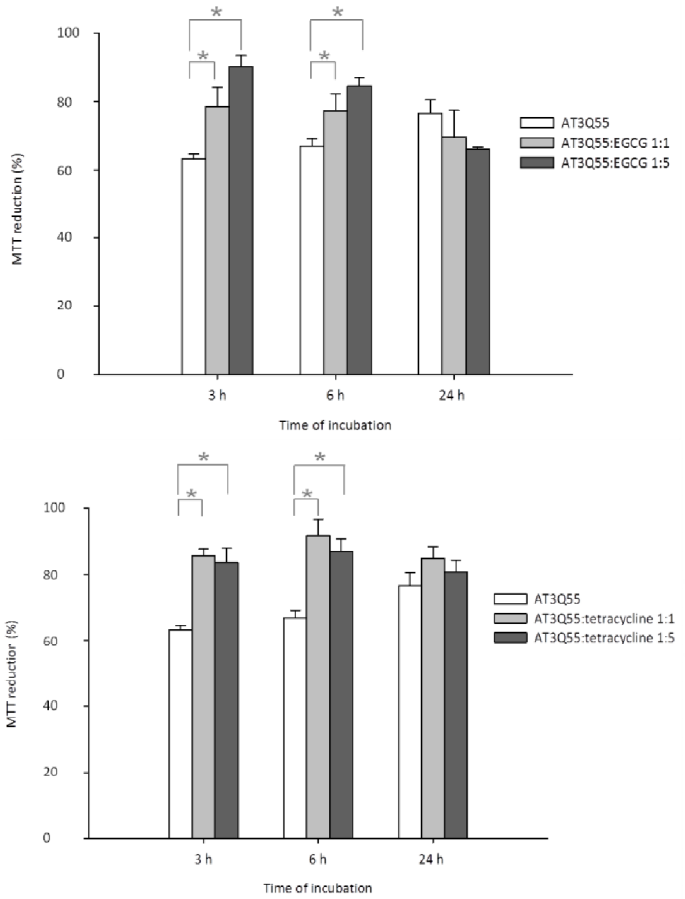

Fig. 4.7 AT3Q55 toxicity assay. AT3Q55 25 µM were incubated alone, with EGCG or tetracycline (molar ratio 1:1 and 1:5) for the indicated times, and aliquots were diluted in cell culture medium to a protein final concentration of 2.5 µM. Metabolic activity was monitored by MTT reduction. Bars represent standard errors and are derived from at least three independent experiments. Values are normalized to not treated cells; * $P < 0.05$.

4.4 DISCUSSION

The green tea polyphenol EGCG and the antibiotic tetracycline are attractive candidates for the treatment of neurodegenerative diseases because of its proven safety record in humans and its blood–brain barrier permeability. Moreover, the anti amyloidogenic effect of these two compounds on many amyloid proteins is well established [118, 119, 132]. In this study, our investigations are focused on SCA3 disease treatment; in fact, no cure or suitable therapeutic compound has been identified yet. We therefore aimed at verifying if EGCG and tetracycline display anti-amyloidogenic activity on AT3 aggregation.

Although our data show that the polyphenol EGCG speeds up protein aggregation, nevertheless they also indicate that the resulting aggregates differ in nature from canonical fibrillar end products. We first observed that, when incubated with expanded AT3, the compound induces the formation of large SDS-resistant protein aggregates, which remain in the supernatant after centrifugation. FTIR analysis revealed that EGCG interferes with a very early step of the amyloid pathway, accelerating misfolding of the Josephin domain and preventing the conversion of the protein into stable, β-sheet–rich structures. The mechanism by which EGCG redirects native AT3 into SDS-stable aggregates is unclear. In the future, NMR analyses we will perform to clarify the nature of protein-drug interaction. AFM analysis also confirmed EGCG prevents the formation of mature fibrils from native monomeric protein and induces the formation of larger spherical amorphous species. Our results are in keeping with the common hypothesis that EGCG prevents on-pathways leading to toxic amyloid oligomers and protofibrils of amyloid proteins. Instead, highly stable off-pathway EGCG-containing spherical aggregates were assembled. This

effect quite likely justifies the protective effect of the drug we have detected by the MTT assay.

In contrast, tetracycline somewhat retarded the disappearance of SDS-soluble species, although FTIR analyses did not detect significant changes in aggregation kinetics and secondary structure compared to the untreated protein. The formation of amyloid fibrils was confirmed by AFM analyses. They also revealed the presence of irregular and compact aggregates along with mature fibrils.

On the whole, our data do not reveal a dramatic impact of tetracycline treatment on aggregation kinetics and on the structural features of the intermediates, the only appreciable difference being a somewhat retarded disappearance of the SDS-soluble species. Nevertheless, the treatment leads to a significant reduction in toxicity. This might be due to a lower steady-state accumulation of the toxic species and/or to subtle structural changes, not detectable by our analytical methods. Our results seem to be conflicting with previous studies, in which tetracycline more dramatically inhibits fibrillogenesis of different proteins, such as PrP and α-syn [222]. Future NMR studies might shed light on the mode of interaction between AT3 and tetracycline, thus clarifying its mechanism.

It is also known that EGCG and tetracycline are generally able to remodel mature amyloid fibrils [212, 222]. However, the two compounds could not disrupt AT3 mature fibrils. This is probably due to the presence of glutamine side-chain hydrogen bonding that contributes to the stability of the SDS-insoluble polyQ mature fibers [135].

Besides further investigation on the molecular mechanisms of protein-drug interaction, we will also assess the protective effects of these compounds in the *Caenorhabditis elegans* animal model.

References

[1] F. Chiti and C.M. Dobson (2006) Protein misfolding, functional amyloid and human disease. *Annu. Rev. Biochem.,* **75**, 333-366.

[2] C. Soto (2003) Unfolding the role of protein misfolding in neurodegenerative disease. *Nature Reviews,* **4**, 49-60.

[3] H. Naiki, N. Hashimoto, S. Suzuki, H. Kimura, K. Nakakuki and F. Gejyo (1997) Establishment of a kinetic model of dialysis-related amyloid fibril extension in vitro. *Amyloid,* **4**, 223–232.

[4] T. Serio, A. Cashikar, A. Kowal, G. Sawicki, J. Moslehi, L. Serpell, M. Arnsdorf and S. Lindquist (2000) Nucleated Conformational Conversion and the Replication of Conformational Information by a Prion Determinant. *Science,* **289**, 1317–1321.

[5] V. Uversky, J. Li, Souillac, I. Millett, S. Doniach, R. Jakes, M. Goedert and A. Fink (2002) Biophysical properties of the synucleins and their propensities to fibrillate: inhibition of alpha-synuclein assembly by beta- and gamma-synucleins. *J. Biol. Chem.,* **277**, 11970–11978.

[6] J. Pedersen, G. Christensen and D. Otzen (2004) Modulation of S6 fibrillation by unfolding rates and gatekeeper residues. *J. Mol. Biol.,* **341**, 575-588.

[7] M. Bucciantini, G. Calloni, F. Chiti, L. Formigli, D. Nosi, C. M. Dobson and M. Stefani (2004) Prefibrillar amyloid protein aggregates share common features of cytotoxicity. *J. Biol. Chem.,* **279**, 31374-31382.

[8] C. Glabe (2008) Structural classification of toxic amyloid oligomers. *J. Biol. Chem.,* **238**, 29639-29643

[9] M. Bucciantini, E. Giannoni, F. Chiti, F. Baroni, L. Formigli, J. Zurdo, N. Taddei, G. Ramponi, C. Dobson and M. Stefani (2002) Inherent toxicity of aggregates implies a common mechanism for protein misfolding diseases. *Nature,* **416**, 507-511.

[10] S. Wickner, M. Maurizi and S. Gottesman (1999) Posttranslational quality control: folding, refolding, and degrading proteins. *Science ,* **286**, 1888-1893.

[11] J. T. Giurleo, X. He and D.S. Talaga (2008) Beta-Lactoglobulin assembles into amyloid through sequential aggregated intermediates. *J. Mol. Biol.,* **381**, 1332-1348.

[12] M. Stefani and C.M. Dobson (2003) Protein aggregation and aggregate toxicity: new insights into protein folding, misfolding diseases and biological evolution. *J. Mol. Med. (Berl),* **81**, 678-699.

[13] J. McLaurin and A. Chakrabartty (1997) Characterization of the interactions of Alzheimer beta-amyloid peptides with phospholipid membranes. *Eur. J. Biochem.,* **245**, 355–363.

[14] M. Lindgren and Hammarstrom (2010) Amyloid oligomers: spectroscopic characterization of amyloidogenic protein states. *FEBS J.,* **277**, 1380–1388.

[15] S. Jayasinghe and R. Langen (2007) Membrane interaction of islet amyloid polypeptide. *Biochim. Biophys. Acta ,* **1768**, 2002–2009.

[16] Z. Oren and Y. Shai (1998) Mode of action of linear amphipathic alpha-helical antimicrobial peptides. *Biopolymers,* **47**, 451–463.

[17] E. Ahmad, A. Ahmad, S. Singh, M. Arshad, A. Khan and R. Khan (2011) A mechanistic approach for islet amyloid polypeptide aggregation to develop anti-amyloidogenic agents for type-2 diabetes. *Biochimie,* **93**, 793–805.

[18] E. Gazit, A. Boman, H. Boman and Y. ShaiI (1995) Interaction of the mammalian antibacterial peptide cecropin P1 with phospholipid vesicles. *Biochemistry,* **34**, 11479–11488.

[19] Y. Pouny, D. Rapaport, A. Mor, Nicolas and Y. Shai (1992) Interaction of antimicrobial dermaseptin and its fluorescently labeled analogues with phospholipid membranes. *Biochemistry ,* **31**, 12416–12423.

[20] B. Tabner, S. Turnbull, O. El-Agnaf and D. Allsop (2001) Production of reactive oxygen species from aggregating proteins implicated in Alzheimer's disease, Parkinson's disease and other neurodegenerative diseases. *Curr. Top Med. Chem.,* **1**, 507–517.

[21] X. Huang, C. Atwood, M. Hartshorn, G. Multhaup, L. Goldstein, R. Scarpa, M. Cuajungco, D. Gray, J. Lim, R. Moir, R. Tanzi and A. Bush (1999) The A beta peptide of Alzheimer's disease directly produces hydrogen peroxide through metal ion reduction. *Biochemistry,* **38**, 7609–7616.

[22] S. Turnbull, B. Tabner, O. El-Agnaf, S. Moore, Y. Davies and D. Allsop (2001) Alpha-synuclein implicated in Parkinson's disease catalyses the formation of hydrogen peroxide in vitro. *Free Radic. Biol. Med,* **30**, 1163–1170.

[23] S. Turnbull, B. Tabner, D. Brown and D. Allsop (2003) Copper-dependent generation of hydrogen peroxide from the toxic prion protein fragment PrP 106-126. *Neurosci. Lett.,* **336**, 159–162.

[24] N. Ansari and F. Khodagholi (2013) Molecular mechanism aspect of ER stress in Alzheimer's disease: current approaches and future strategies. *Curr. Drug Targets,* **14**, 114–122.

[25] G. Mercado, Valdes and C. Hetz (2013) An ERcentric view of Parkinson's disease. *Trends Mol. Med.,* **19**, 165–175.

[26] C. Huang, L. Haataja, T. Gurlo, A. Butler, X. Wu, W. Soeller and P.C. Butler (2007). Induction of endoplasmic reticulum stress-induced beta-cell apoptosis and accumulation of polyubiquitinated proteins by human islet amyloid polypeptide. *Am. J. Physiol. Endocrinol. Metab.,* **293** , 1656–1662,

[27] T. Umeda, T. Tomiyama, N. Sakama, S. Tanaka, M. Lambert, W. Klein and H. Mori (2011) Intraneuronal amyloid beta oligomers cause cell death via endoplasmic reticulum stress, endosomal/lysosomal leakage, and mitochondrial dysfunction in vivo,. *J. Neurosci. Res.,* **89** , 1031–1042.

[28] R. Quiroz-Baez, Ferrera, R. Rosendo-Gutierrez, J. Moran, F. Bermudez-Rattoni and C. Arias (2011) Caspase-12 activation is involved in amyloid-beta protein-induced synaptic toxicity. *J. Alzheimers Dis.,* **26**, 467–476.

[29] E. Ferreiro, I. Baldeiras, I. Ferreira, R. Costa, A. Rego, C. Pereira and C. Oliveira (2012) Mitochondrial- and endoplasmic reticulum-associated oxidative stress in Alzheimer's disease: from pathogenesis to biomarkers. *Int. J. Cell Biol.,* **2012**, 735206.

[30] X. Li, T. Chen, Y. Wong, G. Xu, R. Fan, H. Zhao and J. Chan (2011) Involvement of mitochondrial dysfunction in human islet amyloid polypeptide-induced apoptosis in INS-1E pancreatic beta cells: an effect attenuated by phycocyanin. *Int. J. Biochem. Cell Biol.,* **43**, 525–534.

[31] T. Cali, D. Ottolini and M. Brini (2011) Mitochondria, calcium, and endoplasmic reticulum stress in Parkinson's disease. *Biofactors,* **37**, 228–240.

[32] M. Hsu, J. Sheu, C. Lin, M. Shen and C. Hsu (2010) Mitochondrial mechanisms in amyloid beta peptide-induced cerebrovascular degeneration. *Biochim. Biophys. Acta,* **1800**, 290–296.

[33] M. Hashimoto, E. Rockenstein, L. Crews and E. Masliah (2003) Role of protein aggregation in mitochondrial dysfunction and neurodegeneration in Alzheimer's and Parkinson's diseases. *Neuromolecular Med.,* **4**, 21–36.

[34] S. Cardoso, S. Santos, R. Swerdlow and C. Oliveira (2001) Functional mitochondria are required for amyloid beta-mediated neurotoxicity. *FASEB J.,* **15**, 1439–1441.

[35] B. Cheng, H. Gong, H. Xiao, R. Petersen, L. Zheng and K. Huang (2013) Inhibiting toxic aggregation of amyloidogenic proteins: A therapeutic strategy for protein misfolding diseases. *Biochem. Biophys. Acta,* **1830**, 4860–4871.

[36] A. Jeffreys, J. Holloway, L. Kauppi, C. May, R. Neumann, M. Slingsby and A. Webb (2004) Meiotic recombination hot spots and human DNA diversity. *Philos. Trans. R. Soc. Lond. B. Biol. Sci.,* **359**, 141-152.

[37] I. Kovtun and C. McMurray (2008) Features of trinucleotide repeat instability in vivo. *Cell. Res.,* **18**, 198-213.

[38] J. Gatchel and H. Zoghbi (2005) Diseases of unstable repeat expansion: mechanisms and common principles. *Nat. Rev. Genet.,* **6**, 743–755.

[39] J. Shao and M. Diamond (2007) Polyglutamine diseases: emerging concepts in pathogenesis and therapy. *Hum. Mol. Genet.,* **Spec No. 2**, R115-123.

[40] H. Zoghbi and H. Orr (2000) Glutamine repeats and neurodegeneration. *Annu. Rev. Neurosci.,* **23**, 217–247.

[41] C. Matos, S. de Macedo-Ribeiro and A. Carvalho (2011) Polyglutamine diseases: The special case of ataxin-3 and Machado–Joseph disease. *Progress in Neurobiology,* **95**, 26-48.

[42] A. Durr, G. Stevanin, G. Cancel, C. Duyckaerts, N. Abbas, O. Didierjean, H. Chneiweiss, A. Benomar, O. Lyon-Caen, J. Julien, M. Serdaru, C. Penet, Y. Agid and A. Brice (1996) Spinocerebellar ataxia 3 and Machado–Joseph disease: clinical, molecular, and neuropathological features. *Ann. Neurol.,* **39**, 490–499.

[43] Maciel, C. Gaspar, A. DeStefano, I. Silveira, Coutinho, J. Radvany, D. Dawson, L. Sudarsky, J. Guimaraes, J. Loureiro et al. (1995) Correlation between CAG repeat length and clinical features in Machado–Joseph disease. *Am. J. Hum. Genet.,* **57**, 54–61.

[44] L. Ranum, J. Lundgren, L. Schut, M. Ahrens, S. Perlman, J. Aita, T. Bird, C. Gomez and H. Orr (1995) Spinocerebellar ataxia type 1 and Machado–Joseph disease:

incidence of CAG expansions among adult-onset ataxia patients from 311 families with dominant, recessive, or sporadic ataxia. *Am. J. Hum. Genet.,* **57**, 603–608.

[45] O. Riess, U. Rüb, A. Pastore, Bauer and L. Schöls (2008) SCA3: neurological features, pathogenesis and animal models. *Cerebellum,* **7**, 125–137.

[46] M. Arrasate, S. Mitra, E. Schweitzer, M. Segal and S. Finkbeiner (2004) Inclusion body formation reduces levels of mutant huntingtin and the risk of neuronal death. *Nature,* **431**, 805–810.

[47] C. Ross and M. Poirier (2005) Opinion: What is the role of protein aggregation in neurodegeneration? *Nat. Rev. Mol. Cell Biol. ,* **6**, 891-898.

[48] E. Slow, R. Graham, A. Osmand, R. Devon, G. Lu, Y. Deng, J. Pearson, K. Vaid, N. Bissada, R. Wetzel, B. Leavitt and M. Hayden (2005) Absence of behavioral abnormalities and neurodegeneration in vivo despite widespread neuronal huntingtin inclusions. *Proc. Natl. Acad. Sci. U.S.A.,* **102**, 11402–11407.

[49] L. Li, Z. Yu, X. Teng and N. Bonini (2008) RNA toxicity is a component of ataxin-3 degeneration in Drosophila. *Nature,* **453**, 1107–1111.

[50] P. Coutinho and C. Andrade (1978) Autosomal dominant system degeneration in Portuguese families of the Azores Islands. A new genetic disorder involving cerebellar, pyramidal, extrapyramidal and spinal cord motor functions. *Neurology,* **28**, 703-709.

[51] R. Rosenberg (1992) Machado–Joseph disease: an autosomal dominant motor system degeneration. *Mov. Disord.,* **7**, 193–203.

[52] L. Sudarsky and P. Coutinho (1995) Machado–Joseph disease. *Clin. Neurosci.,* **3**, 17–22.

[53] L. Schols, P. Bauer, T. Schmidt, T. Schulte and O. Riess (2004) Autosomal dominant cerebellar ataxias: clinical features, genetics, and pathogenesis. *Lancet Neurol.,* **3**, 291–304.

[54] Y. Kawaguchi, T. Okamoto, M. Taniwaki, M. Aizawa, M. Inoue, S. Katayama, H. Kawakami, S. Nakamura, M. Nishimura, I. Akiguchi et al. (1994) CAG expansions in a novel gene for Machado–Joseph disease at chromosome 14q32.1. *Nat. Genet.,* **8**, 221–228.

[55] Y. Takiyama, M. Nishizawa, H. Tanaka, S. Kawashima, H. Sakamoto, Y. Karube, H. Shimazaki, M. Soutome, K. Endo, S. Ohta and et al. (1993) The gene for Machado–Joseph disease maps to human chromosome 14q. *Nat. Genet.,* **4**, 300–304.

[56] C. Cummings and H. Zoghbi (2000) Fourteen and counting: unraveling trinucleotide repeat diseases. *Hum. Mol. Genet.,* **9**, 909–916.

[57] P. Maciel, M. Costa, A. Ferro, M. Rousseau, C. Santos, C. Gaspar, J. Barros, G. Rouleau, P. Coutinho and J. Sequeiros (2001) Improvement in the molecular diagnosis of Machado–Joseph disease. *Arch. Neurol.,* **58**, 1821–1827.

[58] S. Alves, E. Regulier, I. Nascimento-Ferreira, R. Hassig, N. Dufour, A. Koeppen, A. Carvalho, S. Simoes, M. de Lima, E. Brouillet, V. Gould, N. Deglon and L. de Almeida(2008) Striatal and nigral pathology in a lentiviral rat model of Machado–Joseph disease. *Hum. Mol. Genet.,* **17**, 2071–2083.

[59] T. Kanda, E. Isozaki, S. Kato, H. Tanabe and M. Oda (1989) Type III Machado–Joseph disease in a Japanese family: a clinicopathological study with special reference to the peripheral nervous system. *Clin. Neuropathol.,* **8**, 134–141.

[60] U. Rub, E. Brunt and T. Deller (2008) New insights into the pathoanatomy of spinocerebellar ataxia type 3 (Machado–Joseph disease). *Curr. Opin. Neurol.,* **21**, 111–116.

[61] H. Shimizu, M. Yamada, Y. Toyoshima, T. Ikeuchi, O. Onodera and H. Takahashi (2010) Involvement of Onuf's nucleus in Machado–Joseph disease: a morphometric and immunohistochemical study. *Acta Neuropathol.,* **120**, 439–448.

[62] B. Soong, C. Cheng, R. Liu and D. Shan (1997) Machado–Joseph disease: clinical, molecular, and metabolic characterization in Chinese kindreds. *Ann. Neurol.,* **41**, 446–452.

[63] U. Wullner, M. Reimold, M. Abele, K. Burk, M. Minnerop, B. Dohmen, H. Machulla, R. Bares and T. Klockgether (2005) Dopamine transporter positron emission tomography in spinocerebellar ataxias type 1, 2, 3, and 6. *Arch. Neurol.,* **62**, 1280–1285.

[64] T. Yen, C. Lu, K. Tzen, S. Wey, Y. Chou, Y. Weng, P. Kao and G. Ting (2000) Decreased dopamine transporter binding in Machado–Joseph disease. *J. Nucl. Med. ,* **41**, 994–998.

[65] J. Sequeiros and P. Coutinho (1993) Epidemiology and clinical aspects of Machado-Joseph disease. *Adv. Neurol.,* **61**, 139-153.

[66] C. Kieling, P. Prestes, M. Saraiva-Pereira and L. Jardim (2007) Survival estimates for patients with Machado-Joseph disease (SCA3). *Clin. Genet.,* **72**, 543-545.

[67] M. Costa, J. Gomes-da-Silva, C. Miranda, J. Sequeiros, M. Santos and P. Maciel (2004) Genomic structure, promoter activity, and developmental expression of the mouse homologue of the Machado–Joseph disease (MJD) gene. *Genomics,* **84**, 361-373.

[68] Y. Ichikawa, J. Goto, M. Hattori, A. Toyoda, K. Ishii, S. Jeong, H. Hashida, N. Masuda, K. Ogata, F. Kasai, M. Hirai, P. Maciel, G. Rouleau, Y. Sakaki and I. Kanazawa (2001) The genomic structure and expression of MJD, the Machado-Joseph disease gene. *J.Hum.Genet.,* **46**, 413-422.

[69] H. Paulson, S. Das, P. Crino, M. Perez, S. Patel, D. Gotsdiner, K. Fischbeck and R. Pittman (1997) Machado–Joseph disease gene product is a cytoplasmic protein widely expressed in brain. *Ann. Neurol.,* **41**, 453-462.

[70] T. Schmidt, G. Landwehrmeyer, I. Schmitt, Y. Trottier, G. Auburger, F. Laccone, T. Klockgether, M. Volpel, J. Epplen, L. Schols and O. Riess (1998) An isoform of ataxin-3 accumulates in the nucleus of neuronal cells in affected brain regions of SCA3 patients. *Brain Pathol.,* **8**, 669-679.

[71] Y. Trottier, G. Cancel, I. An-Gourfinkel, Y. Lutz, C. Weber, A. Brice, E. Hirsch and J. Mandel (1998) Heterogeneous intracellular localization and expression of ataxin-3. *Neurobiol. Dis.,* **5**, 335-347.

[72] L. Masino, V. Musi, R. Menon, P. Fusi, G. Kelly, T. Frenkiel, Y. Trottier and A. Pastore (2003) Domain architecture of the polyglutamine protein ataxin-3: a globular domain followed by a flexible tail. *FEBS Lett.,* **549**, 21-25.

[73] M. Albrecht, M. Golatta, U. Wullner and T. Lengauer (2004) Structural and functional analysis of ataxin-2 and ataxin-3. *Eur. J. Biochem.,* **271**, 3155-3170.

[74] B. Burnett, F. Li and R. Pittman (2003) The polyglutamine neurodegenerative protein ataxin-3 binds polyubiquitylated proteins and has ubiquitin protease activity. *Hum. Mol. Genet.,* **12**, 3195–3205.

[75] G. Nicastro, R. Menon, L. Masino, P. Knowles, N. McDonald and A. Pastore (2005) The solution structure of the Josephin domain of ataxin-3: structural determinants for molecular recognition. *Proc. Natl. Acad. Sci. U.S.A.,* **102**, 10493–10498.

[76] M. Albrecht, D. Hoffmann, B.O. Evert, I. Schmitt, U. Wullner and T. Lengauer (2003) Structural modeling of ataxin-3 reveals distant homology to adaptins. *Proteins: Struct. Funct. Genet.,* **50**, 355–370,.

[77] H. Scheel, S. Tomiuk and K. Hofmann (2003) Elucidation of ataxin-3 and ataxin-7 function by integrative bioinformatics. *Hum. Mol. Genet.,* **12**, 2845-2852.

[78] Y. Mao, F. Senic-Matuglia, P. Di Fiore, S. Polo, M. Hodsdon and P. De Camilli (2005) Deubiquitinating function of ataxin-3: insights from the solution structure of the Josephin domain. *Proc. Natl. Acad. Sci. U.S.A.,* **102**, 12700–12705.

[79] G. Nicastro, L. Masino, V. Esposito, R. Menon, A. De Simone, F. Fraternali and A. Pastore (2009) Josephin domain of ataxin-3 contains two distinct ubiquitin binding sites. *Biopolymers,* **91**, 1203–1214.

[80] M. Chow, J. Mackay, J. Whisstock, M. Scanlon and S. Bottomley (2004) Structural and functional analysis of the Josephin domain of the polyglutamine protein ataxin-3. *Biochem. Biophys. Res. Commun.,* **322**, 387-394.

[81] N. Tzvetkov and P. Breuer (2007) Josephin domain-containing proteins from a variety of species are active de-ubiquitination enzymes. *Biol. Chem.,* **388**, 973–978.

[82] A. Song, C. Zhou, Y. Peng, X. Gao, Z. Zhou, Q. Fu, J. Hong, D. Lin and H. Hu (2010) Structural transformation of the tandem ubiquitin-interacting motifs in ataxin-3 and their cooperative interactions with ubiquitin chains. *PLoS One,* **5**, e13202.

[83] J. Goto, M. Watanabe, Y. Ichikawa, S. Yee, N. Ihara, K. Endo, S. Igarashi, Y. Takiyama, C. Gaspar, P. Maciel, S. Tsuji, G. Rouleau and I. Kanazawa (1997) Machado–Joseph disease gene products carrying different carboxyl termini. *Neurosci. Res.,* **28**, 373–377.

[84] G. Harris, K.G.L. Dodelzon, Gonzalez-Alegre and H. Paulson (2010) Splice isoforms of the polyglutamine disease protein ataxin-3 exhibit similar enzymatic yet different aggregation properties. *PLoS One ,* **5**, e13695.

[85] C. Bettencourt, C. Santos, R. Montiel, C. Costa Mdo, P. Cruz-Morales, L. Santos, N. Simoes, T.V.J. Kay and L.M. Maciel (2009) Increased transcript diversity: novel

splicing variants of Machado–Joseph disease gene (ATXN3). *Neurogenetics,* **11**, 193–202.

[86] S. Macedo-Ribeiro, L. Cortes, P. Maciel and A. Carvalho (2009) Nucleocytoplasmic shuttling activity of ataxin-3. *PLoS One,* **4**, e5834.

[87] H. Paulson, M. Perez, Y. Trottier, J. Trojanowski, S. Subramony, S. Das, Vig, J. Mandel, K. Fischbeck and R. Pittman (1997) Intranuclear inclusions of expanded polyglutamine protein in spinocerebellar ataxia type 3. *Neuron,* **19**, 333–344.

[88] C. Pozzi, M. Valtorta, G. Tedeschi, E. Galbusera, V. Pastori, A. Bigi, S. Nonnis, E. Grassi and P. Fusi (2008) Study of subcellular localization and proteolysis of ataxin-3. *Neurobiol. Dis.,* **30**, 190–200.

[89] C. Reina, X. Zhong and R. Pittman (2010) Proteotoxic stress increases nuclear localization of ataxin-3. *Hum. Mol. Genet.,* **19**, 235–249.

[90] D. Tait, M. Riccio, A. Sittler, E. Scherzinger, S. Santi, A. Ognibene, N. Maraldi, H. Lehrach and E. Wanker (1998) Ataxin-3 is transported into the nucleus and associates with the nuclear matrix. *Hum. Mol. Genet.,* **7**, 991–997.

[91] G. Wang, K. Ide, N. Nukina, J. Goto, Y. Ichikawa, K. Uchida, T. Sakamoto and I. Kanazawa (1997) Machado–Joseph disease gene product identified in lymphocytes and brain. *Biochem. Biophys. Res. Commun.,* **233**, 476–479.

[92] P. Antony, S. Mantele, P. Mollenkopf, J. Boy, R. Kehlenbach, O. Riess and T. Schmidt (2009) Identification and functional dissection of localization signals within ataxin-3. *Neurobiol. Dis.,* **36**, 280–292.

[93] Y. Chai, J. Shao, V. Miller, A. Williams and H. Paulson (2002) Live-cell imaging reveals divergent intracellular dynamics of polyglutamine disease proteins and supports a sequestration model of pathogenesis. *Proc. Natl. Acad. Sci. U.S.A.,* **99**, 9310–9315.

[94] E. Doss-Pepe, E. Stenroos, W. Johnson and K. Madura (2003) Ataxin-3 interactions with rad23 and valosin-containing protein and its associations with ubiquitin chains and the proteasome are consistent with a role in ubiquitin mediated proteolysis. *Mol. Cell. Biol.,* **23**, 6469–6483.

[95] S. Berke, Y. Chai, G. Marrs, H. Wen and H. Paulson (2005) Defining the role of ubiquitin-interacting motifs in the polyglutamine disease protein, ataxin-3. *J. Biol. Chem.,* **280**, 32026–32034.

[96] Y. Chai, S. Berke, R. Cohen and H. Paulson (2004) Poly-ubiquitin binding by the polyglutamine disease protein ataxin-3 links its normal function to protein surveillance pathways.. *J. Biol. Chem.,* **279**, 3605–3611.

[97] K. Donaldson, W. Li, K. Ching, S. Batalov, C. Tsai and C. Joazeiro (2003) Ubiquitin-mediated sequestration of normal cellular proteins into polyglutamine aggregates. *Proc. Natl. Acad. Sci. U.S.A.,* **100**, 8892–8897.

[98] B. Winborn, S. Travis, S. Todi, K. Scaglione, P. Xu, A. Williams, R. Cohen, J. Peng and H. Paulson (2008) The deubiquitinating enzyme ataxin-3, a polyglutamine disease protein, edits Lys63 linkages in mixed linkage ubiquitin chains. *J. Biol. Chem.,* **283**, 26436–26443.

[99] I. Schmitt, M. Linden, H. Khazneh, B. Evert, P. Breuer, T. Klockgether and U. Wuellner (2007) Inactivation of the mouse Atxn3 (ataxin-3) gene increases protein ubiquitination. *Biochem. Biophys. Res. Commun.,* **362**, 734–739.

[100] B. Burnett and R. Pittman (2005) The polyglutamine neurodegenerative protein ataxin 3 regulates aggresome formation. *Proc. Natl. Acad. Sci. U.S.A.,* **102**, 4330–4335.

[101] K. Kuhlbrodt, P. Janiesch, E. Kevei, A. Segref, R. Barikbin and T. Hoppe (2011) The Machado–Joseph disease deubiquitylase ATX-3 couples longevity and proteostasis. *Nat. Cell Biol.,* **13**, 273-281.

[102] G. Nicastro, S. Todi, E. Karaca, A. Bonvin, H. Paulson and A. Pastore (2010) Understanding the role of the Josephin domain in the PolyUb binding and cleavage properties of ataxin-3. *PLoS One,* **5**, e12430.

[103] F. Reyes-Turcu and K. Wilkinson (2009) Polyubiquitin binding and disassembly by deubiquitinating enzymes. *Chem. Rev.,* **109**, 1495–1508.

[104] F. Reyes-Turcu, K. Ventii and K. Wilkinson (2009) Regulation and cellular roles of ubiquitin-specific deubiquitinating enzymes. *Annu. Rev. Biochem.,* **78**, 363-397.

[105] S. Todi, M. Laco, B. Winborn, S. Travis, H. Wen and H. Paulson (2007) Cellular turnover of the polyglutamine disease protein ataxin-3 is regulated by its catalytic activity. *J. Biol. Chem.,* **282**, 29348–29358.

[106] A. Boeddrich, S. Gaumer, A. Haacke, N. Tzvetkov, M. Albrecht, B. Evert, E. Muller, R. Lurz, P. Breuer, N. Schugardt, S. Plassmann, K. Xu, J. Warrick, J. Suopanki, U. Wullner, R. Frank, U. Hartl, N. Bonini and E. Wanker (2006) An arginine/lysine-rich

motif is crucial for VCP/p97-mediated modulation of ataxin-3 fibrillogenesis. *EMBO J.,* **25**, 1547–1558.

[107] M. Hirabayashi, K. Inoue, K. Tanaka, K. Nakadate, Y. Ohsawa, Y. Kamei, A. Popiel, A. Sinohara, A. Iwamatsu, Y. Kimura, Y. Uchiyama, S. Hori and A. Kakizuka (2001) VCP/p97 in abnormal protein aggregates, cytoplasmic vacuoles, and cell death, phenotypes relevant to neurodegeneration. *Cell Death Differ.,* **8**, 977–984.

[108] M. Matsumoto, M. Yada, S. Hatakeyama, H. Ishimoto, T. Tanimura, S. Tsuji, A. Kakizuka, M. Kitagawa and K. Nakayama (2004) Molecular clearance of ataxin-3 is regulated by a mammalian E4. *EMBO J,* **23**, 659–669.

[109] X. Zhong and R. Pittman (2006) Ataxin-3 binds VCP/p97 and regulates retrotranslocation of ERAD substrates. *Hum. Mol. Genet.,* **15**, 2409–2420.

[110] G. Wang, N. Sawai, S. Kotliarova, I. Kanazawa and N. Nukina (2000) Ataxin-3, the MJD1 gene product, interacts with the two human homologs of yeast DNA repair protein RAD23, HHR23A and HHR23B. *Hum. Mol. Genet*., **9**, 1795–1803.

[111] Q. Wang, C. Song and C. Li (2004) Molecular perspectives on p97-VCP: progress in understanding its structure and diverse biological functions. *J. Struct. Biol.,* **146**, 44–57.

[112] Q. Wang, L. Li and Y. Ye (2006) Regulation of retrotranslocation by p97-associated deubiquitinating enzyme ataxin-3. *J. Cell Biol.,* **174**, 963–971.

[113] Q. Wang, L. Li and Y. Ye (2008) Inhibition of p97-dependent protein degradation by Eeyarestatin I. *J. Biol. Chem.,* **283**, 7445–7454.

[114] F. Li, T. Macfarlan, R. Pittman and D. Chakravarti (2002) Ataxin-3 is a histone binding protein with two independent transcriptional corepressor activities. *J. Biol. Chem.,* **277**, 45004–45012.

[115] B. Evert, J. Araujo, A. Vieira-Saecker, R. de Vos, S. Harendza, T. Klockgether and U. Wullner (2006) Ataxin-3 represses transcription via chromatin binding, interaction with histone deacetylase 3, and histone deacetylation. *J. Neurosci.,* **26**, 11474–11486.

[116] A. Rodrigues, G. Coppola, C. Santos, C. Costa Mdo, M. Ailion, J. Sequeiros, D. Geschwind and P. Maciel (2007) Functional genomics and biochemical characterization of the C. elegans orthologue of the Machado–Joseph disease protein ataxin-3. *FASEB J.,* **21**, 1126–1136.

[117] A. Rodrigues, M. do Carmo Costa, T. Silva, D. Ferreira, F. Bajanca, E. Logarinho and P. Maciel (2010) Absence of ataxin-3 leads to cytoskeletal disorganization and increased cell death. *Biochim. Biophys. Acta,* **1803**, 1154–1163.

[118] R. Kopito (2000) Aggresomes, inclusion bodies and protein aggregation. *Trends in Cell Biology,* **10**, 524-530.

[119] R. Garcia-Mata, Y. Gao and E. Sztul (2002) Hassles with taking out the garbage: aggravating aggresomes. *Traffic,* **3**, 388-396.

[120] K. Markossian and B. Kurganov (2004) Protein folding, misfolding, and aggregation. Formation of inclusion bodies and aggresomes. *Biochemistry (Mosc.),* **69**, 971–984.

[121] S. Mazzucchelli, A. De Palma, M. Riva, A. D'Urzo, C. Pozzi, V. Pastori, F. Comelli, P. Fusi, M. Vanoni, P. Tortora, P. Mauri and M.E. Regonesi (2009) Proteomic and biochemical analyses unveil tight interaction of ataxin-3 with tubulin. *Int. J. Biochem. Cell Biol.,* **41**, 2485–2492.

[122] H.A.Y. Ouyang, M. Ravichandran, A. Dong, W. Qiu, F. MacKenzie, S. Dhe-Paganon, C. Arrowsmith and R. Zhai (2012) Protein aggregates are recruited to aggresome by histone deacetylase 6 via unanchored ubiquitin C termini. *J. Biol. Chem.,* **287**, 2317-2327.

[123] K. Seidel, W. den Dunnen, C. Schultz, H. Paulson, S. Frank, R. de Vos, E. Brunt, T. Deller, H. Kampinga and U. Rub (2010) Axonal inclusions in spinocerebellar ataxia type 3. *Acta Neuropathol.,* **120**, 449–460.

[124] A. Bevivino and P. Loll (2001) An expanded glutamine repeat destabilizes native ataxin-3 structure and mediates formation of parallel beta-fibrils. *Proc. Natl. Acad. Sci. U.S.A.,* **98**, 11955–11960.

[125] M. Chow, H. Paulson and S. Bottomley (2004) Destabilization of a non-pathological variant of ataxin-3 results in fibrillogenesis via a partially folded intermediate: a model for misfolding in polyglutamine disease. *J. Mol. Biol.,* **335**, 333–341.

[126] N. Jana and N. Nukina (2004) Misfolding promotes the ubiquitination of polyglutamine- expanded ataxin-3, the defective gene product in SCA3/MJD. *Neurotox. Res.*, **6**, 523–533.

[127] P. Muchowski and J. Wacker (2005) Modulation of neurodegeneration by molecular chaperones. *Nat. Rev. Neurosci.,* **6**, 11–22.

[128] Y. Nagai, T. Inui, H. Popiel, N. Fujikake, K. Hasegawa, Y. Urade, Y. Goto, H. Naiki and T. Toda (2007) A toxic monomeric conformer of the polyglutamine protein. *Nat. Struct. Mol. Biol.,* **14**, 332–340.

[129] M. Tanaka, I. Morishima, T. Akagi, T. Hashikawa and N. Nukina (2011) Intra- and intermolecular beta-pleated sheet formation in glutamine-repeat inserted myoglobin as a model for polyglutamine diseases. *J. Biol. Chem.,* **276**, 45470–45475.

[130] A. Williams and H. Paulson (2008) Polyglutamine neurodegeneration: protein misfolding revisited. *Trends Neurosci.,* **31**, 521–528.

[131] V. Uversky (2010) Mysterious oligomerization of the amyloidogenic proteins. *FEBS J.,* **277**, 2940–2953.

[132] L. Gales, L. Cortes, C. Almeida, C. Melo, M. Costa, P. Maciel, D. Clarke, A. Damas and S. Macedo-Ribeiro (2005) Towards a structural understanding of the fibrillization pathway in Machado–Joseph's disease: trapping early oligomers of non-expanded ataxin-3. *J. Mol. Biol.,* **353**, 642–654.

[133] A. Ellisdon, M. Pearce and S. Bottomley (2007) Mechanisms of ataxin-3 misfolding and fibril formation: kinetic analysis of a disease-associated polyglutamine protein. *J. Mol. Biol.,* **368**, 595–605.

[134] A. Ellisdon, B. Thomas and S. Bottomley (2006) The two-stage pathway of ataxin-3 fibrillogenesis involves a polyglutamine-independent step. *J. Biol. Chem.,* **281**, 16888–16896.

[135] A. Natalello, A. M. Frana, A. Relini, A. Apicella, G. Invernizzi, C. Casari, A. Gliozzi, S.M. Doglia, P. Tortora and M.E. Regonesi (2011) A major role for side-chain polyglutamine hydrogen bonding in irreversible ataxin-3 aggregation. *PLoS One,* **6**, e18789.

[136] L. Masino, G. Nicastro, R. Menon, F. Dal Piaz, L. Calder and A. Pastore (2004) Characterization of the structure and the amyloidogenic properties of the Josephin domain of the polyglutamine-containing protein ataxin-3. *J. Mol. Biol.,* **344**, 1021–1035.

[137] H. Saunders and S. Bottomley (2009) Multi-domain misfolding: understanding the aggregation pathway of polyglutamine proteins. *Protein Eng. Des. Sel.,* **22**, 447–451.

[138] L. Masino, G. Nicastro, L. Calder, M. Vendruscolo and A. Pastore (2011) Functional interactions as a survival strategy against abnormal aggregation. *FASEB J.,* **25**, 45–54.

[139] M. Smith and M. Snyder (2006) Yeast as a model for human disease. *Curr. Protoc. Hum. Genet.,* **Ch. 15**, Unit 15.6.

[140] D. Botstein, S. A. Chervitz and J. M. Cherry (1997) Yeast as a model organism. *Science,* **277**, 1259–1260.

[141] D. Botstein and G. Fink (1988) Yeast: an experimental organism for modern biology. *Science,* **240**, 1439–1443.

[142] F. Sherman (2002) Getting started with yeast. *Methods Enzymol.,* **350**, 3–41.

[143] V. Khurana and S. Lindquist (2010) Modelling neurodegeneration in Saccharomyces cerevisiae: why cook with baker's yeast? *Nature Reviews,* **11**, 436-449.

[144] S. Lindquist, S. Krobitsch, L. Li and N. Sondheimer (2001) Investigating protein conformation-based inheritance and disease in yeast. *Phil. Trans. R. Soc. Lond. B,* **356**, 169–176.

[145] P. Tessier and S. Lindquist (2009) Unraveling infectious structures, strain variants and species barriers for the yeast prion [PSI+]. *Nature Struct. Mol. Biol.,* **16**, 598–605.

[146] A.B. Knott, G. Perkins, R. Schwarzenbacher and E. Bossy-Wetzel (2008) Mitochondrial fragmentation in neurodegeneration. *Nature Rev. Neurosci.,* **9**, 505–518.

[147] J.T. Littleton and H.J. Bellen (1995) Synaptotagmin controls and modulates synaptic-vesicle fusion in a Ca^{2+}-dependent manner. *Trends Neurosci.,* **18**, 177–183.

[148] W. Lin and B. Popko (2009) Endoplasmic reticulum stress in disorders of myelinating cells. *Nature Neurosci.,* **12**, 379–385.

[149] W. Scheper and J. Hoozemans (2009) Endoplasmic reticulum protein quality control in neurodegenerative disease: the good, the bad and the therapy. *Curr. Med. Chem.,* **16**, 615–626.

[150] K. Herrup and Y. Yang (2007) Cell cycle regulation in the postmitotic neuron: oxymoron or new biology? *Nature Rev. Neurosci.,* **8**, 368–378.

[151] C. Jin and J. Reed (2002) Yeast and apoptosis. *Nature Rev. Mol. Cell Biol.,* **3**, 453–459.

[152] W. Cheng, K. Leach and J. Hardwick (2008) Mitochondrial death pathways in yeast and mammalian cells. *Biochim. Biophys. Acta,* **1783**, 1272–1279.

[153] H. Nakatogawa, K. Suzuki, Y. Kamada and Y. Ohsumi (2009) Dynamics and diversity in autophagy mechanisms: lessons from yeast. *Nature Rev. Mol. Cell Biol.,* **10**, 458–467.

[154] E. van Anken and I. Braakman (2005) Endoplasmic reticulum stress and the making of a professional secretory cell. *Crit. Rev. Biochem. Mol. Biol.,* **40**, 269–283.

[155] M. Pandolfo and A. Pastore (2009) The pathogenesis of Friedreich ataxia and the structure and function of frataxin. *Journal of Neurology,* **256**, 9–17.

[156] R. Wilson and D. Roof (1997) Respiratory deficiency due to loss of mitochondrial DNA in yeast lacking the frataxin homologue. *Nature Genetics,* **16**, 352–357.

[157] D. Pearce and F. Sherman (1998) A yeast model for the study of Batten disease. *Proc. Natl. Acad. Sci. U.S.A.,* **95**, 6915–6918.

[158] A. Berger, P. Hanson, J. Nichols and A. Corbett (2005) A yeast model system for functional analysis of the Niemann-Pick type C protein 1 homolog, Ncr1. *Traffic,* **6**, 907–917.

[159] Y. Sanchez, B. Desany, W. Jones, Q. Liu, B. Wang and S. Elledge (1996) Regulation of RAD53 by the ATM-like kinases MEC1 and TEL1 in yeast cell cycle checkpoint pathways. *Science,* **271**, 357–360.

[160] M. Nolden, S. Ehses, M. Koppen, A. Bernacchia, E.I. Rugarli, T. Langer. (2005) The m-AAA protease defective in hereditary spastic paraplegia controls ribosome assembly in mitochondria. *Cell,* **123**, 277–289.

[161] R. Wickner (1994) [URE3] as an altered URE2 protein: evidence for a prion analog in Saccharomyces cerevisiae. *Science,* **264**, 566–569.

[162] B. Johnson, J. McCaffery, S. Lindquist and A. Gitler (2008) A yeast TDP-43 proteinopathy model: exploring the molecular determinants of TDP-43 aggregation and cellular toxicity. *Proc. Natl. Acad. Sci. U.S.A.,* **105**, 6439–6444.

[163] K. Fushimi, C. Long, N. Jayaram, X. Chen, L. Li and J. Wu (2011) Expression of human FUS/TLS in yeast leads to protein aggregation and cytotoxicity, recapitulating key features of FUS proteinopathy. *Protein and Cell,* **2**, 141– 149.

[164] F. Giorgini, Guidetti, Q. Nguyen, S. C. Bennett and J. Muchowski (2005) A genomic screen in yeast implicates kynurenine 3-monooxygenase as a therapeutic target for Huntington disease. *Nature Genet.,* **37**, 526–531.

[165] S. Sokolov, A. Pozniakovsky, N. Bocharova, D. Knorre and F. Severin (2006) Expression of an expanded polyglutamine domain in yeast causes death with apoptotic markers. *Biochim. Biophys. Acta ,* **1757**, 660–666.

[166] M.L. Duennwald and S. Lindquist (2008) Impaired ERAD and ER stress are early and specific events in polyglutamine toxicity. *Genes Dev.,* **22**, 3308–3319.

[167] Q. Chen, J. Thorpe and J. N. Keller (2005) α-Synuclein alters proteasome function, protein synthesis, and stationary phase viability. *J. Biol. Chem.,* **280**, 30009–30017.

[168] C. Dixon, N. Mathias, R. Zweig, D. Davis and D. Gross (2005) α-Synuclein targets the plasma membrane via the secretory pathway and induces toxicity in yeast. *Genetics,* **170**, 47–59.

[169] C. Pereira, C. Bessa, J. Soares, M. Leao and L. Saraiva (2012) Contribution of yeast models to neurodegeneration research. *J. Biomed. Biotechnol,* **2012**, Article ID 941232.

[170] S. Krobitsch and S. Lindquist (2000) Aggregation of huntingtin in yeast varies with the length of the polyglutamine expansion and the expression of chaperone proteins. *Proc. Natl. Acad. Sci. U.S.A.,* **97**, 1589–1594.

[171] P. Muchowski, G. Schaffar, A. Sittler, E. Wanker, M. Hayer-Hartl and F. Hartl (2000) Hsp70 and Hsp40 chaperones can inhibit self-assembly of polyglutamine proteins into amyloid-like fibrils. *Proc. Natl. Acad. Sci. U.S.A.,* **97**, 7841–7846.

[172] B. Apostol, A. Kazantsev, S. Raffioni, K. Illes, J. Pallos, L. Bodai, N. Slepko, J. Bear, F. Gertler, S. Hersch, D. Housman, J. Marsh and L. Thompson (2003) A cell-based assay for aggregation inhibitors as therapeutics of polyglutamine-repeat disease and validation in Drosophila. *Proc. Natl. Acad. Sci. U.S.A. ,* **100**, 5950-5955.

[173] B. Apostol, K. Illes, J. Pallos, L. Bodai, J. Wu, A. Strand, E. Schweitzer, J. Olson, A. Kazantsev, J. Marsh and L. Thompson (2006) Mutant huntingtin alters MAPK signaling pathways in PC12 and striatal cells: ERK1/2 protects against mutant huntingtin-associated toxicity. *Hum. Mol. Genet.,* **15**, 273-285.

[174] B. Woodman, R. Butler, C. Landles, M. Lupton, J. Tse, E. Hockly, H. Moffitt, K. Sathasivam and G. Bates (2007) The Hdh (Q150/Q150) knock-in mouse model of

HD and the R6/2 exon 1 model develop comparable and widespread molecular phenotypes. *Brain Res. Bull.,* **72**, 83–97.

[175] A. Meriin, X. Zhang, X. He, G. Newnam, Y. Chernoff and M. Sherman (2002) Huntington toxicity in yeast model depends on polyglutamine aggregation mediated by a prion-like protein Rnq1. *J. Cell Biol. ,* **157**, 997–1004.

[176] M. Duennwald, S. Jagadish, F. Giorgini, P. Muchowski and S. Lindquist (2006) A network of protein interactions determines polyglutamine toxicity. *Proc. Natl. Acad. Sci. U.S.A.,* **103**, 11051–11056.

[177] M. Duennwald, S. Jagadish, J. Muchowski and S. Lindquist (2006) Flanking sequences profoundly alter polyglutamine toxicity in yeast. *Proc. Natl. Acad. Sci. U.S.A. ,* **103**, 11045–11050.

[178] H. Gong, N. Romanova, K. Allen, P. Chandramowlishwaran, K. Gokhale, G. Newnam, P. Mieczkowski, M. Sherman and Y. Chernoff (2012) Polyglutamine toxicity is controlled by prion composition and gene dosage in yeast. *PLoS Genet.,* **8**, e1002634.

[179] A. Meriin, X. Zhang, N. Miliaras, A. Kazantsev, Y. Chernoff, J. McCaffery, B. Wendland and M. Sherman (2003) Aggregation of expanded polyglutamine domain in yeast leads to defects in endocytosis. *Mol. Cell. Biol.,* **23**, 7554–7565.

[180] A. Meriin, X. Zhang, I. Alexandrov, A. Salnikova, M. Ter-Avanesian, Y. Chernoff and M. Sherman (2007) Endocytosis machinery is involved in aggregation of proteins with expanded polyglutamine domains. *FASEB J.,* **21**, 1915–1925.

[181] R. Hughes, R. Lo, C. Davis, A. Strand, C. Neal, J. Olson and S. Fields (2001) Altered transcription in yeast expressing expanded polyglutamine. *Proc. Natl .Acad. Sci. U.S.A.,* **98**, 13201–13206.

[182] A. Solans, A. Zambrano, M. Rodriguez and A. Barrientos (2006) Cytotoxicity of a mutant huntingtin fragment in yeast involves early alterations in mitochondrial OXPHOS complexes II and III. *Hum. Mol. Genet.,* **15**, 3063–3081.

[183] A. Ocampo, A. Zambrano and A. Barrientos (2010) Suppression of polyglutamine-induced cytotoxicity in Saccharomyces cerevisiae by enhancement of mitochondrial biogenesis. *FASEB J.,* **24**, 1431–1441.

[184] P. Joyner, R. Matheke, L. Smith and R. Cichewicz (2010) Probing the metabolic aberrations underlying mutant huntingtin toxicity in yeast and assessing their degree of preservation in humans and mice. *J. Proteome Res.,* **9**, 404–412.

[185] R. Braun, S. Büttner, J. Ring, G. Kroemer and F. Madeo (2010) Nervous yeast: modeling neurotoxiv cell death. *Trends Biochem. Sci.,* **35**, 135-144.

[186] M. Thevandavakkam, R. Schwarcz, P. Muchowski and F. Giorgini (2010) Targeting kynurenine 3-monooxygenase (KMO): implications for therapy in Huntington's disease. *CNS Neurol. Disord. Drug Targets,* **9**, 791–800.

[187] X. Zhang, D. Smith, A. Meriin, S. Engemann, D. Russel, M. Roark, S. Washington, M. Maxwell, J. Marsh, L. Thompson, E. Wanker, A. Young, D. Housman, G. Bates, M. Sherman and A. Kazantsev (2005) A potent small molecule inhibits polyglutamine aggregation in Huntington's disease neurons and suppresses neurodegeneration *in vivo*. *Proc. Natl Acad. Sci. U.S.A.,* **102**, 892-897.

[188] R. Bodner, T. Outeiro, S. Altmann, M. Maxwell, S. Cho, B. Hyman, P. McLean, A. Young, D. Housman and A. Kazantsev (2006) Pharmacological promotion of inclusion formation: a therapeutic approach for Huntington's and Parkinson's diseases. *Proc .Natl Acad. Sci. U.S.A.,* **103**, 4246-4251.

[189] D. Ehrnhoefer, M. Duennwald, Markovic, J. Wacker, S. Engemann, M. Roark, J. Legleiter, J. Marsh, L. Thompson, S. Lindquist, P. Muchowski and E. Wanker (2006) Green tea (-)-epigallocatechin-gallate modulates early events in huntingtin misfolding and reduces toxicity in Huntington's disease models. *Hum. Mol. Genet.,* **15**, 2743-2751.

[190] S. Sarkar, E. Perlstein, S. Imarisio, S. Pineau, A. Cordenier, R. Maglathlin, J. Webster, T. Lewis, C. O'Kane, S. Schreiber and D. Rubinsztein (2007) Small molecules enhance autophagy and reduce toxicity in Huntington's disease models. *Nat. Chem. Biol.,* **3**, 331-338.

[191] M. Verma, A. Sharma, S. Naidu, A. Bhadra, R. Kukreti and V. Taneja (2012) Curcumin prevents formation of polyglutamine aggregates by inhibiting Vps36, a component of the ESCRT-II complex. *PLoS ONE,* **7**, e42923.

[192] A. Aguzzi and T. O'Connor (2010) Protein aggregation diseases: pathogenicity and therapeutic perspectives. *Nat. Rev. Drug Discovery,* **9**, 237–248.

[193] G. Merlini, E. Ascari, N. Amboldi, V. Bellotti, E. Arbustini, V. Perfetti, M. Ferrari, I. Zorzoli, M. Marinone and P. Garini (1995) Interaction of the anthracycline 4'-iodo-4'-deoxydoxorubicin with amyloid fibrils: inhibition of amyloidogenesis. *Proc. Natl Acad. Sci. U.S.A.,* **92**, 295929-63.

[194] V. Heiser, E. Scherzinger, A. Boeddrich, E. Nordhoff, R. Lurz, N. Schugardt, H. Lehrach and E. Wanker (2000) Inhibition of huntingtin fibrillogenesis by specific antibodies and small molecules: implications for Huntington's disease therapy. *Proc. Natl Acad. Sci. U.S.A.,* **97**, 6739-6744.

[195] G. Forloni, L. Colombo, L. Girola, F. Tagliavini and M. Salmona (2001) Anti-amyloidogenic activity of tetracyclines: studies in vitro. *FEBS Lett.,* **487**, 404-407.

[196] D. Howlett, A. George, D. Owen, R. Ward and R. Markwell (1999) Common structural features determine the effectiveness of carvedilol, daunomycin and rolitetracycline as inhibitors of Alzheimer β-amyloid fibril formation. *Biochem. J.,* **343**, 419–423.

[197] M. Findeis (2000) Approaches to discovery and characterization of inhibitors of amyloid beta-peptide polymerization.. *Biochim. Biophys. Acta,* **1502**, 76-84.

[198] N. Cashman and B. Caughey (2004) Prion diseases -- close to effective therapy?. *Nat. Rev. Drug Discov.,* **3**, 874-884.

[199] P. Bauer and N. Nukina (2009) The pathogenic mechanisms of polyglutamine diseases and current therapeutic strategies. *J. Neurochem*., **110**, 1737–1765.

[200] H. Paulson, N. Bonini and K. Roth (2000) Polyglutamine disease and neuronal cell death. *Proc. Natl. Acad. Sci. U.S.A.,* **97**, 12957–12958.

[201] H. Graham (1992) Green tea composition, consumption, and polyphenol chemistry. *Prev. Med.,* **21**, 334–350.

[202] S. Sang, J. Lambert, C. Ho and C. Yang (2011) The chemistry and biotransformation of tea constituents. *Pharmacol. Res.,* **64**, 87–99.

[203] D. Balentine, S. Wiseman and L. Bouwens (1997) The chemistry of tea flavonoids. *Crit. Rev. Food Sci. Nutr.,* **37**, 693–704.

[204] S. Mandel and M. Youdim (2012) In the rush for green gold: can green tea delay age-progressive brain neurodegeneration? *Recent Pat. CNS Drug Discov.,* **7**, 205–217.

[205] S. Mandel, T. Amit, O. Weinreb and M. Youdim (2011) Understanding the broad spectrum neuroprotective action profile of green tea polyphenols in aging and neurodegenerative diseases. *J. Alzheimers Dis.,* **25**, 187–208.

[206] M. Suganuma, S. Okabe, M. Oniyama, Y. Tada, H. Ito and H. Fujiki (1998) Wide distribution of [3H](-)-epigallocatechin gallate, a cancer preventive tea polyphenol, in mouse tissue. *Carcinogenesis,* **19**, 1771–1776.

[207] S. Henning, Y. Niu, N. Lee, G. Thames, R. Minutti, H. Wang, V. Go and D. Heber (2004) Bioavailability and antioxidant activity of tea flavanols after consumption of green tea, black tea, or a green tea extract supplement. *Am. J. Clin. Nutr.,* **80**, 1558–1564.

[208] D. Ehrnhoefer, J. Bieschke, A. Boeddrich, M. Herbst, L. Masino, R. Lurz, S. Engemann, A. Pastore and E. Wanker (2008) EGCG redirects amyloidogenic polypeptides into unstructured, off-pathway oligomers. *Nat. Struct. Mol. Biol.,* **15**, 558-566.

[209] J. Harper and P. Lansbury (1997) Models of amyloid seeding in Alzheimer's disease and scrapie: mechanistic truths and physiological consequences of the time-dependent solubility of amyloid proteins. *Annu. Rev. Biochem.,* **66**, 385–407.

[210] J. Rochet and P. Lansbury (2000) Amyloid fibrillogenesis: themes and variations. *Curr. Opin. Struct. Biol.,* **10**, 60–68.

[211] C. Bertoncini, C. Fernandez, C. Griesinger, T. Jovin and M. Zweckstetter (2005) Familial mutants of alpha-synuclein with increased neurotoxicity have a destabilized conformation. *J. Biol. Chem.,* **280**, 30649–30652.

[212] J. Bieschke, J. Russ, R. Friedrich, D. Ehrnhoefer, H. Wobst, K. Neugebauer and E. Wanker (2010) EGCG remodels mature alpha-synuclein and amyloid-beta fibrils and reduces cellular toxicity. *Proc. Natl Acad. Sci. U.S.A.,* **107**, 7710-7715.

[213] I. Chopra and M. Roberts (2001) Tetracycline antibiotics: mode of action, applications, molecular biology, and epidemiology of bacterial resistance. *Microbiol. Mol. Biol. Rev.,* **65**, 232-260.

[214] Y. Choi, H. Kim, K. Shin, E. Kim, M. Kim, H. Kim, C. Park, Y. Jeong, J. Yoo, J. Lee, K. Chang, S. Kim and Y. Suh (2007) Minocycline attenuates neuronal cell death and improves cognitive impairment in Alzheimer's disease models. *Neuropsychopharmacology,* **32**, 2393–2404.

[215] G. Forloni, M. Salmona, G. Marcon and F. Tagliavini (2009) Tetracyclines and prion infectivity. *Infect. Disord. Drug Targets,* **9**, 23–30.

[216] W. Noble, C. Garwood, J. Stephenson, A. Kinsey, D. Hanger and B. Anderton (2008) Minoycline reduces the deveoplment of abnormal tau species in models of Alzheimer's disease. *FASEB J.,* **23**, 1–12.

[217] M. Bendeck, M. Conte, M. Zhang, N. Nili, B. Strauss and S. Farwell (2002) Doxycycline modulates smooth muscle cell growth, migration, and matrix remodeling after arterial injury. *Am. J. Pathol.,* **160**, 1089-1095.

[218] F. Tagliavini, G. Forloni, L. Colombo, G. Rossi, L. Girola, B. Canciani, N. Angeretti, L. Giampaolo, E. Peressini, T. Awan, L. De Gioia, E. Ragg, O. Bugiani and M. Salmona (2000) Tetracycline affects abnormal properties of synthetic PrP peptides and PrP(Sc) in vitro. *J. Mol. Biol.,* **300**, 1309-1322.

[219] K. Ono and M. Yamada (2006) Antioxidant compounds have potent anti-fibrillogenic and fibril-destabilizing effects for α-synuclein fibrils in vitro. *J. Neurochem*., **97**, 105−115.

[220] M. Chen, V.O. Ona, M. Li, R.J. Ferrante, K.B. Fink, S. Zhu, J. Bian, L. Guo, L.A. Farrell, S.M. Hersch, W. Hobbs, J. Vonsattel, J.H. Cha and R.M. Friedlander (2000) Minocycline inhibits caspase-1 and caspase-3 expression and delays mortality in a transgenic mouse model of Huntington disease. *Nat. Med.,* **6**, 797−801.

[221] D.L. Smith, B. Woodman, A. Mahal, K. Sathasivam, S. Ghazi-Noori, A. Lowden, G. Bates and E. Hockly (2003) Minocycline and doxycycline are not beneficial in a model of Huntington's disease. *Ann.Neurol.,* **54**, 186−196.

[222] T. Stoilova, L. Colombo, G. Tagliavini, F. Forloni and M. Salmona (2013) A new face for old antibiotics: tetracyclines in treatment of amyloidoses. *J. Med. Chem.,* **56**, 5987−6006.

[223] R. Garcia-Mata, Z. Bebok, E. Sorscher and E. Sztul (1999) Characterization and dynamics of aggresome formation by a cytosolic GFP-chimera. *J. Cell Biol*., **146**, 1239–1254.

[224] Y. Kawaguchi, J. Kovacs, A. McLaurin, J. Vance, A. Ito and T. Yao (2003) The deacetylase HDAC6 regulates aggresome formation and cell viability in response to misfolded protein stress. *Cell*, **115**, 727–738.

[225] H. de Forges, A. Bouissou and F. Perez (2012) Interplay between microtubule dynamics and intracellular organization. *Int. J. Biochem. Cell Biol.* , **44**, 266-274.

[226] M. Chow, A. Ellisdon, L. Cabrita and S. Bottomley (2006) Purification of polyglutamine proteins. *Methods Enzymol.,* **413**, 1–19.

[227] M. Roessle, R. Klaering, U. Ristau, B. Robrahn, D. Jahn, T. Gehrmann, P. Konarev, A. Round, S. Fiedler and C. Hermes (2007) Upgrade of the small-angle X-ray scattering beamline X33 at the European Molecular Biology Laboratory, Hamburg. *J. Appl. Crystallogr.,* **40**, 190-194.

[228] P. Konarev, V. Volkov, A. Sokolova, M. Koch and D. Svergun (2003) PRIMUS: A Windows-PC based system for small-angle scattering data analysis. *J. Appl. Crystallogr.*, **36**, 1277–1282.

[229] A. Guinier (1939) La diffraction des rayous X aux tres petits angles: application a l'etude de phenomenes ultramicroscopiques. *Ann. Phys.*, 12, 161–237.

[230] D. Svergun (1992) Determination of the regularization parameter in indirect transform method using perceptual criteria. *J. Appl. Crystallogr*., **25**, 495–503.

[231] G. Porod (1982) General theory. In Small-angle X-ray scattering (Glatter, O., and Kratky, O., Eds.), Academic Press, London.

[232] D. Franke and D. Svergun (2009) DAMMIF, a program for rapid *ab-initio* shape determination in small-angle scattering. *J. Appl. Crystallogr.,* **42**, 342–346.

[233] D. Svergun (1999) Restoring low resolution structure of biological macromolecules from solution scattering using simulated annealing. *Biophys. J.*, **76**, 2879–2886.

[234] V.S.D. Volkov (2003) Uniqueness of *ab initio* shape determination in small angle scattering. *J. Appl. Crystallogr.*, **36**, 860-864.

[235] M. Kozin and D. Svergun (2001) Automated matching of highand low- resolution structural models. *J. Appl. Crystallogr.*, **34**, 33-41.

[236] E. Nogales, S. Wolf and K. Downing (1998) Structure of the alpha beta tubulin dimer by electron crystallography. *Nature*, **391**, 199-203.

[237] R. Ravelli, B. Gigant, P. Curmi, I. Jourdain, S. Lachkar, A. Sobel and M. Knossow (2004) Insight into tubulin regulation from a complex with colchicine and a stathmin-like domain. *Nature*, **428**, 198-202.

[238] D. Svergun, C. Barberato and M. Koch (1995) CRYSOL - a program to evaluate X-ray solution scattering of biological macromolecules from atomic coordinates. *J. Appl. Crystallogr.,* **28**, 768-773.

[239] E. Nogales, M. Whittaker, R. Milligan and K. Downing (1999) High-resolution model of the microtubule. *Cell*, **96**, 79-88.

[240] J. Johnstron, C. Ward and R. Kopito (1998) Aggresomes: a cellular response to misfolded proteins. *J. Cell Biol.*, **143**, 1883-1898.

[241] C. Olanow, D. Perl, G. DeMartino and K. McNaught (2004) Lewy-body formation is an aggresome-related process: a hypothesis. *Lancet Neurol.*, **3**, 496-503.

[242] A. Valenzuela-Fernández, J. Cabrero, J. Serrador and F. Sánchez-Madrid (2008) HDAC6: a key regulator of cytoskeleton, cell migration and cell–cell interactions. *Trends Cell Biol.*, **18**, 291-297.

[243] N. Caron, C. Desmond, J. Xia and R. Truant (2013) Polyglutamine domain flexibility mediates the proximity between flanking sequences in huntingtin. *Proc. Natl. Acad. Sci. U.S.A.*, **110**, 14610-14615.

[244] E. Sacco, M. Farina, C. Greco, S. Lamperti, S. Busti, L. Degioia, L. Alberghina, D. Liberati and M. Vanoni (2012) Regulation of hSos1 activity is a system-level property generated by its multi-domain structure. *Biotechnol. Adv.*, **30**, 154-168.

[245] M. Duennwald (2011) Polyglutamine misfolding in yeast: toxic and protective aggregation. *Prion,* **5**, 285-290.

[246] S. Campioni, B. Mannini, M. Zampagni, A. Pensalfini, C. Parrini, E. Evangelisti, A. Relini, M. Stefani, C.M. Dobson, C. Cecchi and F. Chiti (2010) A causative link between the structure of aberrant protein oligomers and their toxicity. *Nat. Chem. Biol.,* **6**, 140-147.

[247] P. Lajoie and E. Snapp (2010) Formation and toxicity of soluble polyglutamine oligomers in living cells. *PLoS ONE,* **5**, e15245.

[248] R. Kayed, E. Head, J. Thompson, T. McIntire, S. Milton, C. Cotman and C. Glabe (2003) Common structure of soluble amyloid oligomers implies common mechanism of pathogenesis. *Science,* **300**, 486–489.

[249] G. Schaffar, P. Breuer, R. Boteva, C. Behrends, N. Tzvetkov, N. Strippel, H. Sakahira, K. Siegers, M. Hayer-Hartl and F. Hartl (2004) Cellular toxicity of polyglutamine

expansion proteins: mechanism of transcription factor deactivation. *Mol. Cell,* **15**, 95–105.

[250] A. Cooper, A. Gitler, A. Cashikar, C. Haynes, K. Hill, B. Bhullar, K. Liu, K. Xu, K. Strathearn, F. Liu, S. Cao, K. Caldwell, G. Marsischly, R. Kolodner, J. Labaer, J. Rochet, N. Bonini and S. Lindquist (2006) Alpha-synuclein blocks ER-Golgi traffic and Rab1 rescues neuron loss in Parkinson's models. *Science,* **313**, 324-328.

[251] D. Gietz, A. St Jean, R. Woods and R. Schiestl (1994) Improved method for high efficiency transformation of intact yeast cells. *Nucl. Acids Res.,* **20**, 1425.

[252] S. Alberti, R. Halfmann and S. Lindquist (2010) Biochemical, Cell Biological, and Genetic Assays to Analyze Amyloid and Prion Aggregation in Yeast, *Methods Enzymol.,* **470**, 709–734.

[253] E. Shehi, P. Fusi, F. Secundo, S. Pozzuolo, A. Bairati and P. Tortora (2003) Temperature dependent, irreversible formation of amyloid fibrils by a soluble human ataxin-3 carrying a moderately expanded polyglutamine stretch (Q36). *Biochemistry,* **42**, 14626–14632.

[254] R. Teparić, I. Stuparević and V. Mrša (2004) Increased mortality of *Saccharomyces cerevisiae* cell wall protein mutants. *Microbiology,* **150**, 3145–3150.

[255] A. Boyne and G. Ellman (1972) A methodology for analysis of tissue sulfhydryl components. *Anal. Biochem.,* **46**, 639–653.

[256] N. Shangari and P. J. O'Brien (2006) Catalase Activity Assays. *Current Protocols in Toxicology,* **27**, 7.7.1–7.7.16.

[257] J. Hubener, F. Vauti, C. Funke, H. Wolburg, Y. Ye, T. Schmidt, K. Wolburg-Buchholz, I. Scmitt, A. Gardyan, S.A.H. Driessen, H. Nguyen and O. Riess (2011) N-terminal ataxin-3 causes neurological symptoms with inclusions, endoplasmic reticulum stress and ribosomal dislocation, *Brain,* **134**, 1925–1942.

[258] G. Invernizzi, F.A. Aprile, A. Natalello, A. Ghisleni, A. Penco, A. Relini, S. Doglia, P. Tortora and M.E. Regonesi (2012) The relationship between aggregation and toxicity of polyglutamine-containing ataxin-3 in the intracellular environment of *Escherichia coli. PLoS ONE,* **7**, e51890.

[259] H. Lashuel, D. Hartley, B. Petre, T. Walz and P. J. Lansbury (2002) Neurodegenerative disease: amyloid pores from pathogenic mutations, *Nature,* **418**, 291.

[260] E. De Lorenzi, S. Giorgetti, S. Grossi, G. Merlini, G. Caccialanza and V. Bellotti (2004) Pharmaceutical strategies against amyloidosis: old and new drugs in targeting a "protein misfolding disease". *Curr. Med. Chem.,*. **11**, 1065-1184.

[261] H. Susi and D. Byler (1986) Resolution-enhanced Fourier transform infrared spectroscopy of enzymes, *Methods Enzymol.,* **130**, 290-311.

[262] E. Goormaghtigh, V. Cabiaux and J. Ruysschaert (1994) Determination of soluble and membrane protein structure by Fourier transform infrared spectroscopy. III. Secondary structures. *Subcell. Biochem.,* **23**, 405–450.

[263] A. Barth (2000) The infrared absorption of amino acid side chains. *Prog. Biophys. Mol. Biol.,* **74**, 141–173.